PERFORMANCE ENHANCEMENT OF SEGMENTED INFRARED REFLECTORS VIA QUASISTATIC SHAPE CONTROL

by

GREGORY G. LOBODA
B.S., Aeronautical Engineering, Massachusetts Institute of Technology
(1992)

Submitted to the Department of
Aeronautics and Astronautics
In Partial Fulfillment of the Requirements
for the Degree of

MASTER OF SCIENCE IN AERONAUTICS AND ASTRONAUTICS
at the
MASSACHUSETTS INSTITUTE OF TECHNOLOGY
June, 1992

Signature of Author.....
Department of Aeronautics and Astronautics
May 8, 1992

Certified by.....
Prof. Edward F. Crawley
Thesis Supervisor

Certified by.....
Dr. James L. Hanson
Jet Propulsion Laboratory
Company Supervisor

Accepted by.....
Prof. Harold Y. Wachman
Chairman, Department Graduate Committee

Performance Enhancement of Segmented Infrared Reflectors via Quasistatic Shape Control

by

Gregory G. Loboda

Submitted to the Department of Aeronautics and Astronautics
on May 8, 1992 in partial fulfillment of the
requirements for the degree of
Master of Science in Aeronautics and Astronautics

ABSTRACT

A new technique to improve the performance of segmented reflectors operating in the infrared was developed through interaction of structural and optical models. A hypothetical six-panel reflector model was analyzed to determine nominal operating wavelength, temperature and integration time. A linear optical model of the reflector was generated using the Controlled Optics Modeling Package (COMP). Through this model, the effects of higher order surface deformations on Strehl ratio and wavefront error were evaluated. A high fidelity NASTRAN model of each panel was created to simulate the deformations created by both on-orbit thermal gradients as well as those by the surface mounted piezoelectric moment actuators. Both sets of deformations were fit to 36 Zernike polynomials, and two control algorithms were utilized. The first involved a simply constrained quadratic cost function weighted toward the minimization of surface error. The second altered the cost function by introducing a sensitivity matrix describing wavefront error with respect to changes in each panel degree of freedom. Both algorithms showed significant improvement in Strehl ratio and wavefront error, with no apparent advantage in either algorithm in correcting a thermally induced deformation.

Thesis Supervisor: Dr. Edward F. Crawley
Professor of Aeronautics and Astronautics

Company Supervisor: Dr. James L. Fanson
Lead Technologist
Jet Propulsion Laboratory

Acknowledgements

I would first like to express my deep appreciation for the advice and technical assistance I received from many members of the Jet Propulsion Laboratory during my stay there, in particular those members of sections 343 and 354. Several people, however, consistently aided me in my work, without whom I could not have completed my research. First, I want to thank Mark Milman and Dave Redding, perhaps the two most laid back mathematician/engineers I've ever encountered. Thanks for both your conceptual genius as well as your common sense in developing the analytic and COMP optical models used in this research, without which there would be no thesis. Second, I want to thank Robert Norton and C.P. Kuo, both of whom went to a lot of trouble to get my NASTRAN model off the ground. Third, thanks goes to Robert Laskin, who let me spend his money on my research with little complaint aside from the occasional glance over my shoulder. Lastly, I want to thank James Fanson and Donald Rapp, my principal advisors at JPL and the instigators of this thesis research. The motivation and dedication to his field that Jim showed provided me with the impetus to spend long nights laboring over my work. In additional to his wealth of technical knowledge, Don's wisdom, political insight, and old fashioned wit proved to be a great morale booster, and kept me going when the bureaucracy of the system seemed intent on halting my progress. To all of you at JPL, my sincere thanks.

Back at MIT, there are three professors who have strongly influenced the progress of my career as well as my thesis research. First, thanks goes to my thesis advisor Professor Edward Crawley, whose brilliance and personal appeal incited my interest in the field of structures and control. Second, I want to thank Professor Harold Wachman, who has been a good friend as well as an advisor during my five years at MIT. His faith in my abilities as a teacher and a person has made me a better engineer than I had ever hoped for. Last, thanks goes to Professor Joseph Shea. In one short year, he has transformed my perception of what engineering is about and the role I may play in it. His unparalleled wisdom in the field and willingness to help me begin my career has undoubtedly steered my future into a very positive direction.

Those who unquestionably deserve the most thanks are my friends and family. I want to thank the brothers of Alpha Tau Omega for four years of valuable lessons learned through friendship, respect and love, all of which will stay with me through my life. In particular, thanks goes to Neil Okamoto, whose selflessness, respect and steadfast friendship through

five years at MIT have been both a role model and great comfort to me. I have not, however, forgotten my close circle of Wellesley friends, namely Chia-Ann, Ruth and Jenny, who have provided me with a different perspective of college life as well as uncompromising love and affection. Special thanks goes to my newfound friend Masako, whose beauty, intelligence and "sense of humor" have proven to be both a challenge and a source of happiness for me in this last semester at MIT. I want to thank, above all others, my parents for their understated yet unwavering support of my efforts throughout my life. Their strength and courage in dealing with the imperfections of life have made them my greatest role models.

This research was conducted at the Jet Propulsion Laboratory, Pasadena, California, from May through December 1991, and was supported by the Control Structures Interaction program in cooperation with the MIT Engineering Internship Program.

This thesis report was prepared on a Macintosh SE/30 using Microsoft Word 4.0® as the text editor. Additional plots and figures were created using Kaleidagraph®, Microsoft Excel®, Edu-Matlab® and MacDraw II®.

Table of Contents

List of Figures

List of Tables

Chapter 1

Introduction

One of the goals of modern day astronomy is to view the night sky across the entire electromagnetic spectrum. A region of particular interest is the moderate to far infrared (IR) spectrum, with the wavelength λ ranging from 5 μm to 100 μm. This region promises a good potential for the detection of relatively cool objects ($\approx$ 3 K to 2000 K) which emit the majority of their energy in the infrared. These objects include brown dwarfs and planet-like bodies in orbit around nearby stars. Telescopes operating in the infrared have a much better chance for detection of dwarfs and planets than those operating in the visible for a given aperture diameter. As shown in Table 1-1, the minimum angular separation required between a star and its cool companion is much greater when the objects are observed in the visible, because the relatively huge energy output of a star in the visible spectrum effectively obliterates the weaker signal of its companion.

Table 1-1 Minimum Required Angular Resolution for Detection of a Cool Object around a 3600 K Star (arcseconds)

$\lambda(\mu m)$	10^3 K dwarf	640 K dwarf	450 K dwarf	300 K dwarf
0.5 (visible)	7.25	1600	8.90×10^5	3.8×10^{10}
10.0 (IR)	0.27	0.38	0.52	0.90
telescope diameter = 10 m				

Three major difficulties arise in the operation of a telescope in the infrared, however. First, to obtain sufficient resolution of two nearby objects at wavelengths of 5 μm or greater, large reflector diameters are required. Minimum useful diameters are on the scale of 4 meters to 20 meters. A continuous glass primary reflector of this size would weigh hundreds of tons, too heavy for the construction of a reasonable support structure. Second, ground based reflectors are victims to atmospheric absorption and turbulence, both of which tend to reduce the amount of IR energy reaching the Earth's surface. Third, many dim objects require long integration times which may even be too long for a single night's

observation.[1] A solution to these difficulties may lie in the design of a space based infrared reflector telescope.

1.1 Space Based Infrared Reflector Concept

A possible design for a space based IR reflector telescope involves the use of passive cooling technology and a primary mirror consisting of lightweight segmented panels. This telescope would potentially operate in a high Earth orbit unobstructed by the Earth's atmosphere or shadow and unaffected by gravity loading. The passive cooling involves the thermal protection of the telescope through multilayered insulation (MLI) and sunshades. Two conceptual designs for such a telescope are the Sub-Millimeter Imaging Line Survey (SMILS) telescope and the Large Deployable Reflector (LDR). SMILS is a 3.5 meter reflector composed of six hexagonal composite or semi-metallic panels surrounded by an inflatable sunshade (Fig. 1-1). Its nominal operating temperature and wavelengths are 100 K and 80 to 700 μm, respectively.[2]

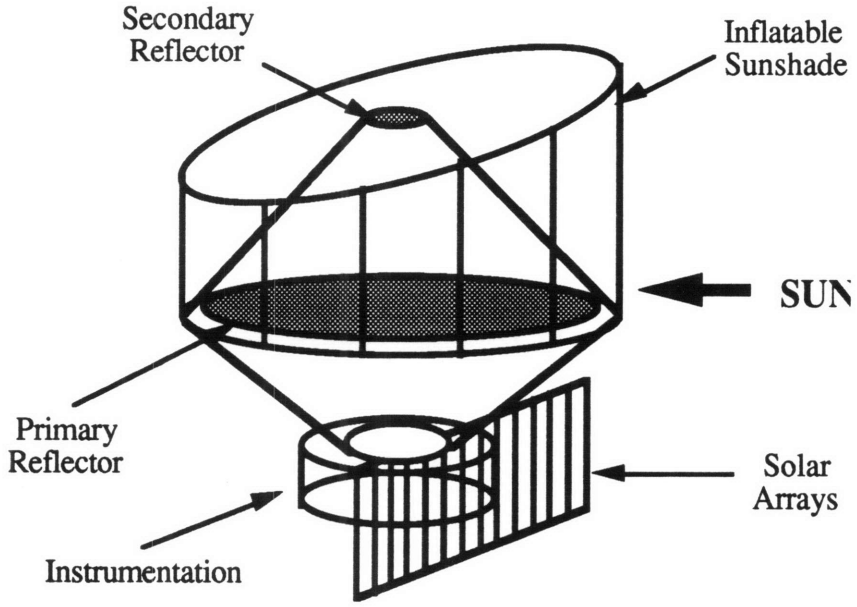

Figure 1-1
SMILS Telescope Schematic

---

[1]Rapp, Dr. Donald. "Potential for Active Structures Technology to Enable Lightweight Passively Cooled IR Telescopes", JPL Report D-9449, (1992), Appendix 1 .

[2]Rapp, et al.

LDR, a more advanced design to be assembled in space, is a 20 meter quaternary reflector composed of approximately 60 hexagonal composite panels surrounded by a rigid sunshade. Current designs specify an operating temperature of 200 K and wavelengths greater than 30 μm. Neither telescope concept currently provides the required resolution for the detection of extrasolar planets and dwarfs, although LDR would have the sufficient resolution if it were to operate at temperatures closer to 100 K.

Two problems are encountered in using lightweight composite panels in such reflector configurations. First, it is difficult to construct a rigid support structure capable of maintaining a perfect alignment of the reflector panels in orbit. Launch loads alone could misalign the panels by as much as a wavelength, causing considerable degradation of the quality of images collected through the reflector. Second, the panels themselves are constructed from low density composites which are not thermally rigid. Experiments on existing composite panels near one meter in diameter have shown that the cooling of these panels to cryogenic temperatures induces a radius of curvature (ROC) change of several microns.[3] In addition, under passive cooling, considerable thermal gradients would still exist in the reflector causing the panels to warp asymmetrically. Such conditions would produce a considerable loss in image quality and resolution, as well. A possible solution to these problems is found in the active control of optics.

1.2 Adaptive Optics

The active control of optics, or adaptive optics, involves the deliberate displacement and/or deformation of optical elements in a system to compensate for aberrations caused by misalignment or environmental conditions. The earliest serious discussion of adaptive optics for the compensation of atmospheric disturbances was by Babcock in 1953, where he proposed the use of an arbitrary deformable optical element with feedback from a wavefront sensor.[4] In 1973, Itek developed the Real Time Atmospheric Corrector (RTAC), a mirror mounted onto a monolithic piezoelectric (PZT) actuator. The PZT was imbedded with discrete electrodes, thereby allowing localized deformation of the mirror

---

[3]Hochberg, E.B. "PSR Prototype Panel Optical Figure Testing: Cryointerferometric Tests of JPL 91-03 on 5/16/91", JPL Interoffice Memorandum PSR #91-70 (1991), p. 5.

[4]Hardy, John W. "Active Optics: A New Technology for the Control of Light", Proceedings of IEEE Vol. 66, No. 6, June 1978, p. 656.

surface for real time compensation.[5] Electrostrictives (PMN) have also been implemented in adaptive optics. In 1981, researchers at the Tokyo Institute of Technology developed a thin disk mirror composed of PMN capable of refocusing a Helium-Neon laser by adjusting the radius of curvature of the mirror.[6] More recently, the 2.4 meter glass primary mirror of the Hubble Space Telescope (HST) utilizes 24 piston actuators mounted onto the rear of the mirror for fine surface correction. All of the above cases involve the shape control of reflecting surfaces. For larger segmented reflectors, other methods of control have been developed.

In 1980, the University of California at Berkeley proposed the construction of a 10 meter ground-based reflector telescope operating from 0.3 μm to 30 μm. The primary, composed of 60 1.4 meter hexagonal glass panels, was required to maintain a figure accuracy within 0.05 μm. The proposed control system involved a series of capacitive edge sensors coordinated with a three point mounting of torque driven screw rollers behind each panel. Under the assumption that the panels are completely rigid, this would allow piston-tilt control for real time compensation for wind gusts and alignment errors.[7] The W.M. Keck Telescope, nearing completion in Hawaii, is similar to the U.C. Berkeley telescope. It is a 10 meter telescope with a primary reflector composed of 36 1.8 meter glass hexagonal panels. Using a control system of edge sensors and three point piston actuators on each panel, figure accuracy will be maintained below 0.07 μm in real time.[8] In recent years, this technology has been applied to the control of lightweight composite panels. The Precision Segmented Reflector (PSR) program has analyzed the potential for the correction of composite panels which undergo deformations due to cryogenic cooling. The primary result of cooling is a significant change in ROC in the panels, effectively changing the overall reflector focal length. Correction for this type of error is to be

---

[5]Ealey, Mark. "Deformable Mirrors at Litton/Itek: A Historical Perspective", Litton/Itek Optical Systems, report #1167-04 (1990), p. 1.

[6]Uchino, K., Tsuchiya, Y., Nomura, S., Sato, T., Ishikawa, H., Ikeda, O. "Deformable Mirror Using PMN Electrostrictor", *Applied Optics*, Vol. 20 No. 17, September 1981, pp. 3077-3079.

[7]Mast, Terry S., Nelson, Jerry E. "Figure Control for a Segmented Telescope Mirror", Kitt Peak National Observatory Conference Proceedings Vol. I - *Optical and Infrared Telescopes for the 1990's*, May 1980, pp. 508-525.

[8]Aubrun, J., Lorell, K., Nast, T., Nelson, J. "Dynamic Analysis of the Actively Controlled Segmented Mirror of the W.M. Keck Ten Meter Telescope", IEEE Control Systems Proceedings Vol. VII #6 (1987), pp. 3-10.

implemented through a three point piston-tilt actuator layout similar to that in the Keck telescope. In this case, however, the control is quasistatic because the correction is performed only once or at infrequent intervals. Quasistatic control is also sufficient for space based IR telescope used for astronomical observations, which do not deal with atmospheric compensation. The above control methods do not, however, address the issue of correction for higher order deformations, or "wrinkling", in a panel's surface.

Recent efforts at the Jet Propulsion Laboratory (JPL) have been directed towards the quasistatic correction of large scale panel deformations through the implementation of surface mounted PZT actuators. These actuators, which produce an in-plane strain when energized, have been tested on PSR composite panels. Results have shown that radially symmetric configurations of these actuators are effective in correcting ROC errors.[9] Two issues still remain unaddressed, however. First, the aforementioned results did not conclusively show the ability of such actuators to correct asymmetric or higher spatial frequency deformations such as astigmatism, coma or spherical aberration, all of which are known to produce a degradation of image quality in optical systems. This leads to the second issue, that of wavefront compensation. Little work has been done in the correction of panel errors with respect to wavefront compensation. Most previous efforts have been directed towards the minimization of panel surface error. Redding has shown analytically that correction weighted towards the minimization of wavefront error provides considerably better wavefront quality than that achieved through surface error correction.[10] This analysis, however, was conducted under the constraint of three axis correction only. If such compensation methods were integrated into a control scheme capable of higher order error correction, perhaps the improvements in wavefront quality would be greater still. From these two issues, a question presents itself: can a series of surface mounted piezoelectric actuators be developed to selectively eliminate any arbitrary deformation through panel shape control, in particular those deformations which most severely degrade wavefront quality ? This question forms the basis for this present research, and is now developed into several principal objectives which may lead to a convincing answer.

---

[9]Kuo, C.P. "A Deformable Mirror Concept for Adaptive Optics in Space", Jet Propulsion Laboratory section 354 report (1991), pp. 5-10.

[10]Redding, D. "A Wavefront Compensation Approach to Segmented Mirror Figure Control", 14th Annual AAS Guidance and Control Conference, AAS 91-054 (1991), p. 1.

1.3 Objectives and Approach

The principal objectives of this research can be reduced to three statements, and are as follows:

(1) characterize the optical performance of a hypothetical reflector system as a function of the nature and magnitude of various surface aberrations

(2) quantify the level of control over surface aberrations as a function of the position and actuation strain of surface mounted PZT actuators

(3) successfully interface structural and optical models of the reflector system, and verify the effectiveness of quasistatic active correction of higher order aberrations with respect to wavefront control and image quality

The first objective involves the development of a means to represent any deformation in an optical system, and an evaluation of the optical system's sensitivity to these deformations as functions of the system's geometry and operating parameters. The second objective requires an equivalent representation of deformations in a structural model to understand how certain deformations are controllable by a specific actuator strain or combination of strains. The third objective links the previous two into a control scheme using image quality as the primary active feedback on which the piezoelectric actuators react. From this control scheme, various performance parameters are measured for comparison with nominal conditions. One of these parameters is the ability of a corrected optical system to resolve dim secondary objects around a primary star. This, along with the other performance parameters, will provide the evidence to determine whether or not quasistatic shape control is effective in reducing surface aberrations. The methodology used to evaluate the effectiveness of a scheme designed to control panel shapes for wavefront correction is based on a system's level approach. The problem is solved through the interaction of several disciplines, each contributing a part to the understanding of the problem. These disciplines include astronomy, geometric and physical optics, structures and control. The solution process involving these disciplines consists of five main steps, and is as follows:

(1) perform an analytic evaluation of the reflector's nominal performance in terms of resolution and sensitivity to background noise for the detection of cool extrasolar bodies. This determines the operating parameters such as wavelength, telescope temperature and integration time which give the best chance to detect dwarfs and planets.

(2) derive a linear analytic solution for a chosen performance metric for the prediction of optical performance assuming small perturbations in the optical system. This serves as a means of comparison against numerical results obtained for the corrected system.

(3) develop a numerical model of the optical system using current modeling software. The model represents higher order deformations as finite expansions of Zernike polynomials defined over each reflector panel. A sensitivity matrix relating changes in wavefront error to changes in panel shape is constructed, from which the deformations most detrimental to image quality are determined in terms of Zernike polynomials.

(4) construct a high fidelity structural model of a reflector panel using finite element modeling software. The PZT actuation behavior is modeled as equivalent thermal strains. Surface deformations created by a single actuator's energization are described using Zernike polynomials equivalent to those in the optical model. A control "transfer function" is developed, relating actuation strain to deformation shape.

(5) develop quadratic cost functions to optimize the actuation strain for given input aberration. One cost function optimizes to minimize surface error, the other to minimize wavefront error. The cost functions are solved for overconstrained, determinate and underconstrained control schemes. These control schemes represent different numbers and configurations of actuators on the panels. In each case, the residual error is reintroduced into the optical model, and the corrected performance is evaluated against the linear analytic solution.

The completion of these five steps is covered in five chapters. Chapter 2 deals primarily with the definition of the reflector operating parameters based on analysis for the best resolution and noise conditions available. Chapter 3 develops both the analytic and numerical optical models of the reflector used to characterize the effects of low and higher order aberrations on chosen performance metrics. Chapter 4 discusses the properties and deformation characterization of a structural model of the reflector panels onto which is mounted a series of piezoelectric actuators. Chapter 5 introduces both the test aberrations

for correction as well as the control algorithms used for the quasistatic correction. These algorithms are modified to simulate the various actuator configurations of the three control cases. Chapter 6 presents the results of the control cases, and discusses model limitations and sources of errors. Chapter 7 summarizes the findings of this report, and suggests changes and ideas for future research on this topic.

Chapter 2

Nominal Reflector Performance

The first step in developing a means to improve the image performance of an optical system for resolving binary systems is to define the system and its nominal operating parameters. Performance parameters such as operating wavelength, telescope temperature, and integration time are determined to maximize the system's ability to resolve binary objects with very different relative intensities. This then defines what is considered nominal performance for the reflector over a range of object pairs of observation.

Several steps are required in determining the nominal operating parameters. First, the optical system must be defined physically. Second, the reflector's resolving limits must be determined for various objects. Lastly, background noise must be quantified. By these means, operating parameters can be chosen to optimize the reflectors ability to resolve binary systems.

2.1 Reflector Description

The optical system consists of two major components: the primary and secondary reflectors. The primary reflector is composed of 6 independent hexagonal panels in a single ring configuration, each panel having a flat-to-flat diameter of 1.30 meters. The effective reflector diameter is 3.90 meters, with a maximum diameter of 3.972 meters (Fig. 2-1). The choice of size and configuration of the panels was based on three simple assumptions. First, the reflector needed to fit within the bay of the Space Shuttle. This constrained the maximum diameter to approximately 4 meters. Second, an additional set of rings would add 12 additional panels to the reflector, making the development of a control system for the reflector much more complex. Third, the center panel was omitted to allow space for the mounting of the secondary reflector. The missing panel does not change the effective diameter of the reflector, but reduces its collecting area.

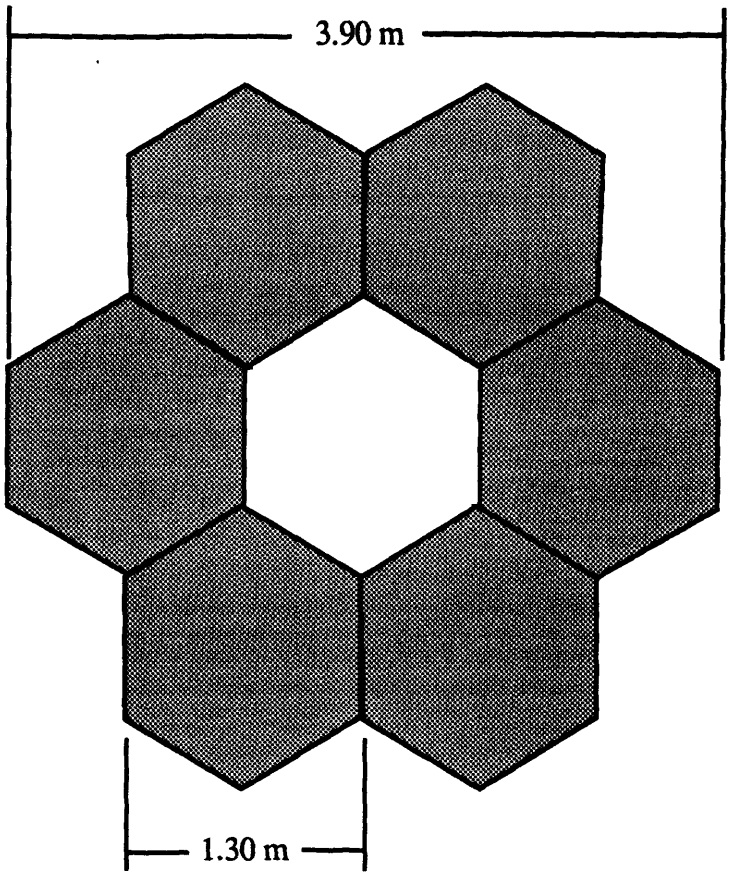

Figure 2-1
Primary Reflector Dimensions

The primary reflector is a paraboloid, with a focal length of 7.8 meters and eccentricity of 1.0. The focal number, the ratio between focal length and diameter, is therefore 2.0. The collecting area of each panel is determined by:

$$A_R = \frac{3}{2}\sqrt{3}x^2 \qquad (2.1)$$

where x is the length of one side (1.464 sq. meters). The total collection area of the six panels is 8.783 sq. meters.

The secondary mirror is a 0.78 meter single element hyperboloid mounted in a Cassegrain configuration 6.24 meters above the vertex of the primary (Fig. 2-2). The secondary has a rear focal length of 7.02 meters, focusing the image 0.78 meters beyond the vertex of the primary reflector, and an eccentricity of 1.571. The total focal number of the system is 3.80.

The optical system is assumed to be passively cooled by multilayered insulation or sunshades surrounding the primary reflector. This would potentially allow operation at temperatures as low as 100 K.[11]

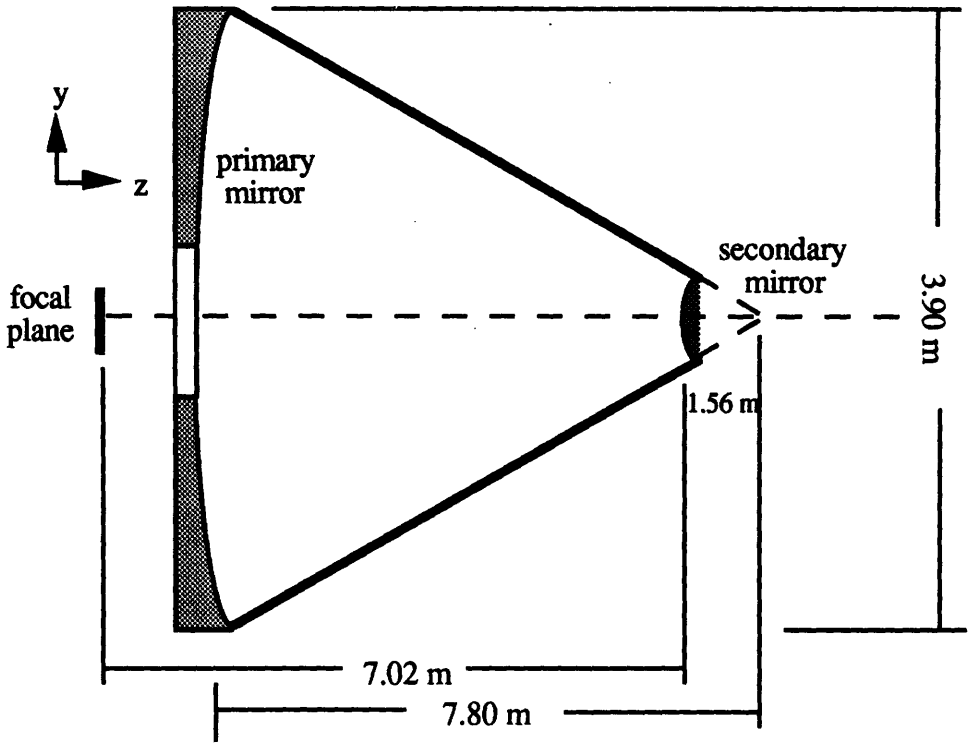

Figure 2-2
Cassegrain Reflector Configuration (not to scale)

With the dimensions and configuration of the hypothetical reflector defined, analyses are now performed to determine the reference operating parameters.

2.2 Diffraction Limited Resolution

The following section calculates the reflector's ability to resolve pairs of nearby objects assuming that the limiting factor on the image sharpness is the interference between the diffraction patterns of the two objects. Diffraction limited analysis is performed for objects of both similar and dissimilar brightnesses.

---

[11]Rapp (1992), pp. 4-11 to 4-25.

2.2.1 *Objects of Similar Brightness*

When a celestial object such as a star is viewed through a reflector, the collected energy is scattered in an Airy pattern over the focal plane. The Airy pattern is described by:

$$I(x) = \left[\frac{2J_1(\pi x)}{\pi x}\right]^2 \tag{2.2}$$

where J_1 is a first order Bessel function, and x is the non-dimensional off-axis distance from the peak at x = 0.[12] The angle θ corresponding to x is:

$$\theta = x\frac{\lambda}{D} \quad \text{(radians)} \tag{2.3}$$

where λ is the operating wavelength in microns, and D is the primary reflector diameter in meters. As can be seen in Figure 2-3, the primary peak at x=0 has a value of 1, with subsequent peaks falling off very rapidly in value. The first "zero" of the pattern occurs at x = 1.22.

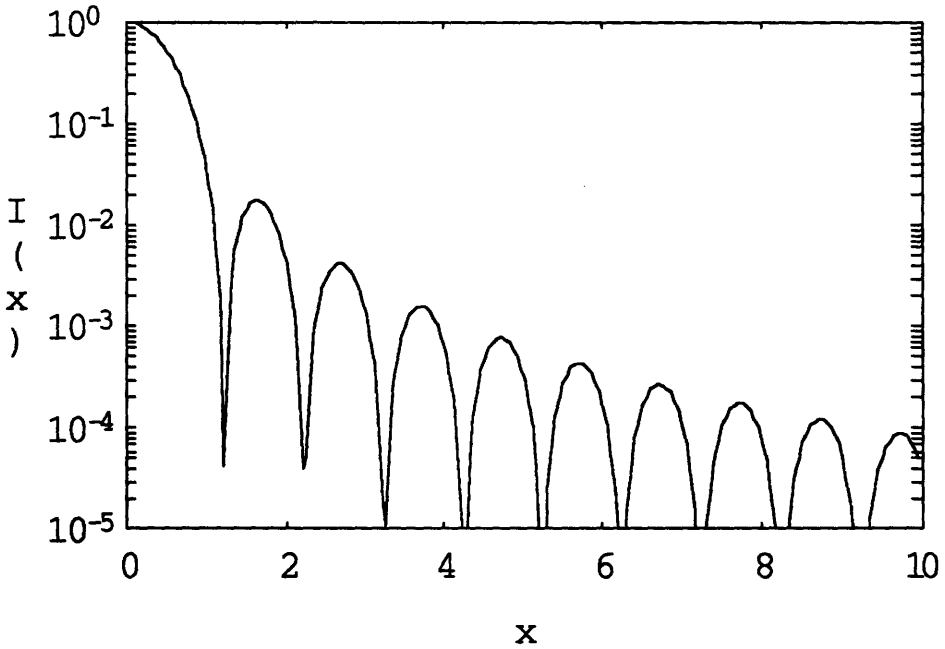

Figure 2-3
Airy Diffraction Pattern

---

[12]Goodman, J. W. *Introduction to Fourier Optics*, McGraw-Hill, 1968, pp. 64-66.

For two nearby objects of similar brightness, such as companion stars in a binary system, the closest distance at which the peak of the second object can be detected is assumed to be at this "zero" in the pattern of the first. Therefore, the minimum angular separation required for resolution, according to Eq. 2.3, is:

$$\theta = 1.22\frac{\lambda}{D} \qquad \text{(radians)} \qquad (2.4)$$

This minimum angular separation is known as the "Rayleigh criterion".

In the detection of small secondary objects around a much larger and brighter primary object, such as a planet around a star, the Rayleigh criterion fails due to the great difference in intensities of the two objects. A new criterion must be derived to account for this difference.

2.2.2 Objects of Very Dissimilar Intensities

A new resolution criterion was developed by Black to estimate the minimum resolution required between two objects as a function of their relative intensities[13]. Black integrated the image intensity of the brighter object over the Airy pattern, and determined its average value as a function of spatial separation. The new criterion was then developed under the assumption that the peak intensity of the dim object's image was at least equal to the average intensity of the diffraction wing of the bright object. From this, Black determined the new criterion to be:

$$\theta = 0.3451\left(\frac{I_{bright}}{I_{dim}}\right)^{1/3}\frac{\lambda}{D} \quad \text{(radians)} \qquad (2.5)$$

and will be referred to as "Black's Law". This law retains the proportionality with respect to wavelength and diameter, but now is also proportional to the cube root of the intensity ratio between bright and dim objects. Figure 2-4 illustrates the predicted resolutions of both Black's Law and the Rayleigh criterion vs. intensity ratio. The two curves intersect at an intensity ratio of 43. Thus, the resolution of systems with intensity ratios less than 43 will determined by the Rayleigh criterion. Under this criterion, the minimum angular

---

[13]Black, D. "In Search of Other Planetary Systems", Space Science Reviews #25 (1980), pp. 35-81.

resolution of the reflector is 3.11 μradians, or 0.641 arcseconds for an operating wavelength of 10 μm.

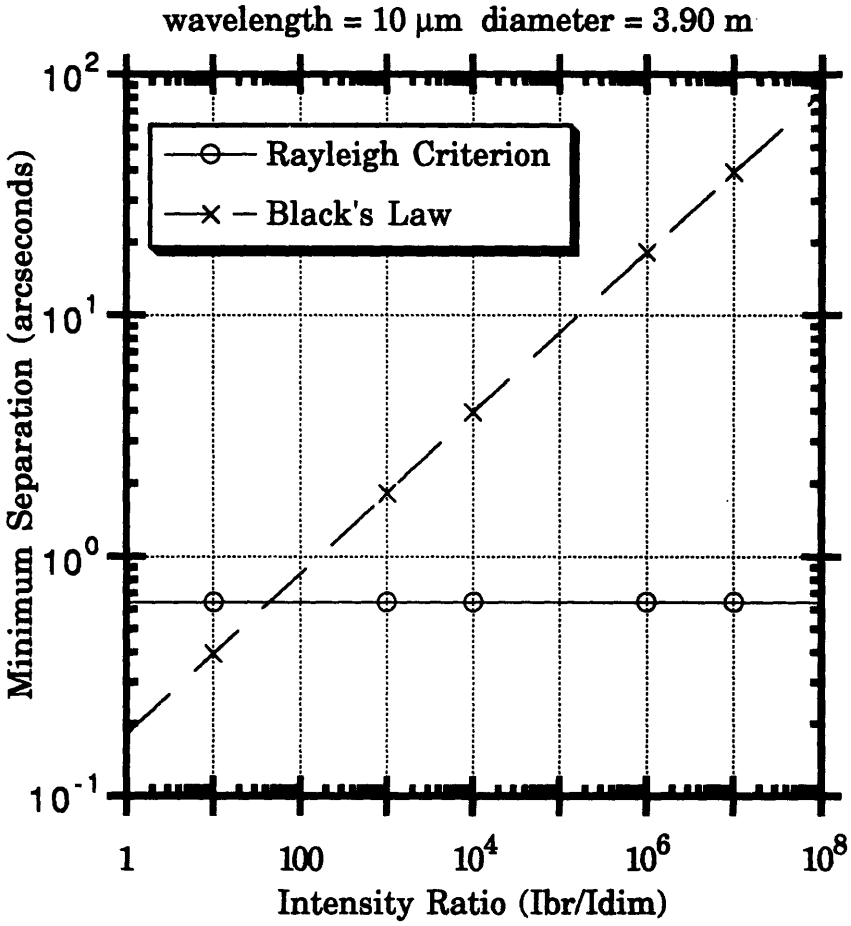

Figure 2-4
Black's Law vs. Rayleigh Criterion

Black's Law was rederived assuming that the peak intensity of the dim object was at least equal to the local peak (rather than the average) value of the bright object diffraction pattern. Under this assumption, the revised Black's Law becomes:

$$\theta = 0.5236\left(\frac{I_{bright}}{I_{dim}}\right)^{0.3104}\frac{\lambda}{D} \text{ (radians)} \qquad (2.6)$$

Figure 2-5 shows only a minor difference in the two curves, although the revised Law has a minimum applicable intensity ratio of 15, rather than 43. This new derivation requires that the peak object-to-background ratio for the dim object will be at least equal to 1.0.

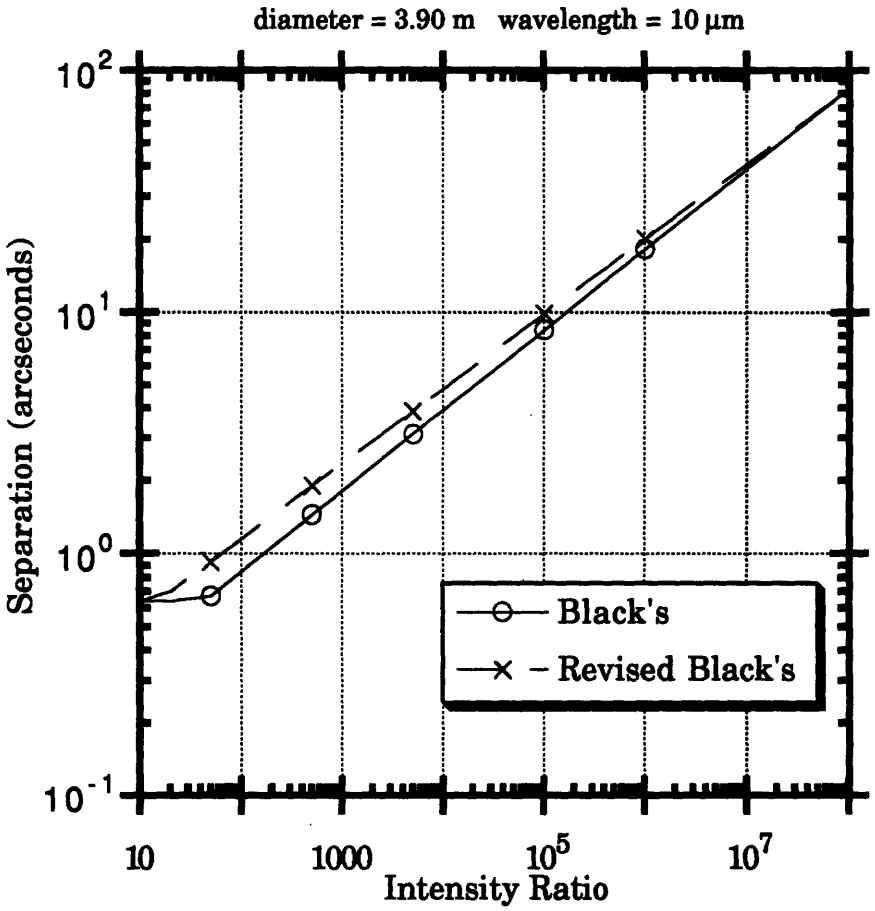

Figure 2-5
Black's Law - Original vs. Revised

2.2.3 Calculation of Object Intensities

Now that the diffraction limited resolution criteria have been developed, the object intensities must be quantified for comparison. In this analysis, we will deal with the example of a brown dwarf around a nearby star (see Appendix A.1 for a list of star systems within 6.5 parsecs from the Sun). The photon output from a brown dwarf can be expressed as:

$$N_{dwarf} = \frac{2\eta A_d A_t \nu^2 \Delta\nu \varepsilon_d t}{R^2 c^2 \left(e^{\frac{h\nu}{kT}} - 1\right)} \quad \text{(photons)} \qquad (2.7)$$

k = Boltzmann's constant (J/K)
A_d = disc area of object (m^2)
ν = signal frequency (Hz)
ε_d = object emissivity
R = distance to object (m)
T = object temperature (K)
η = detector efficiency ≈ 0.5
A_t = reflector collection area (m^2)
$\Delta\nu$ = bandwidth (Hz) = 0.3ν
t = integration time (sec)
c = speed of light (m/s)
h = Planck's constant (kgm^2/s)

This equation can also be used to calculate the object signal from a star.[14] Figure 2-6 illustrates this distribution as a function of wavelengths for several stars and brown dwarfs. The peak on each curve indicates the point of maximum output of photons.

[14]Rapp, D. "Direct and Indirect Detection of Extra-Solar Planets and Brown Dwarfs: A Survey Report Written for Non-Specialists", 1990, pp. 3-2 to 3-5.

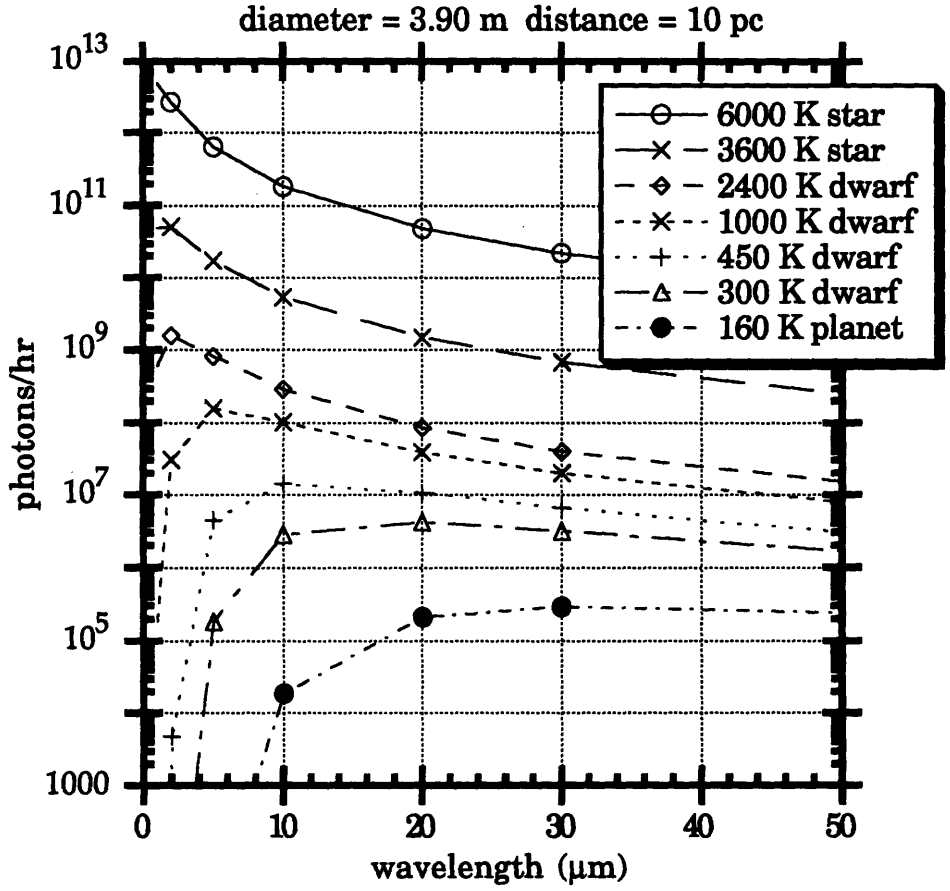

Figure 2-6
Calculated Photon Signals for Various Bodies

The signals from a star and brown dwarf can be converted to ratios with respect to one another, and resolutions determined via Eq. 2.5. Assuming that brown dwarfs are found in orbit about a star, the ratios are taken only between a star and a brown dwarf. Figure 2-7 illustrates the resolution required for detection of various dwarfs around a 3600 K star as a function of wavelength.

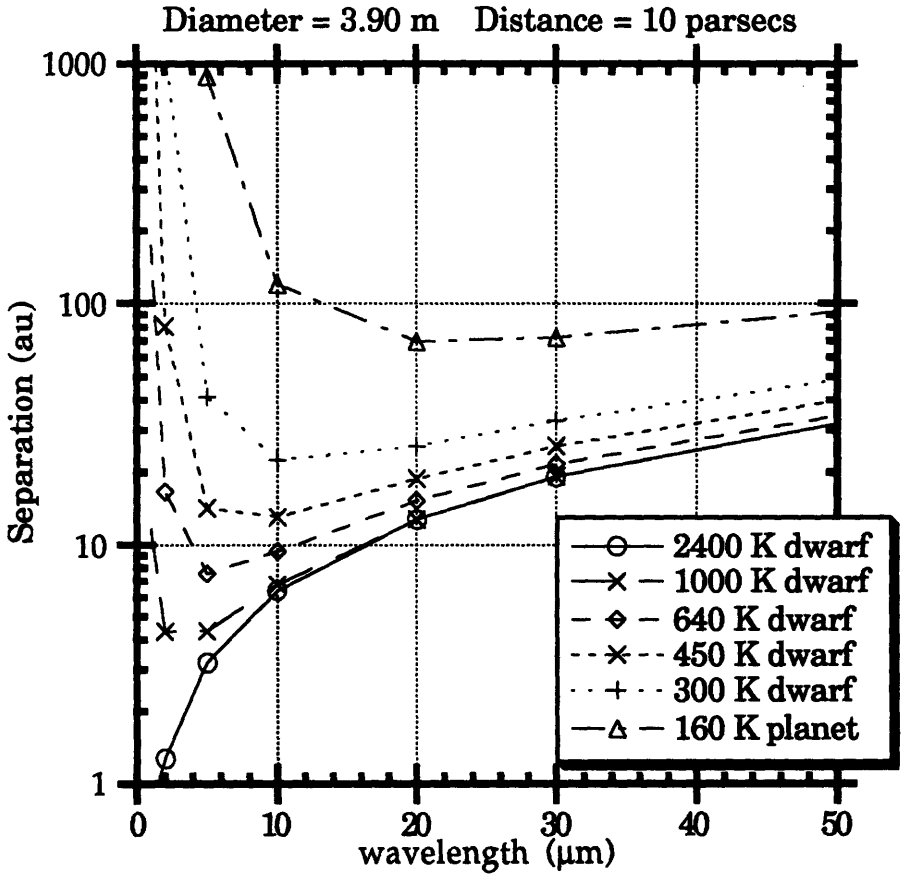

Figure 2-7

Minimum Detectable Object Separation vs. Wavelength for a 3600 K Star

Several interesting points can be drawn from Figure 2-7. The very rapid increase in minimum required separation at shorter wavelengths is due to a dramatic increase in intensity ratios. As can be seen in Figure 2-6, stars emit most of their energy in the visible spectrum, whereas dwarfs emit strongly in the near infrared. At longer wavelengths, the intensity ratio approaches a constant, but the minimum separation increases proportionately to the longer wavelength. A minimum angular separation appears in most of the curves near 10 μm, where the intensity ratio is close to the long wavelength asymptote, but the wavelength has not yet grown too large. Table 2-1 gives minimum angular resolution values for other stars at wavelengths of 10 μm and 20 μm.

Table 2-1 Angular Resolution for Various Brown Dwarfs and Stars

All values in arcseconds						
	2400 K dwarf	1000 K dwarf	640 K dwarf	450 K dwarf	300 K dwarf	160 K planet
6000 K star						
10μm	1.56	2.21	3.05	4.26	7.34	39.09
20 μm	3.01	3.92	4.91	6.05	8.25	22.37
3600 K star						
10μm	0.64	0.68	0.94	1.31	2.26	12.03
20 μm	1.28	1.28	1.53	1.89	2.57	6.98
3360 K star						
10μm	0.64	0.64	0.68	0.95	1.65	8.80
20μm	1.28	1.28	1.28	1.38	1.88	5.12

2.3 Signal-to-Noise Ratios

Inherent in any optical system is background noise which shrouds weak signals that may otherwise be detected. Background noise has many sources, all of which fall into two categories: spatially uniform and non-uniform. The following sections describe and quantify both types of noise, and give object signal to background noise ratios over various operating parameters of the reflector.

2.3.1 Uniform Noise

Uniform noise can be placed into four categories: cosmic background, zodiacal dust emission, scattered sunlight, and telescope noise. Cosmic background noise is the remnant energy from the Big Bang; zodiacal dust emission is evenly distributed matter in the galaxy; scattered sunlight is solar radiation reflected off interplanetary dust, and telescope noise is energy emitted by the telescope itself due to its own temperature. Each type of uniform noise can be expressed by:

$$N_{un} = \left[8\eta\Delta\nu\varepsilon t\left(e^{\frac{h\nu}{kT}} - 1\right)^{-1}\right]^{0.5} \quad \text{(photons)} \qquad (2.8)$$

cosmic: $\varepsilon = 1$, T = 2.7 K

zodiacal dust: $\varepsilon = 10^{-7}$, T = 275 K

scattered sunlight: $\varepsilon = 6 \times 10^{-14}$, T = 5500 K

telescope: $\varepsilon = .05\left(\frac{100}{\lambda_{\mu m}}\right)^{0.5}$, T = variable

Much like the object signal, noise is highly sensitive to changes in temperature. In addition, telescope emissivity is wavelength dependent. In the near infrared, the predominant noise sources are telescope and zodiacal dust. A fortunate aspect of uniform noise is that it increases with the square root of time, whereas the object signal increases linearly with time. Thus, longer integration times are desirable in order to achieve higher signal-to-noise ratios[15].

2.3.2 Non-Uniform Noise

Non-uniform, or cirrus, noise is due to the discontinuous distribution of galaxy clusters in the universe. Because of its non-uniformity, cirrus noise cannot be statistically subtracted from the object signal, and so increases linearly with time, as well. Cirrus noise can be crudely approximated as:

$$N_c \approx 10.5\lambda_{\mu m} D^{-0.5} t \qquad \text{(photons)} \qquad (2.9)$$

where D is the reflector diameter in meters. Cirrus noise becomes significant only at wavelengths of 30 μm or greater.

---

[15]Rapp, et al.

2.3.3 *Analysis Results*

With both object and noise signals quantified, signal-to-noise ratios can be analyzed as a function of several parameters. The parameters of greatest interest are integration time, wavelength, and telescope temperature.

With telescope temperature and wavelength fixed, the signal-to-noise (S/N) ratio can be examined as a function of integration time (Fig. 2-8). At a wavelength where cirrus noise is negligible (10 μm), S/N ratios increase with the square root of time above t = 10 seconds. Assuming that the minimum required S/N ratio is 1, the minimum integration time for a 300 K dwarf is ≈ 100 seconds. If the telescope temperature is higher, however, these ratios fall off sharply, requiring longer integration times.

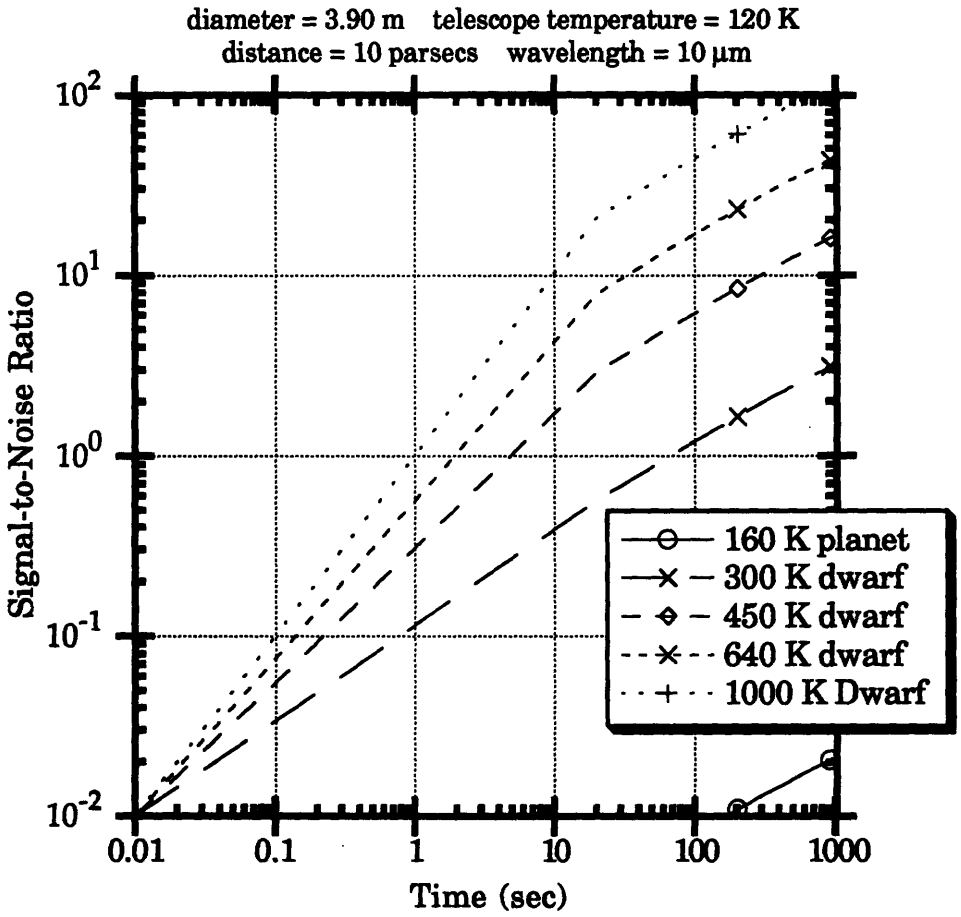

Figure 2-8
Signal-to-Noise Ratio vs. Integration Time

Looking at S/N ratios as a function of wavelength, again the range between 5 μm and 10 μm give the best results (Fig. 2-9). Shorter wavelengths greatly diminish the object signal strength, whereas longer wavelengths (>30 μm) suffer from the effects of increased cirrus noise. The values in Figure 2-9 reflect an integration time of 1 hour. At t = 1000 seconds, S/N ratios would still be high enough for fairly easy detection of dim secondary objects.

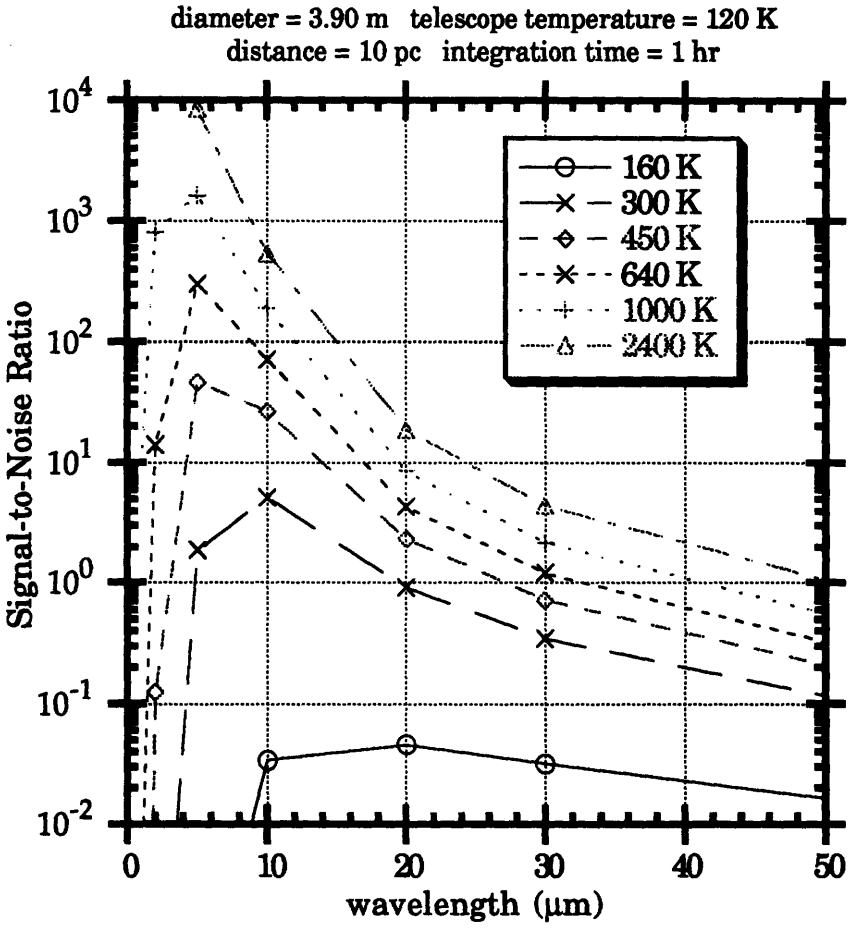

Figure 2-9
Signal-to-Noise Ratio vs. Wavelength

The final parameter of analysis is telescope temperature. At an integration time of 1000 seconds, the S/N ratio as a function of brown dwarf temperature is shown in Figure 2-10. Setting the minimum S/N ratio equal to 1, there is little to be gained in cooling the reflector from 120 K to 80 K. A reflector operating ≈ 120 K could detect a dwarf at 250 K, which is sufficient for this analysis. Detection of a planet-like object at a temperature of 150 K

would require telescope temperatures below 50 K, thereby posing greater demands on passive cooling technology.

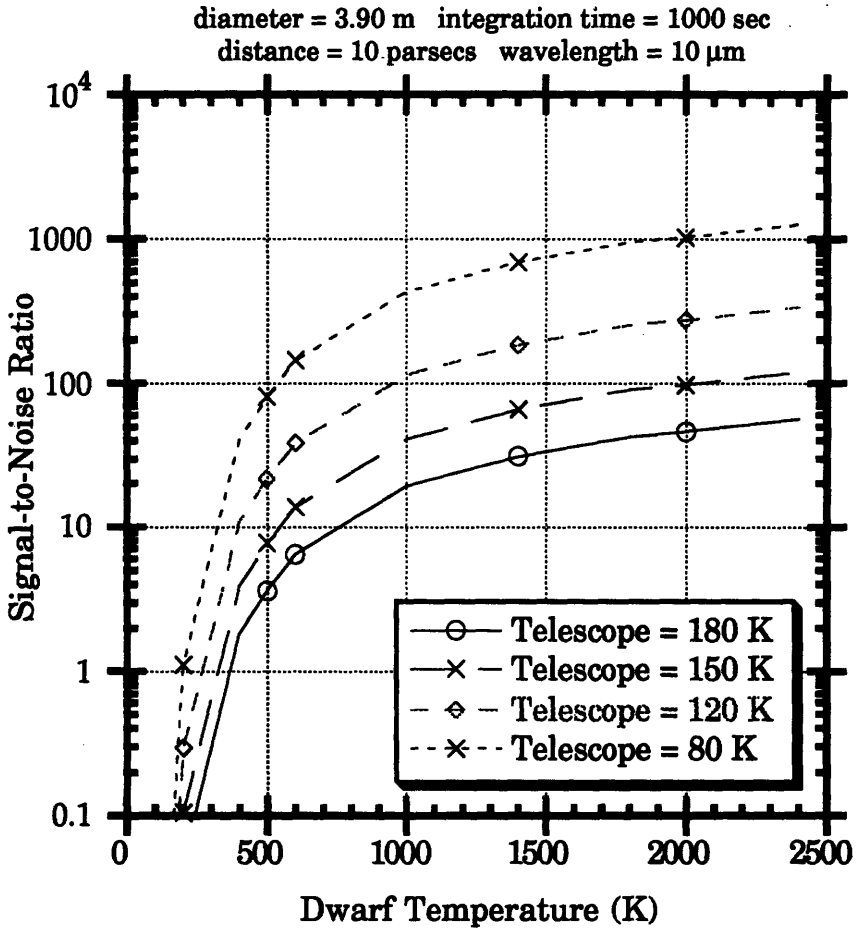

Figure 2-10
Signal-to-Noise Ratio vs. Dwarf Temperature

A final comparison is made between telescope and the external noise sources. As telescope noise is the only controllable noise source, it would be pointless to cool the reflector below a point where the telescope noise was less than that of the remaining sources. Figure 2-11 reinforces the fact that operation at a telescope temperature below 100 K does not significantly improve signal-to-noise ratios for dwarfs at 250 K or higher. At an operating wavelength of 10 μm, integration times > 1000 seconds require a telescope temperature of 100 K to reach the noise floor of the system. Longer wavelengths would require colder temperatures to meet the same requirement.

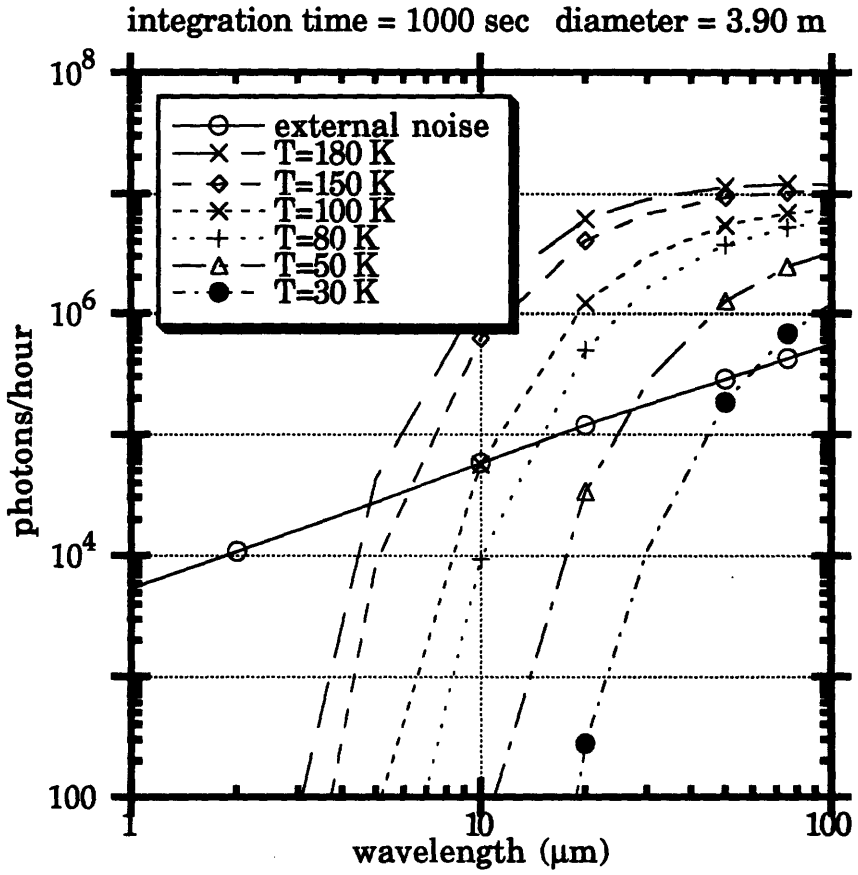

Figure 2-11
Comparison of External and Telescope Noises vs. Wavelength

2.4 Conclusion

In the determination of the reflector's nominal performance for detecting brown dwarfs, the issues of diffraction limited resolution and background noise were addressed. Minimum required angular resolution for various star/dwarf combinations was calculated under Black's Law. In addition, signal-to-noise ratios were evaluated over the primary operating parameters of wavelength, telescope temperature and integration time. From the above analysis, the selection of nominal values for the telescope operating parameters was made. An operating wavelength between 5 μm and 10 μm is ideal, as it allows for the best angular resolution in most cases while keeping S/N ratios sufficiently high at temperatures near 100

K. 10 μm is selected, because the control requirements for reflector surface precision are less stringent. A telescope temperature of 100 K is sufficient, keeping the telescope noise level below that of the external noise for integration times greater than 1000 sec. Finally, a minimum integration time of 1000 seconds is selected by default. The nominal values for resolution and signal-to-noise determined by these operating parameters set a point of reference for the analyses of the aberrated optical system.

Chapter 3

Optical Analysis

Chapter 3 deals with (1) the development of a closed analytic solution relating optical performance of the reflector system to surface aberrations in the primary reflector panels, and (2) the creation and implementation of an optical model of the reflector system. The closed analytic solution is derived for a chosen performance metric assuming linear perturbations in the panels. The optical model is created using a coordinate-free ray tracing program capable of accurately representing both the panel aberrations and the performance output. This model serves three main purposes. First, it is used to characterize the performance of the reflector system subject to rigid body deformations only. Second, it verifies the analytic solution through a comparison with numerical results from the rigid body characterization. Third, it is used to characterize the reflector system's optical performance subject to higher order aberrations, thereby providing the observable "feedback" in a control scheme implemented to minimize the panel aberrations. The first step, however, is the selection of a performance metric.

3.1 Performance Metrics

Before an analytic solution could be developed, a measure of optical quality, or performance metric, had to be selected. Three such metrics are: Strehl ratio, signal-to-scattered light ratio, and encirclement of energy. The Strehl ratio is defined here as the ratio of the peak intensity of the image of a point source with aberration to the peak intensity of the image with no aberration, with values ranging between zero and one.[16] The Strehl ratio (SR) is a commonly used performance metric, and is a good indicator of the sharpness of a bright central image. The second performance metric is the signal-to-scattered light (SSL) ratio. This is the ratio between the intensity of an off-axis point image of a dim object and the intensity of light scattered from the bright central image at that off-axis point, and ranges between zero and infinity. SSL ratio is potentially a good metric in the detection of dim objects around a bright source because it quantifies the possibility of detection under aberrated conditions. The last metric is encirclement of energy. This metric describes the

---

[16]Lawrence, G.N. *Applied Optics and Optical Engineering* (preprint), Eds. Shannon and Wyatt, Applied Optics Research. Tuscon, 1990. Pg. 46.

fraction of the primary image's total intensity within a given angular bandwidth. This also is a potentially useful metric in quantifying the level of scattering over secondary images. Strehl ratio was selected as the performance metric for this research for two reasons. First, it is easier to develop Strehl ratio into a closed analytic form than it is for encirclement of energy. Second, the SSL ratio solution is approximate at best, and would not provide the level of accuracy attainable with the Strehl ratio solution. This solution based on the Strehl ratio is now developed.

3.2 Linear Analytic Model

The closed analytic solution, also referred to as the linear analytic model, relates loss in optical performance in the reflector system to surface aberrations with Strehl ratio used as the figure of merit. The model is termed linear because it is assumed that the magnitude of the wavefront error produced by the aberration is small compared to the operating wavelength of the system. "Small" has been quantified by Borne and Wolf as approximately $\lambda/14$, with a resulting Strehl ratio of 0.8.[17] This will be verified within the optical model to be described later. The analytic model is derived first in an integral form, and then is implemented numerically.

3.2.1 Derivation

The model derivation begins with an observation of the image point spread function (PSF), a three dimensional expansion of the the Airy diffraction pattern shown in Figure 2-3. Defining pertinent terms as:

μ = mechanical displacement vector	μ^* = nominal displacement vector
r = small perturbation vector ($\|r\| << \lambda$)	$h(\mu)$ = PSF value at center
$W(\mu)$ = wavefront error	$W(\mu^*) = 0$

the PSF, assuming a small perturbation in the system, can be expanded to second order as:

$$h(\mu) = h(\mu^*+r) \approx h(\mu^*) + \nabla h(\mu^*)r + \frac{1}{2}r^T H(\mu^*)r \qquad (3.1)$$

---

[17]Borne, M., Wolf, E. *Principles of Optics: Electromagnetic Theory and Propagation, Interference and Diffraction of Light*, Pergamon Press, 1980, p. 469.

where **H** is the square Hessian matrix, describing the second derivative of the wavefront error W with respect to the displacement vector μ. Each term in **H** can be described by:

$$H_{ij} = 2k^2\left[-A\int_A \frac{\partial^2 W}{\partial\mu_i\partial\mu_j}\partial\sigma + \left(\int_A \frac{\partial W}{\partial\mu_i}\partial\sigma\right)\left(\int_A \frac{\partial W}{\partial\mu_j}\partial\sigma\right)\right] \tag{3.2}$$

where k is the wave number, $\partial\sigma$ is a differential surface element, and A is the collecting area of the reflector. For small perturbations about the nominal $h(\mu^*)$, representing a maximum point, the slope of the point spread function is zero. Therefore:

$$\nabla h(\mu^*) = 0 \tag{3.3}$$

leaving only the nominal PSF value and the second order Hessian. To obtain an expression for the Strehl ratio (SR), the expansion of Eq. 3.1 is normalized by the nominal PSF value:

$$SR = \frac{h(\mu^*+r)}{h(\mu^*)} \approx 1 + \frac{1}{2h(\mu^*)} r^T\mathbf{H}(\mu^*)r \tag{3.4}$$

The normalized Hessian, or S-matrix, is now defined as:

$$\mathbf{S} = \frac{1}{2h(\mu^*)}\mathbf{H}(\mu^*) \tag{3.5}$$

Each term in **S** can be expanded as:

$$S_{ij} = -k^2\left[\frac{1}{A}\int_A \frac{\partial^2 W}{\partial\mu_i\partial\mu_j}\partial\sigma - \left(\frac{1}{A}\int_A \frac{\partial W}{\partial\mu_i}\partial\sigma\right)\left(\frac{1}{A}\int_A \frac{\partial W}{\partial\mu_j}\partial\sigma\right)\right] \tag{3.6}$$

Eq. 3.4 can then be rewritten in vector form as:

$$SR = 1 + r^T\mathbf{S}r \approx 1 - k^2\left[\frac{\int_A (\nabla W\cdot r)^2\partial\sigma}{A} - \frac{\left(\int_A \nabla W\cdot r\,\partial\sigma\right)^2}{A^2}\right] \tag{3.7}$$

In Eq. 3.7, the first term in parentheses is a surface integral over the aperture representing the normalized wavefront error caused by the small perturbation r. The second term in parentheses represents the average wavefront deviation over the aperture. It is subtracted from the first as a component of the error which can be removed by a simple pistoning of the reflector surface.[18] Therefore, this definition for the Strehl ratio assumes an insensitivity to wavefront error caused by pure piston motion in the panels. This definition is now recreated for numerical implementation.

3.2.2 Discrete Model

In order to utilize the analytic form of the Strehl ratio, a discrete version must be formulated for numerical implementation. Defining new terms as:

n = number of data points sampling the aperture
m = number of degrees of freedom in optical model
$C_{ij} = \frac{\partial W_i}{\partial \mu_j}$ = change in wavefront at data point i with respect to change in degree of freedom j

Eq. 3.6 can be expressed discretely by:

$$S_{ij} = k^2\left[\frac{1}{n}\sum_{i=1}^{n}\left(\sum_{j=1}^{m} C_{ij}\right)^2 - \frac{1}{n^2}\left(\sum_{i=1}^{n}\sum_{j=1}^{m} C_{ij}\right)^2\right] \tag{3.8}$$

Rewriting Eq. 3.8 in matrix form:

$$\mathbf{S} = k^2\left[\frac{1}{n}\mathbf{C}^T\mathbf{C} - \frac{1}{n^2}\mathbf{M}\right] \tag{3.9}$$

where **C**, defined as the optical sensitivity matrix, has dimension n-by-m. **M**, defined as the mean matrix, is the outer product of the column sums of **C**, and has dimension m-by-m. The resultant S-matrix is negative definite, and acts as the reducing term in the Strehl ratio. An eigen-decomposition of the S-matrix reveals m normalized eigenvectors with corresponding eigenvalues describing the "normal modes" of the reflector panels. To

[18]Conversations with Mark Milman (JPL section 343), July - November, 1991.

determine the discrete expression for the Strehl ratio, consider any normalized perturbation vector in the system. This can be represented as a linear sum of the S-matrix eigenvectors:

$$r = \sum_{i=1}^{m} \alpha_i v_i \tag{3.10}$$

where v is an S-matrix eigenvector, and α is its corresponding coefficient. Inserting Eq. 3.10 into Eq. 3.7, the Strehl ratio can be expressed as:

$$SR \approx 1 + \left\langle S\left(\sum_{i=1}^{m} \alpha_i v_i\right), \left(\sum_{i=1}^{m} \alpha_i v_i\right) \right\rangle \tag{3.11}$$

Because the eigenvectors of S are normalized to unit length, the inner product of the eigenvectors with themselves leaves only their coefficients squared multiplied by their respective eigenvalues λ_i. Therefore, Eq. 3.11 can be restated as:

$$SR \approx 1 - k^2\left(\sum_{i=1}^{m} \alpha_i^2 \lambda_i\right) z^2 = 1 - (kz)^2 \Lambda \tag{3.12}$$

The variable z is a scaling factor which represents the Euclidean norm (magnitude) of r. It is apparent that the reduction in Strehl ratio is proportional to Λ, defined as the effective eigenvalue of the perturbation vector, and is quadratic with its norm z. Therefore, the eigenvalues of the system are a measure of the system's sensitivity to reduction in Strehl ratio. This will be verified in the following sections involving the optical model of the reflector system. In addition, a relationship between Strehl ratio and wavefront error will be developed.

3.3 Optical Modeling

With an analytic form of the Strehl ratio developed, a computational model of the optical system is required to verify the accuracy of the analytic form, as well as provide a direct means to observe the effects of surface aberrations on image quality. A program recently developed at the Jet Propulsion Laboratory provides such a model. The Controlled Optics Modeling Package (COMP) generates mathematical elements representing optical surfaces within a system, and utilizes geometric coordinate-free ray tracing methods to propagate

rays of light through the system.[19] These rays, assumed to be collimated (parallel) due to the far-field nature of astronomical observations, effectively simulate a wavefront of light impinging on the primary mirror. Amongst its many applications, COMP is capable of calculating both optical pathlength difference (OPD) and point spread function (PSF) images for an optical system. Both are valuable in quantifying the quality of an image. Through scalar diffraction analysis, OPD maps determine the wavefront error of an aberrated system. PSF maps are three dimensional representations of the image at the focal plane, and directly provide information on both Strehl ratio as well the distribution of energy across the image plane.[20] Figure 3-1 illustrates the PSF map of a nominal single star diffraction pattern generated by a hexagonal segmented reflector.

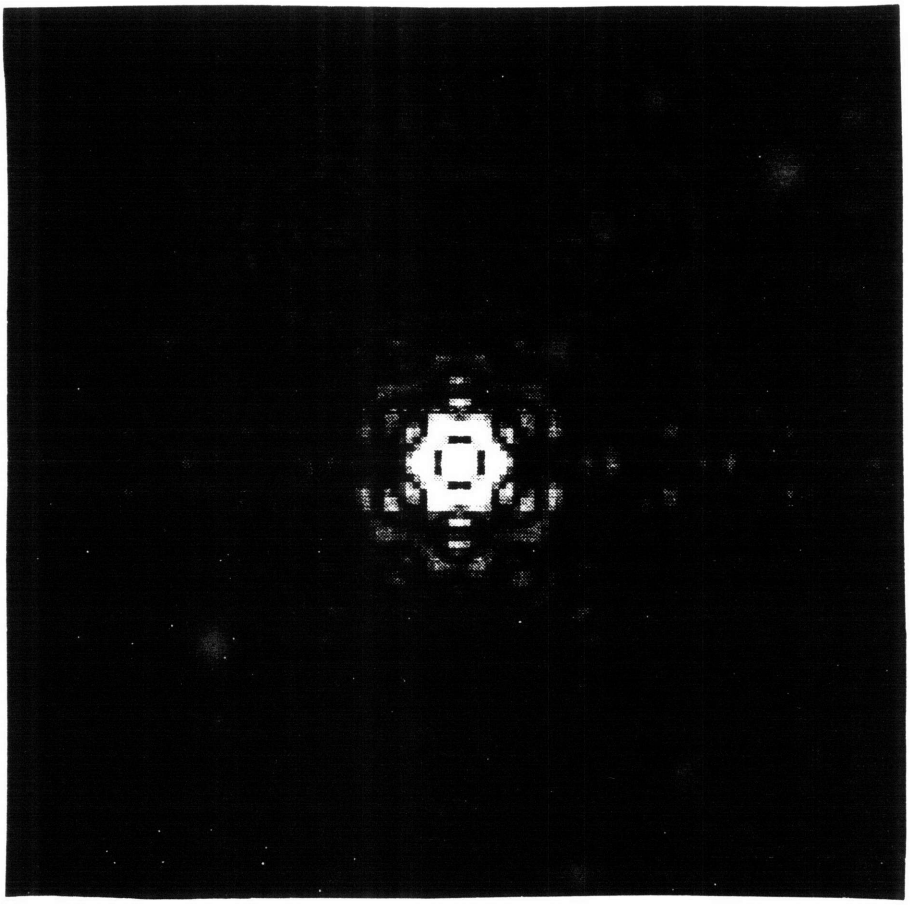

Figure 3-1
Point Spread Function Map

---

[19]Redding, D., Breckenridge, W. "Optical Modelling for Dynamics and Control Analysis", AIAA paper courtesy of C.S. Draper Laboratory, 1990, pp. 2-4.

[20]Redding, D. *Controlled Optics Modelling Package User Manual*, release 1.0, Jet Propulsion Laboratory, October 22, 1991, pp. 9-13.

The following sections describe two models of the optical system created within COMP. The first, low order model is used to validate the linear analytic form assuming small perturbations. The second, higher order model is the actual model used in the control scheme.

3.3.1 Low Order Model

Both optical models developed within COMP are identical in dimension and configuration to that described in section 2.1. The only "physical" addition to the model is that of a spherical reference surface located just after the secondary mirror. This surface is merely a mathematical tool needed to calculate the wavefront error, and is not an actual element in the system (Fig. 3-2).

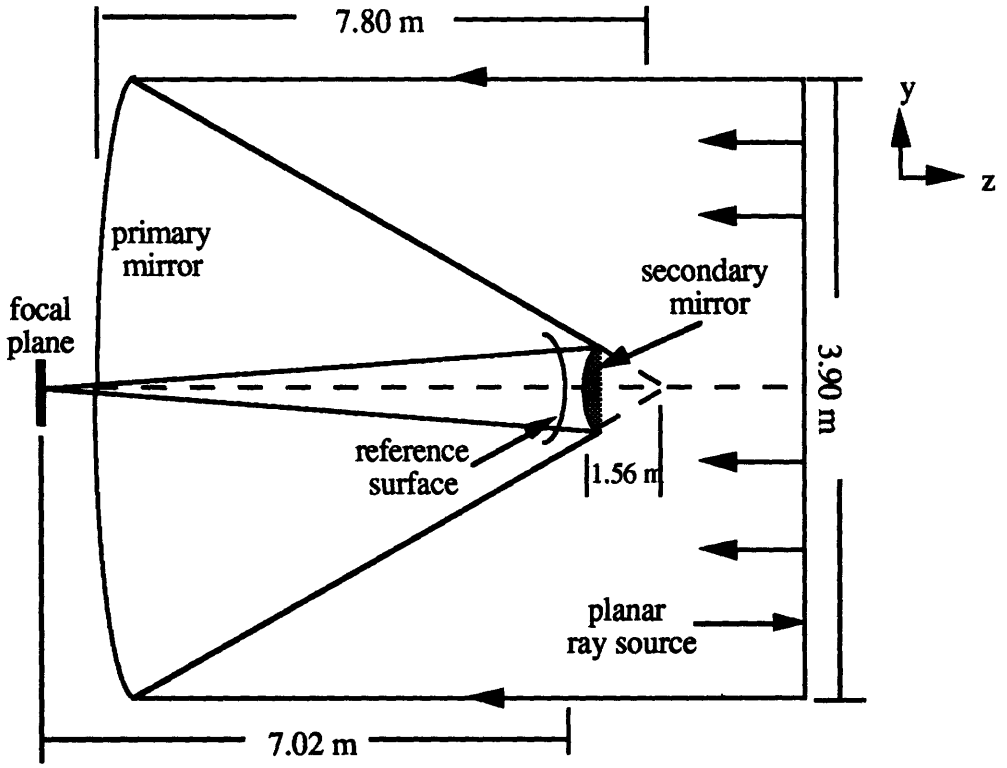

Figure 3-2
COMP Model Configuration

The low order optical model samples the reflector surface using 120 evenly distributed rays, corresponding to 15 rays across the maximum aperture of 3.90 meters. The seams between panels are assumed to have zero width. To avoid computational difficulties, the seventh central panel was left in this model. All perturbations occur within the primary

mirror elements only. The other optical elements are assumed fixed. Each of the seven panels is allowed six independent rigid body degrees of freedom. Perturbations act at the center of each panel about the global coordinate system, as shown in Figure 3-3. These rigid body motions are used in the initial characterization of the optical system described below. Appendix A.2 contains the COMP input code defining the low order model. The analysis methods used in COMP for the characterization of the reflector system are now discussed.

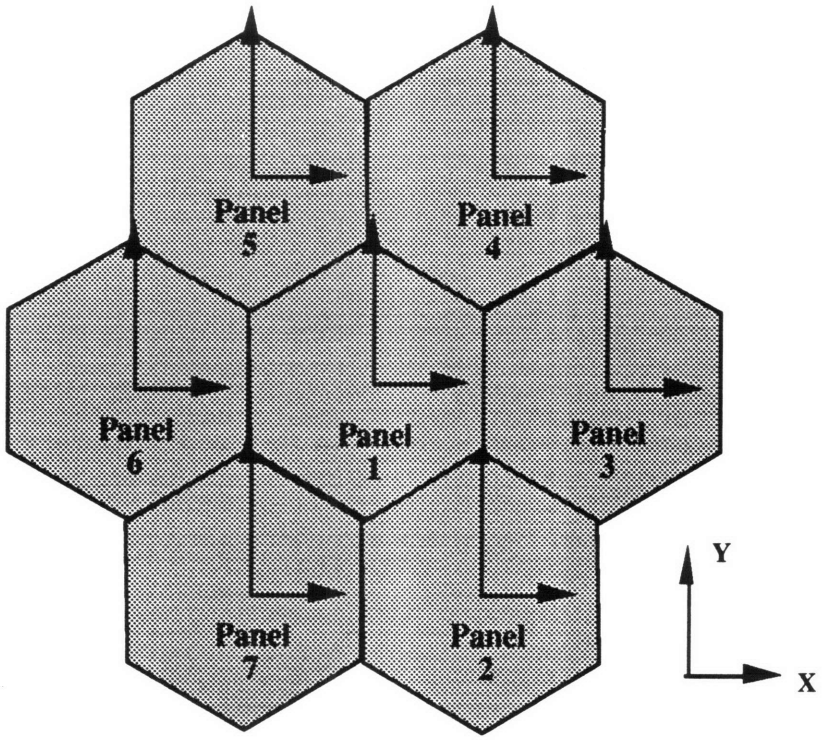

Figure 3-3
Low Order Panel Layout

3.3.1.1 Linear and Full Ray Trace Optical Analysis

Within the COMP program, there are two ways to characterize the performance of an optical system. First, the full ray trace method generates as a source a rectangular grid of parallel rays representing a sampled wavefront of light. The rays are assumed parallel because of the great distance to the objects of observation (stars and dwarfs). These rays are propagated from the source through all the intermediate optical elements to the spherical reference plane using Fresnel diffraction algorithms. The algorithms provide information on the magnitude and phase of the rays. A Fast Fourier Transform (FFT) algorithm is then applied to the sampled information over the reference surface, from which PSF and

wavefront data are generated.[21] When an aberration is introduced into the optical elements, the rays are deflected along different paths, thereby altering the character of the original wavefront. The full ray trace method is considered very accurate in describing the effects of physical perturbations in the system, including nonlinear errors, where the error magnitude is equal or greater than the operating wavelength. However, the FFT is effective only when the spatial frequency of the sampling rays is several times that of the surface errors. In large systems, this may require many thousands of rays, and is computationally expensive. A faster and cheaper alternative for some cases is found in differential, or linear, ray tracing.

Linear ray tracing offers the advantage of being computationally cheaper than the full ray trace method, and is very useful in characterizing a system's performance when the errors are small relative to the operating wavelength. Rather than compute an FFT over the reference surface, the linear method utilizes an optical sensitivity matrix, the C-matrix discussed previously in section 3.2.2, to determine the effects of surface aberrations on optical performance. This matrix is in essence an analytic linear transformation between the ray state and the aberration. It relates changes in the optical element degrees of freedom, defined by a 6-vector of rigid body motions, to the state of each ray, defined by a 3-vector (forward and transverse aberration, and pathlength error). From the ray state, OPD and PSF information is obtained.[22] Although useful primarily for analyzing small perturbations, the linear ray trace methods may potentially work for nonlinear errors in systems which display little sensitivity to physical perturbations. A comparison, therefore, was conducted between the linear and full ray trace methods using the described optical system to determine the range of errors over which the two methods were close in their predictions.

The comparison involved the evaluation of Strehl ratio (SR) and wavefront error (WFE) at increasing magnitudes of an input aberration. SR and WFE were evaluated using each ray trace method, and the values were compared. Results showed a very close approximation of the linear ray trace method to the full ray trace method for aberrations with magnitudes up to 50 μm (5λ). Over this range of aberration magnitude, the difference in both WFE and Strehl ratio between the two methods was less than 1% (see Appendix A.3). This indicates that at least for the optical system under examination, linear approximations of the

---

[21]Redding, et al.

[22]Redding, et al.

optical sensitivity matrix is sufficient to characterize the system's behavior subject to panel aberrations. The optical behavior of the reflector model is now characterized through the decomposition of the linear analytic sensitivity matrix.

3.3.1.2 Model Characterization

The characterization of the low order model involved the eigen-decomposition of the optical sensitivity S-matrix, described by Eq. 3.9. The S-matrix, rather than the original C-matrix, was used because of the assumption that pure unidirectional piston motion in all the panels could be removed without the use of the surface mounted actuators. COMP commands allow transfer of the linear C-matrix to a Matlab file, from which the S-matrix was generated and decomposed into 42 eigenvectors and corresponding eigenvalues, one for each degree of freedom of the primary reflector. These eigenvectors represent the "normal modes" of the reflector system, describing those combinations of motions in the panels which are most detrimental to the Strehl ratio. The eigenvalues represent their relative strengths in degrading the Strehl ratio. Table 3-1 highlights the seven most prominent eigenvectors. The notation + piston and - piston signify pistoning along the positive and negative z direction, respectively; + rot x represents positive rotation about the x axis.

Table 3-1 Low Order S-Matrix Eigenvalues and Associated Motions

	Primary Motions						
Eigenvalue	**Panel 1**	**Panel 2**	**Panel 3**	**Panel 4**	**Panel 5**	**Panel 6**	**Panel 7**
.6364	none	none	none	none	+ piston	none	- piston
.6073	none	- piston	- piston	- piston	+ piston	+ piston	+ piston
.5589	none	+ piston	- piston	+ piston	- piston	+ piston	- piston
.5360	- piston	+ piston	none	+ piston	none	+ piston	none
.5347	none	- piston	none	- piston	none	+ piston	none
.5345	none	- piston	none	+ piston	none	none	none
.0837	+ rot x	none	none	none	none	none	none

From this table, it is readily apparent that piston motions are still the most detrimental to optical performance with respect to the Strehl ratio. The piston motions are not in the same direction for all panels, however. In the first eigenvector, the symmetric panels 5 and 7 piston equally in magnitude but in opposite directions. The second eigenvector shows equal but opposite pistoning occurring on opposing sides of the reflector: panels 2, 3 and 4

recede while panels 5, 6 and 7 piston forward. The seventh eigenvector exhibits only a rotation about the x axis in panel 1. From its corresponding eigenvalue, it is apparent that this motion is much weaker than the piston motions. The subsequent 14 eigenvectors all show similar rotation motions in symmetric pairs of panels with equally low eigenvalues. The remaining 21 eigenvectors displayed motions which had near zero effect on optical performance. These motions were primarily rotation about the z-axis (normal to surface) and translation along the x and y axes, but also included one eigenvector representing near equal positive pistoning in all seven panels. In all cases, the motions were symmetric about the reflector's center. It should be noted that even for a symmetric arrangement of identical panels, panel position as well as the nature of the panel's deformation plays an important role in determining the aberration's impact on wavefront error. For example, the first and sixth eigenvectors listed in Table 3-1 perform identical motions on two sets of symmetric panels. Their corresponding eigenvalues, measuring their relative effects on wavefront error, are not equal, however. A possible explanation for this behavior is given in the error analysis of chapter 6.

It still remains to be shown whether the linear analytic solution for the Strehl ratio is an accurate representation of the system performance for small perturbations. Further tests were run in COMP, now comparing the validated linear ray trace model to the analytic solution.

3.3.1.3 Analytic Solution Verification

The linear analytic solution for the Strehl ratio was verified through a comparison with results from the COMP linear ray trace method. Several eigenvectors of the decomposed S-matrix were entered into the COMP model at increasing amplitudes z (error norm), and the Strehl ratio was recorded for each case. Figure 3-4 illustrates the comparison for the sixth eigenvector listed in Table 3-1, representing opposite piston motions in panel 2 and panel 4.

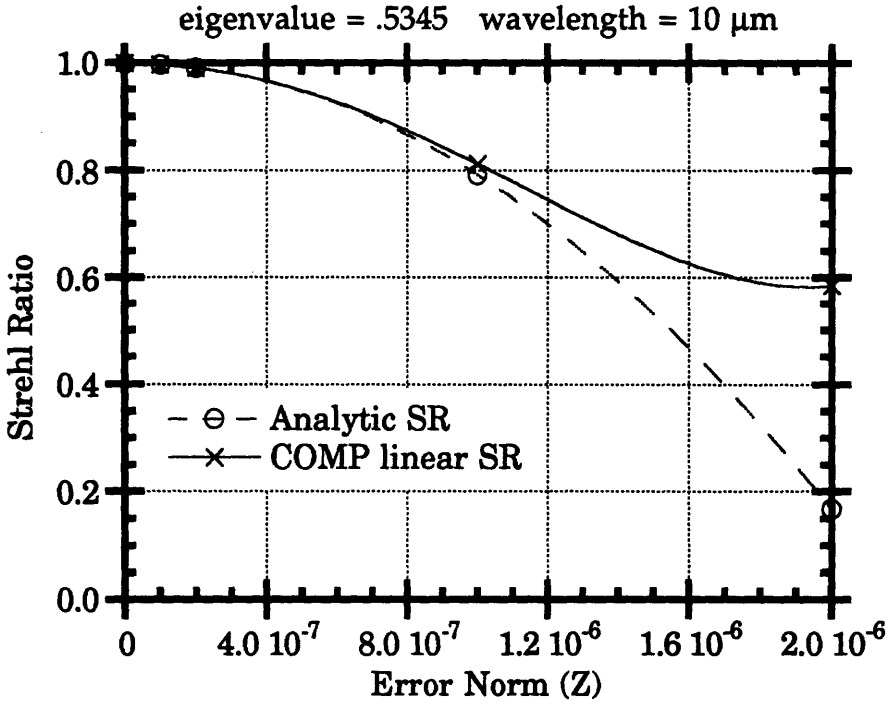

Figure 3-4

Strehl Ratio vs. Error Norm (Linear & Analytic)

The analytic solution follows the linear model closely down to a SR ≈ 0.8, at which point it begins to fall off rapidly. The Strehl ratio calculated by COMP tends to flatten out, and even increases at larger perturbation amplitudes as the image is refocused at a different point on the focal plane. Table 3-2 summarizes results from the remaining comparison tests.

Table 3-2 Comparison Between COMP Linear SR and Analytic SR Solution

Eigenvalue (#)	Error Norm ($z \times 10^{-6}$)	Analytic SR (#)	Linear SR (#)	Error in SR (%)	rms WFE (μm)
.031	4.05	0.8	0.824	2.93	0.721
.084	2.48	0.8	0.844	5.16	0.707
.288	1.34	0.8	0.827	3.29	0.714
.535	0.98	0.8	0.819	2.30	0.713
Operating wavelength = 10 μm					

In each case, the analytic solution tended to underestimate the true Strehl ratio. More importantly, however, these data verify the behavior previously stated by Born and Wolf with regard to rms wavefront error. In each case, the analytic SR = 0.8 when the WFE ≈ $\lambda/14$, in this case, 0.714 μm. From this information, an simple relationship between the two can be developed. Data collected during the comparison tests of the linear and full ray trace methods show that the slope $\partial WFE/\partial z$ is constant for a particular perturbation vector and associated eigenvalue. Plotting $\partial WFE/\partial z$ vs. eigenvalue (Λ), one obtains the relationship:

$$WFE = 0.9921\Lambda^{0.5}z \tag{3.13}$$

where WFE and z are described in equivalent units. Solving Eq. 3.17 for Λ, and substituting into Eq. 3.11, the Strehl ratio is now stated as:

$$SR \approx 1 - 40\left(\frac{WFE}{\lambda}\right)^2 \tag{3.14}$$

The analytic form of the Strehl ratio for small perturbations has now been verified against both the linear and full ray trace methods of COMP. The optical model within COMP is now further developed to allow analysis of higher order aberrations as they affect the Strehl ratio.

3.3.2 Higher Order Model

The higher order optical model was designed to allow more precise analysis of surface aberrations beyond those associated with rigid body motions. Higher order refers to the spatial frequency of a particular aberration. For example, a fifth order aberration displays regular variations in its shape five times across the surface. To better resolve these aberrations, the planar ray source within COMP sampled the reflector surface using 1289 rays distributed in a rectangular grid. At the maximum diameter of 3.90 meters, 48 rays span the aperture, corresponding to 16 rays across one panel. The new model does not have a seventh centrally located panel. This was done to simplify the structural modeling of the reflector elements, as discussed in chapter 4. To avoid computational difficulties, however, the code representing the seventh panel was left within the COMP model . The panel's "presence", however, was effectively eliminated by obscuring this element (i.e, preventing the rays impinging on it from propagating through the system) as well as

prohibiting any movement within its degrees of freedom (Fig. 3-5). Appendix A.2 contains the COMP input code defining the higher order optical system.

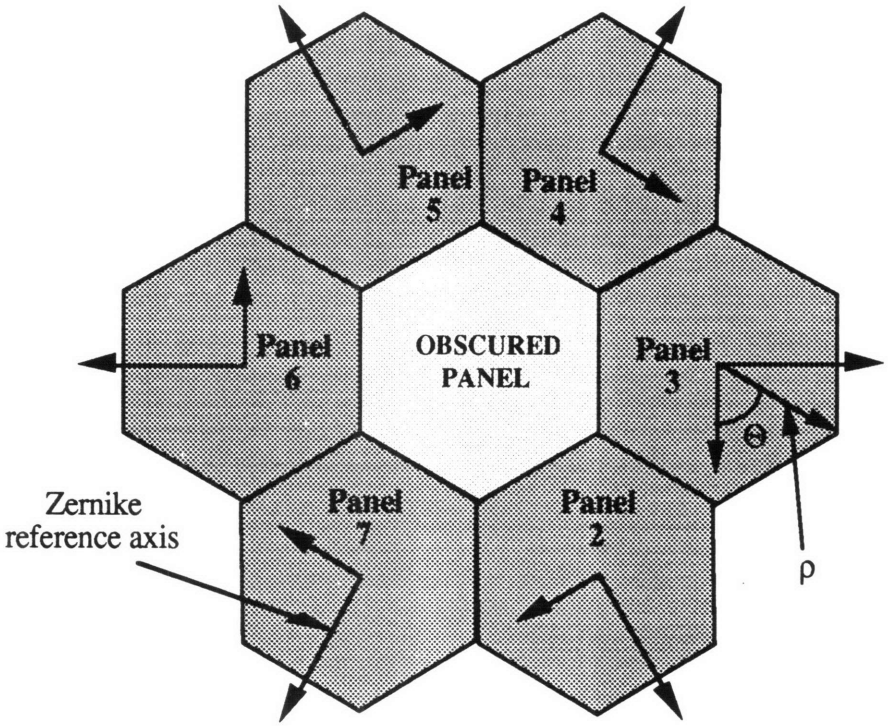

Figure 3-5
Higher Order Panel Layout

All perturbations occur within the six remaining primary mirror elements only. The other optical elements are assumed fixed. The surface displacement degrees of freedom within the new model are described by Zernike polynomials. Zernike polynomials and their implementation are now discussed.

3.3.2.1 Surface Representation through Zernike Polynomials

Zernike polynomials are an infinite series of orthonormal basis functions defined on the unit circle. Each Zernike can be expressed as the product of a radial and angular polynomial, defined over the unit circle. There is no unique definition for Zernikes, and several definitions have been used extensively.[23] However, some of these definitions generate a series of non-sequential Zernike terms, thereby making it difficult to fully

---

[23]Anderson, David. *Fringe Manual Version 3*. University of Arizona, Tuscon, 1982, pp. 11-13.

describe an arbitrary aberration whose components span several orders. Using a definition suggested by Malacara:

$$Z_n^{2m-n} = \sum_{s=0}^{m} (-1)^s \frac{(n-s)!}{s!(m-s)!(n-m-s)!} \rho^{n-2s} e^{i(2m-n)\theta} \tag{3.15}$$

$$e^{i(2m-n)\theta} = \begin{cases} \sin(2m-n)\theta, & 2m-n < 0 \\ \cos(2m-n)\theta, & 2m-n \geq 0 \end{cases}$$

where n is the order number (n: integer ≥ 0), ρ is the normalized radial distance ($0 \leq \rho \leq 1$), and m = 0,1,....n. Within each order, there are m = n+1 polynomial terms. Therefore, up through the kth order, there are (k+1)(k+2)/2 terms.[24] Any surface S can be approximated by a finite sum of these Zernike terms:

$$S(\rho,\theta) = \sum_{t=1}^{(n+1)(n+2)/2} C_t Z_t \tag{3.15}$$

where C_t is the Zernike coefficient.[25] The capabilities of COMP limited the use of Zernikes through the 7th order, for a total of 36 Zernike (Z) terms. Several of these are easily recognizable shapes. Z1 is simple pistoning, Z2 and Z3 are x and y axis tilts, and and Z5 is defocus. Although it is permitted in the characterization of the higher order reflector model, Z1 was fixed equal to zero for all test aberrations used in this research, as it was assumed that piston errors had already been removed. Figure 3-6 illustrates Z8, a first order coma along the x-axis, over the unit circle. Appendix A.4 lists the 36 Zernike polynomials used within COMP, with additional figures.

---

[24]Malacara, Daniel. *Optical Shop Testing*, John Wiley & Sons, Inc., New York, 1978, pp. 489-496.

[25]Anonymous. "View Zernike Coefficients - Surface Analysis", Breault Research, Inc., 1991, pp. 10-12.

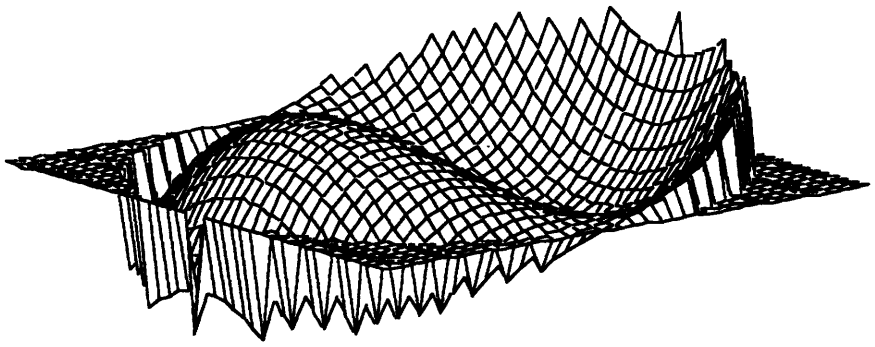

Figure 3-6
Zernike #8 (X-axis Coma) Over Unit Circle

As stated earlier, these terms are defined locally on each panel over a unit circle centered at the panel's rotation point. The reference axes are illustrated in Figure 3-5. These axes are defined such that the input of an identical error into each panel produces an azimuthally symmetric error over the entire aperture. Although COMP evaluates an image over the entire reflector aperture, local definition is required to resolve deformations on the panel level, as the error correction occurs on the panel level. For a 7th order aberration over one panel, a minimum of 14 sampling points across the panel is required to meet the Nyquist criterion.[26] The existing sampling rate of 16 points meets this criterion.

With the Zernikes described on the reflector surface, a characterization similar to that of the low order model must be done. The optical sensitivity S-matrix with respect to Zernike polynomials is now developed, through which the reflector system's performance subject to Zernike aberrations can be characterized.

3.3.2.2 Model Characterization

In section 3.3.1, the linear analytic optical sensitivity C-matrix for rigid body motions was developed. No such analytic form exists with respect to Zernike polynomials. Therefore, one was constructed via a finite difference approximation. Within COMP, a subroutine was written to input a fixed Zernike coefficient value C_t into a single Zernike term on each panel, the term being the same on each panel. The coefficient value was chosen as

---

[26]Lawrence, G.N., 1991, p. 24.

2×10^{-6}, because it was determined that the finite difference $\partial OPD/\partial C_t$ was constant in this range for all 36 Zernike terms. The rays were then propagated through the system using the full ray trace algorithm, and the OPD of each ray was evaluated. In this way, a numerical sensitivity matrix between ray OPD and Zernike degree of freedom was assembled. This sensitivity matrix differs from that of the low order model in three ways. First, the higher order C-matrix has a much finer mesh of ray points over the reflector surface to meet the need for better resolution of higher order aberrations. When fully assembled, it is a 1289-by-216 matrix. Second, as mentioned previously, the C-matrix is generated numerically whereas the low order matrix is analytic. Third, this matrix considers the change in OPD only, rather than an evaluation of a 3-vector ray state. These three differences may affect the accuracy of predictions of the Strehl ratio when the eigenvalues of the higher order S-matrix are implemented within the analytic solution to Strehl ratio. The eigen-decomposition of the numerical S-matrix is now considered.

As in the low order model characterization, the S-matrix rather than the C-matrix is decomposed because all purely unidirectional piston motions in all panels are assumed removed. The resulting decomposition produced 216 eigenvectors and corresponding eigenvalues. Again, the eigenvectors represent the "normal modes" of the reflector system, those aberrations which produce the greatest degradation of Strehl ratio. However, they differ from their low order counterparts in that they are 216-vectors describing changes in 36 Zernike polynomials over 6 panels rather than describing rigid motions alone. In fact, translation along the x and y axes and rotation about the z-axis are ignored by the higher order model. Table 3-3 highlights the properties of the six most prominent eigenvectors of the higher order S-matrix. The numerical values in each of the panel columns represent the term number of the Zernike polynomial.

Table 3-3 Higher Order S-Matrix Eigenvalues and Associated Motions

	Primary Motions (expressed in Zernike polynomials)					
Evalue	**Panel 2**	**Panel 3**	**Panel 4**	**Panel 5**	**Panel 6**	**Panel 7**
.6850	1,5,13,25	none	none	1,5,13,25	none	none
.6850	none	none	1,5,13,25	none	none	1,5,13,25
.6850	1,5,13 25	1,5,13,25	1,5,13,25	1,5,13,25	1,5,13,25	1,5,13,25
.6742	5, 2, 3,13	5, 2, 3,13	5, 2, 3,13	5, 2, 3, 3	5, 2, 3, 3	5, 2, 3,13
.6690	none	5, 2, 3,13	none	none	5, 2, 3,13	none
.2072	5,13	5,13	5,13	5,13	5,13	5,13

Table 3-3 indicates that the most prominent aberrations are composed of Z1, Z5, Z13 and Z25, representing piston, defocus, third and fifth order spherical, respectively. The first three eigenvectors, each with an eigenvalue of 0.6850, distributed these aberrations differently over the 6 panels yet produced equivalent results in terms of degradation to Strehl ratio. Each of these four terms has a piston component within it, perhaps explaining their predominance in the most detrimental eigenvectors, similar to that found for the piston error alone in the low order model. The fourth eigenvector exhibited an equal distribution of Z5, Z2, Z3 and Z13 over all panels, representing defocus, x and y axis tilts and third order spherical. Subsequent eigenvectors showed similar combinations of less damaging Zernike terms, such as Z8, Z9, Z18 and Z19, representing first and third order coma along the x and y axes. Contrary to the decomposition of the low order model, however, none of the higher order S-matrix eigenvectors have corresponding eigenvalues which are near zero, although eigenvalues beyond that of the sixtieth eigenvector are more than a factor of ten lower than the largest eigenvalue of 0.6850. To better understand the effects of individual Zernikes on reflector performance, additional analyses were performed.

A COMP subroutine was written to input individual Zernike terms as aberration vectors into each panel. The vectors were scaled to a norm equal to 2.0 μm, a value stated previously to lie in a range of constant $\partial OPD/\partial C_t$. For each aberration vector, an effective eigenvalue Λ was calculated, and both rms wavefront error and rms surface error were calculated through the COMP full ray trace algorithm. Figure 3-7 plots the normalized wavefront error produced by each Zernike aberration vector based on a linear relationship between WFE and aberration vector magnitude (z).

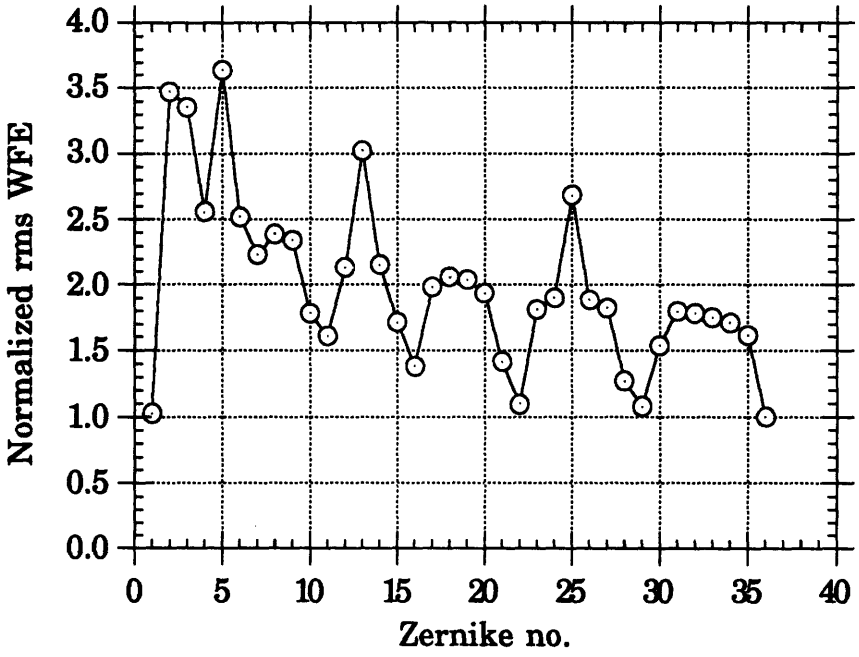

Figure 3-7

Normalized Wavefront Error vs. Zernike Term

The results of Table 3-3 are clearly illustrated in Figure 3-7. The individual Zernikes most detrimental to wavefront quality are Z5, Z2, Z3, Z13 and Z25, followed closely by Z4 and Z6. Z1 appears to have a relatively low effect on wavefront error. This is true when all panels piston equally in the same direction, because the S-matrix is insensitive to pure unidirectional pistoning. The appearance of Z1 in Table 3-3, however, is due to opposing pistoning motions in symmetric panels, similar to that shown in Table 3-1 for the low order model. The remaining Zernike terms analyzed show a steadily decreasing influence over wavefront error with increasing Zernike number, the lowest and highest wavefront error values differing by a factor of 3.7. Figure 3-8, illustrating normalized rms surface error vs. Zernike term, corroborates the observation that primarily the lower Zernike terms ($\leq$ Z6) most strongly affect the reflector's performance, increasing the surface error by more than a factor of two over the higher Zernikes. In comparing Figures 3-7 and 3-8, however, it should be noted that, with few exceptions, the effects of the Zernike terms on wavefront and surface errors follow a similar pattern. The exceptions come in at the wavefront error "wells", seen in Figure 3-7 near Z11, Z16, Z22 and Z29. These wells do not exist for the surface error plot, which exhibits a rather flat decline with increasing Zernike term.

Therefore, the wavefront error is less sensitive to aberrations in these Zernikes than is the surface error. This pattern in relative sensitivities of wavefront and surface errors to various Zernike polynomials may play a significant role in determining which control algorithm used for the correction of surface aberration is most effective.

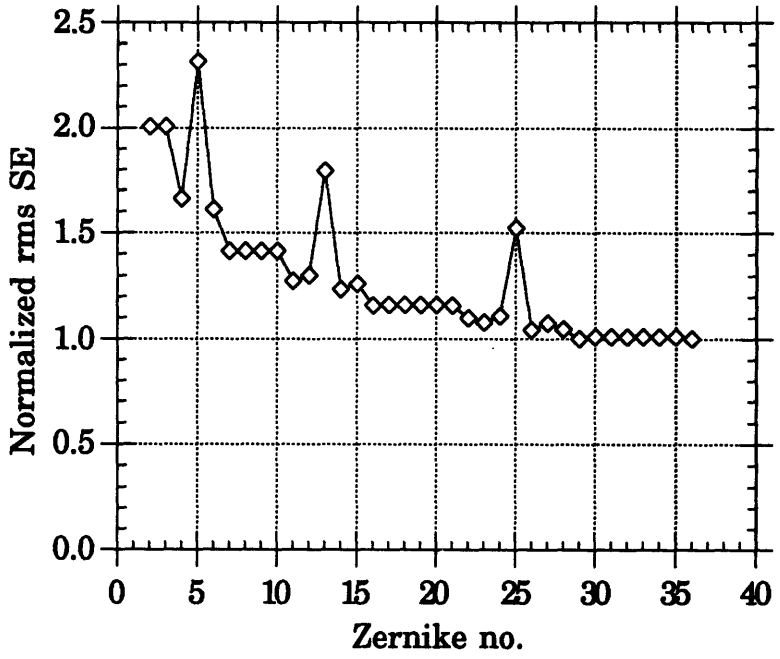

Figure 3-8
Normalized rms Surface Error vs. Zernike Term

3.4 Conclusion

Chapter 3 has developed several principal concepts for the optical analysis of a segmented reflector system. First, a closed analytic solution for the Strehl ratio was developed assuming linear perturbations in the system. Second, a low order optical model was created to (1) characterize those rigid body motions which most adversely affect Strehl ratio, and (2) verify the predictions for the Strehl ratio provided by the linear analytic solution. Linear and full ray trace analysis methods were compared for the low order model, and the linear method proved to be accurate for aberrations with magnitudes several times larger than the operating wavelength. The analytic solution was shown to be accurate to within 5% of the actual SR for rms wavefront errors up to $\lambda/14$. Third, a higher order

model using a finite expansion of Zernike polynomials to describe panel aberrations was developed and characterized through an eigen-decomposition of the optical sensitivity matrix. COMP provided information on wavefront and surface errors which resulted from individual Zernike aberration vectors. Analysis showed that several Zernike aberrations beyond piston and tilt errors exist which significantly degrade Strehl ratio, primarily higher order spherical aberration and defocus. In addition, a strong correlation between wavefront and surface errors was noted for these same Zernikes. These results provide sufficient justification for the use of surface mounted actuators to correct for these higher order aberrations. A structural model of the reflector system is now developed to characterize the ability of various actuators to correct for these Zernike aberrations.

Chapter 4

Structural Analysis

With the optical analysis of the segmented reflector system completed, a structural analysis is now required. This analysis consists of several tasks. First, a finite element model of the reflector panels is developed based on existing models of composite reflector panels. Second, the piezoelectric actuators used as surface controllers are modeled and their mechanical properties are characterized. Lastly, an actuation scheme is implemented, in which the panel deformations due to actuator strain are quantified using Zernike polynomials. From this, a "transfer function" relating surface deformation to actuation strain is generated. This transfer function acts as the link to the optical model in controlling surface aberrations.

4.1 Reflector Panel Structural Model

The structural model of a hexagonal reflector panel was constructed using the MSC/NASTRAN finite element modeling program. The model was based on an existing model developed by C.P. Kuo at the Jet Propulsion Laboratory for analysis of composite panels used in the Precision Segmented Reflector (PSR) program. This existing model was used primarily to predict low order aberration correction through symmetric energization of surface mounted piezo actuators. Model accuracy has been empirically validated through cryointerferometric methods and direct loading of an actual panel.[27,28] Therefore, to improve accuracy, the model developed for this analysis is nearly identical in material properties to its predecessor. Significant differences are found only in physical dimensions and fidelity, both of which were increased to meet the need to resolve higher order surface aberrations on a larger panel.

In constructing the panel model, two major assumptions were made. First, no backup support structure was designated. Rather than design a specific structure and constrain the motion of the panels, a virtual constraint was imposed at the centerpoint of the panel's rear

---

[27]Kuo, C.P. 1991, pp. 1-5.

[28]Kuo, C.P., Wada, B.K. "Composite Deformable Mirror", JPL New Technology Report Case No. NPO-18128, 1990, pp. 5-9.

face. This constraint eliminated translation of the panel, but did not create any reaction forces. From this it is noted that there can be no piston motion of the panel for correction. Second, across the diameter of a face, there are 21 collinear gridpoints. This offers the structural model higher fidelity than the COMP model in describing surface errors. This will prove to be an important issue when estimating the modeling error due to the finite truncation of Zernike polynomials.

The hexagonal panel model measures 1.30 meters flat-to-flat, with a maximum diameter of 1.51 meters. It is a spherical conic, with radius of curvature of 7.80 meters. Although the optical reflector model utilizes parabolic panels, a spherical model was generated to take advantage of the symmetry of curvature about the panel center, thereby simplifying deformation analysis. Within NASTRAN, the panel is defined by 3 layers of equilaterally spaced gridpoints, each layer containing 331 gridpoints (Figure 4-1). These layers form the skeleton for 2400 elements, divided into a core and two facesheets. Each facesheet is comprised of 600 isoparametric triangular plate elements with a thickness of 1.0 mm. The facesheets are composites, consisting of two layers with different properties. The outer layer is 0.9 mm monolithic graphite-epoxy (Gr/Ep). The inner layer, in contact with the core, is 0.1 mm of isotropic adhesive. This adhesive layer, included to model shear lag, has a much lower elastic modulus than the Gr/Ep.

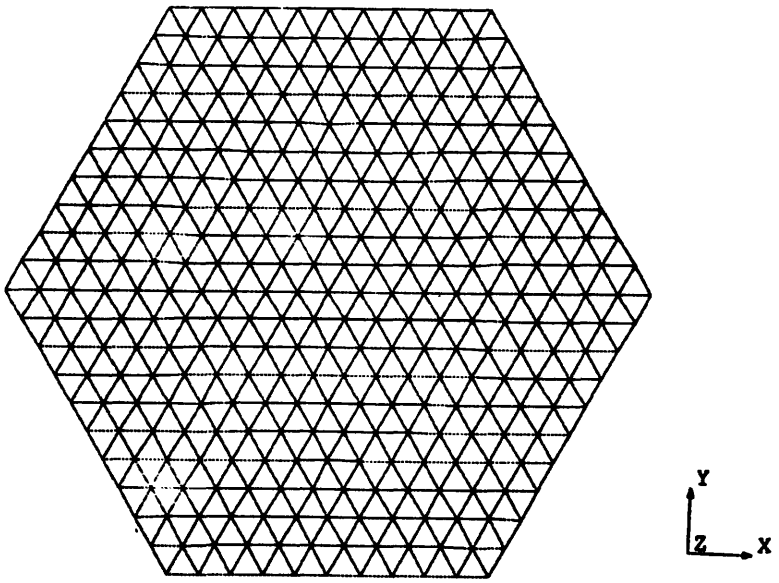

Figure 4-1
NASTRAN Panel Model Geometry

The core consists of 2 identical layers of solid body elements, each layer containing 600 elements. These pentahedral elements simulate a continuous aluminum honeycomb core with a thickness of 2.54 cm. To simplify modeling, the anisotropic properties of the hexagonal honeycomb structure are evenly smeared through the solid elements. This simplification has been shown to be quite accurate for in-plane strains, both in experiments involving the PSR panels and elsewhere.[29] It is contingent, however, on using two or more layers of solid elements to model the core, as a monolithic core model would prove too stiff in shearing.[30] Figure 4-2 illustrates an exploded cross-section of a panel.

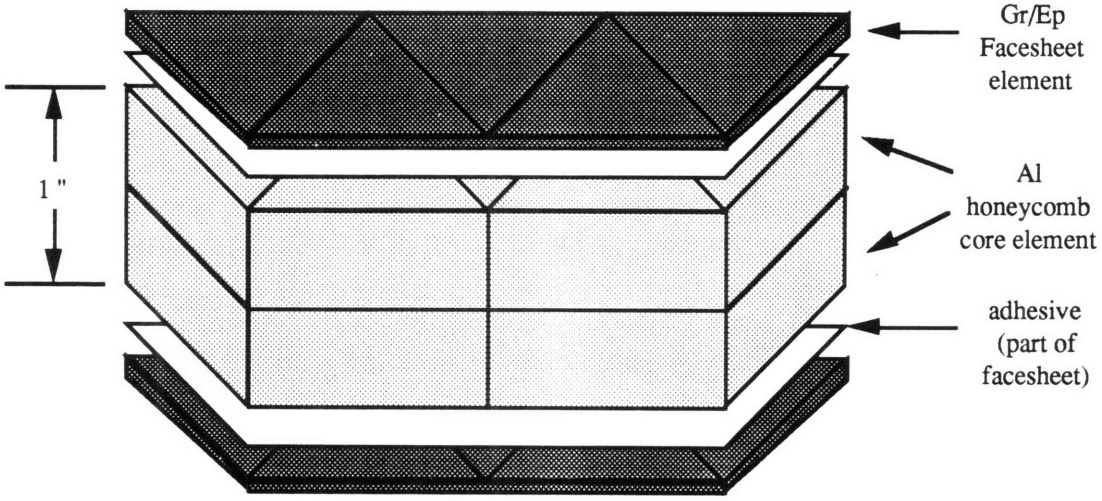

Figure 4-2
Exploded Panel Cross-Section

[29]C.C. Chamis, R.A. Aiello and P.L.N. Murthy. "Fiber Composite Sandwich Thermostructural Behavior: Computational Simulation", *Journal of Composites Technology and Research* No. 10, 1988, pp. 93-99.

[30]Conversations w/ C.P. Kuo (JPL section 354), November, 1991.

Table 4-1 lists pertinent material properties of the core and facesheets.

Table 4-1 NASTRAN Panel Element Properties

Core	
element type: CPENTA	E11: 2.55×10^5 Pa
no. of elements: 600 each layer	E22: 1.54×10^5 Pa
total thickness: 2.54 cm	E33: 8.60×10^8 Pa
density: 33.6 kg/m^3	E44: undefined
CTE: 22.5×10^{-6}/K	E55: 6.9×10^7 Pa
core mass: 1.249 kg	E66: 1.24×10^8 Pa
Gr/Ep Facesheet	
element type: CTRIA (composite)	E11: 15.93×10^{10} Pa
no. of elements: 600 each face	E22: 15.93×10^{10} Pa
thickness: 0.9 mm	E12: 1.746×10^{10} Pa
density: 1544 kg/m^3	facesheet mass: 2.034 kg each
CTE: 2.5×10^{-6}/K	
Adhesive	
thickness: 0.1 mm	E: 0.31×10^{10} Pa
density: 1108 kg/m^3	adhesive mass: 0.162 kg each layer
CTE: 102×10^{-6}/K	
Overall panel mass: 5.64 kg	
All material properties referenced to operating T = 100K	
E11 modulus aligned with x-axis in all materials	

The surface mounted piezoelectric actuators are now modeled and integrated into the panel model before the actuation scheme is developed.

4.2 Actuator Model

As stated earlier with regard to the panel model, the surface actuators are modeled after those used in the PSR model. Each actuator is composed of two rod elements. Each element is 7.5 cm long and 1.27 cm wide, with a thickness of 0.1 cm. The actuator elements are surface mounted to the rear face of the panel model, each element spanning two adjacent gridpoints. The attachment between panel and actuators is modeled as perfect,

with no shear losses. On each panel is affixed 66 actuators, or equivalently, 132 elements. Figure 4-3 illustrates the actuator layout on each reflector panel. The actuator properties and behavior are now described.

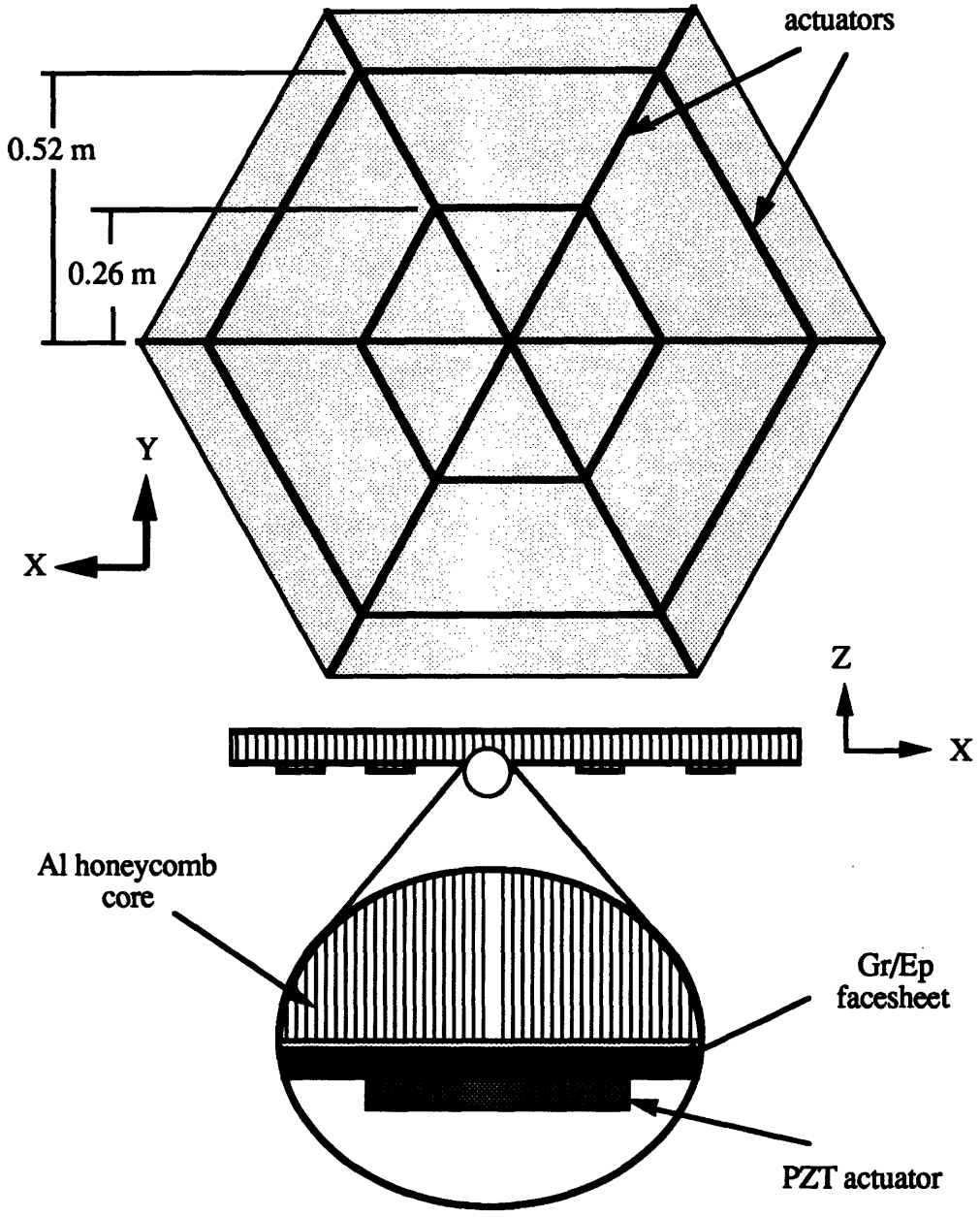

Figure 4-3
Panel/Actuator Configuration

4.2.1 *Nominal Piezoelectric Behavior*

The actuator element properties simulate the behavior of piezoelectric ceramics. Piezoelectric ceramics (piezos) are electromechanical in nature, straining in the presence of an electric field. The strain-field relationship is nominally linear, and is modeled as:

$$\frac{\Delta t}{t} = \varepsilon_3 = d_{33}E_3 \tag{4.1}$$

where E_{33} (V/m) is the applied electric field in the x_3 direction, t is the nominal actuator thickness, and ε_3 is the associated induced strain in the x_3 direction. Similarly, the applied field causes an in-plane strain due to Poisson effects, described by:

$$\frac{\Delta d}{d} = \varepsilon_1 = d_{31}E_3 \tag{4.2}$$

where d is the unenergized actuator length. When the applied field is in the direction of polarization within the piezo, it is considered positive, inducing a positive strain in the x_3 direction. The coefficient d_{33} is therefore taken to be positive. The coefficient d_{31}, related to the Poisson effect, is negative.[31] Therefore, a positive field applied to a piezo increases its thickness while reducing its length. By reversing the field, the opposite occurs. Because an actuator is surface mounted to the panel facesheet normal to the direction of the applied field, the in-plane strain plays the greatest role in deforming the panel. When the actuator strains in-plane, the induced mechanical stress produces an effective moment about the midline of the panel cross section. This moment causes localized bending in the rear panel surface (Fig. 4-4).

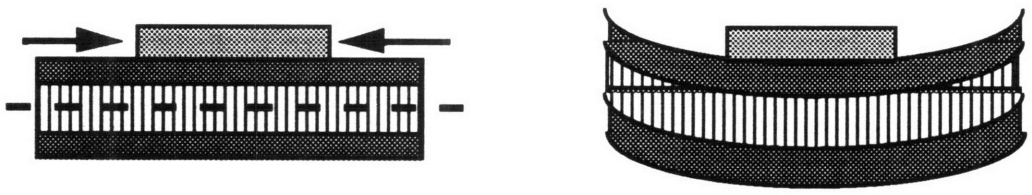

Figure 4-4 Localized Bending Due to Actuation Strain

---

[31] Anderson, Eric H. *Piezoceramic Actuation of One and Two Dimensional Structures*, MIT Master's thesis SSL #5-89, 1989, pp. 22-24.

NASTRAN cannot directly model electromechanical behavior; therefore, the in-plane actuation strain is modeled as an equivalent thermal strain, while the normal strain is unmodeled. The in-plane strain ε_1 can be restated as:

$$\varepsilon_1 = d_{31}E_3 = \alpha_1\Delta T \tag{4.3}$$

where α_1 is an equivalent coefficient of thermal expansion (CTE) representing d_{31} of the piezo, and ΔT is a temperature gradient representing the field strength. It appears from Eq. 4.3 that an unlimited strain can be induced from an actuator with sufficient voltage. In reality, however, non-idealities in piezoelectric behavior place restrictions on the operation range of the actuators.

4.2.2 Non-Ideal Piezo Behavior

Three main non-ideal phenomena arise in the modeling of piezo actuators. First, the strain-field relationship is not actually linear. As shown experimentally by Anderson, the in-plane strain coefficient d_{31} increases with increasing field strength.[32] This nonlinearity makes it difficult to predict surface deformations as functions of input voltage. Therefore, to formulate a roughly linear strain-field model, the maximum strain must be kept low enough to minimize the deviation in d_{31}. At a strain of 50 $\mu\varepsilon$, d_{31} has increased by almost 25%. However, when physically constrained, the total piezo "thermal" strain is partially absorbed into mechanical stress, thereby reducing the net strain. For this lower net strain, the nonlinearity is less apparent. Second, the equivalent piezo CTE is based on material properties at a temperature of 100 Kelvin. Manufacturer's specifications for the piezoelectric material modeled here, Vernitron PZT-5H, show a considerable decrease in d_{31} at lower temperatures (Fig. 4-5).[33,34] The lower d_{31} of 0.1 $\mu\varepsilon$/V at 100 K requires a voltage upwards of $\pm$500 V for an actuation strain of 50 $\mu\varepsilon$. Such a high voltage increases the risk of arcing across the actuator, and should not be exceeded.

---

[32]Anderson, et al.

[33]Information package, Vernitron Corp. Piezoelectric Division, 1991, pp. 2-12.

[34]Chen, G.S. "Piezoelectric Actuator for Cryogenic Application", JPL Interoffice Memorandum 3542/GSC/018-90, January 18, 1990, pp. 3-4.

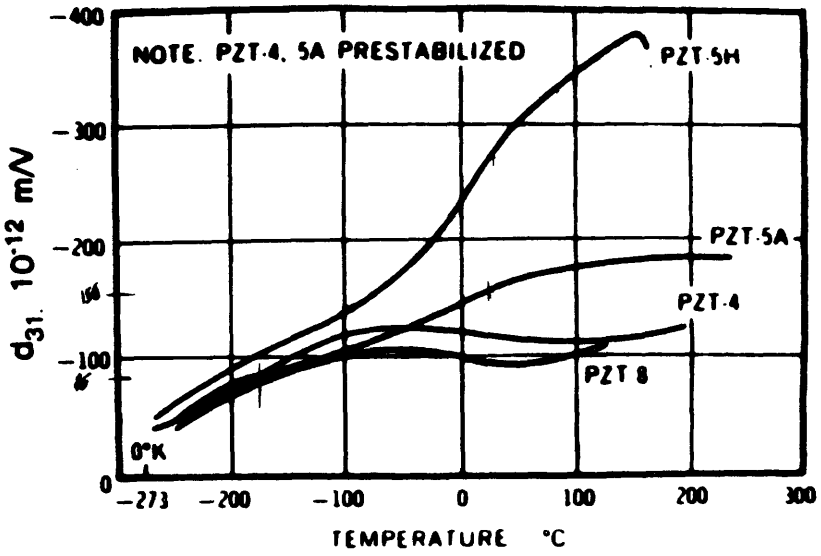

Figure 4-5

d_{31} vs. Temperature

Third, piezos exhibit considerable hysteresis when strained cyclically at low frequencies. Anderson has shown that the hysteresis, defined as the maximum strain offset divided by the total strain range, is more than 16% when the piezo is cycled at ±250 με. For smaller strain ranges (±50 με), the hysteresis is approximately 13%.[35] This is still a considerable deviation from the ideally linear behavior described by Eq. 4.2. Empirical results indicate that methods such as charge control, in which the nonlinear dielectric constant of the piezo, related to d_{31}, is linearized through a connection with a fixed capacitance, lessen the hysteretical strain offset by a factor of three.[36] For a strain range of ±50 με, this amounts to 4.5%, which may be considered small enough to disregard in this model. Also, for constrained actuators, the net strain is still less, and the hysteresis would be even lower. In consideration of the nonlinearities of piezoelectric materials, the allowable range of energization of the actuator models operating at 100 K is ±500 V, corresponding to an unconstrained strain of ±50 με. In this way, the nonlinearities of d_{31} and hysteresis are minimized, and the risk of arcing across the actuators is lessened. With the characterization of the actuators completed, it is now necessary to describe the actuation scheme and the effects of actuation strain on the reflector panel. Table 4-2 lists the pertinent properties of the piezoelectric actuators used in the model.

---

[35]Anderson, E., 1989, pp. 30-40.

[36]Anderson, E.H., Moore, D., Fanson, J.L., Ealey, M. "Development of an Active Member Using Piezoelectric and Electrostrictive Actuation for Control of Precision Structures", JPL report (section 354), 1990, pp. 10-11.

Table 4-2 Actuator Model Element Properties

Element Type	NASTRAN CROD
no. of elements / actuator	2
no. of actuators / panel	66
actuator dimensions (cm)	15.0 x 1.27 x 0.1
Material type	Vernitron PZT-5H
Modulus (E)	1.53×10^{11} Pa
d_{31} (@ 100 K)	0.1 με/V
Effective CTE (με/K)	0.1
Density (kg/m^3)	7500.
Mass / actuator	0.0143 kg
Total actuator mass / panel	0.943 kg

4.3 Actuation Scheme

The actuation scheme involves (1) the layout of actuators in a panel and (2) the determination of the effect of any single actuator on the panel in terms of an expansion in 36 Zernike polynomials. A few assumptions are made in analyzing the scheme. First, the deformations generated are small enough to be considered linear with induced strain. Second, the effects of one actuator are independent of those of every other actuator, i.e, linear superposition is assumed when several actuators are used simultaneously. Third, each panel is an independent structure; i.e, the actuators of one panel cannot affect the deformations of another panel. Lastly, modal decomposition rather than zonal decomposition of the deformations is used. Zonal decomposition is the generation of influence functions very similar to contour lines describing zones of equal deformation.[37] Modal decomposition involves fitting the deformation to a series of orthogonal surfaces, namely Zernike polynomials. In general, modal decomposition is not the preferred method, as most of the higher spatial frequency components of a deformation are lost in the finite series of terms. Two important factors, however, drove the selection of modal decomposition. First, modal decomposition is less costly computationally. Second, surface deformations within the COMP optical model are already described in Zernikes.

---

[37]Ealey, M., Wellman, J., "Fundamentals of Deformable Mirror Design and Analysis", Litton/Itek Optical Systems report #1167-05, 1990, pp. 2-4.

Using the same Zernikes within the structural model lends itself to a ready interface between structural and optical models when actively controlling deformations.

The scheme begins with the actuator layout. Shown in Figure 4-6, the layout of 66 actuators consists of two concentric rings and six radial arms. Each arm contains five actuators. The inner ring is formed from 12 actuators, and the remaining 24 actuators make up the outer ring. The layout was designed arbitrarily, with no fixed number of actuators initially chosen. As stated previously, Kuo has shown that actuators laid out in equally spaced radial arms are effective in controlling low order curvature errors. In addition, the rings seem to be an appropriate configuration to influence azimuthally periodic deformations, based on intuitive arguments. The combination of rings and radial arms of actuators would intuitively appear effective in controlling deformations defined by Zernike polynomials.

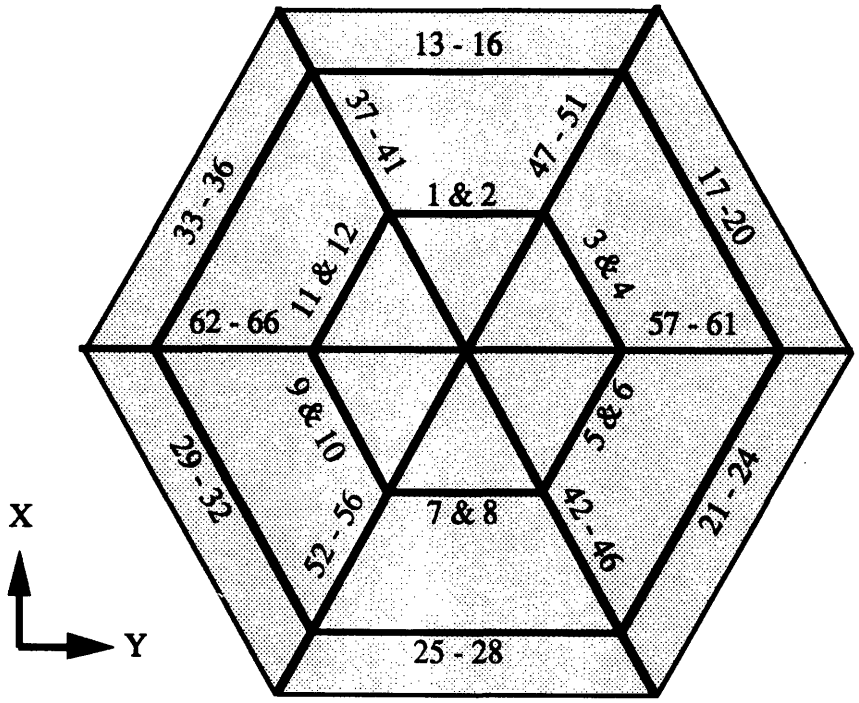

Figure 4-6
Actuator Layout and Numbering Sequence

Within NASTRAN, each actuator, composed of two rod elements, is individually energized one at a time with an equivalent thermal strain of 50 $\mu\varepsilon$. Positive strain is defined as the contraction of an actuator's in-plane dimensions. Output data include stresses within the actuators and nodal displacements for all gridpoints. Both are discussed below.

4.3.1 *Stress/Strain Analysis*

Internal stress is created because the actuator is mechanically constrained by the facesheet. The net strain of each actuator can be calculated simply from:

$$\varepsilon_{net} = \varepsilon_{total} - \varepsilon_m = \varepsilon_{total} - \frac{\sigma_m}{E} \tag{4.4}$$

where σ_m is the resultant internal stress, and ε_{total} is the original thermal strain of 50 $\mu\varepsilon$. Several trends are apparent in the strain behavior of the constrained actuators. First, there is a great deal of symmetry in the strains. Typically, actuators which are symmetrically positioned with respect to either the x or y midlines of the panel exhibited the same strain behavior. Therefore, the actuators can be divided into 19 groups, listed in Table 4-3.

Table 4-3 Symmetric Strain Actuator Groups

Group	Actuator #	Strain ($\mu\varepsilon$)	Group	Actuator #	Strain ($\mu\varepsilon$)
1	1,2,7,8	6.6	10	37,46,47,56	29.1
2	3,6,9,12	21.3	11	38,45,48,55	23.0
3	4,5,10,11	22.9	12	39,44,49,54	22.5
4	13,16,25,28	6.8	13	40,43,50,53	21.2
5	14,15,26,27	6.8	14	41,42,51,52	20.2
6	17,24,29,36	23.2	15	57,66	7.75
7	18,23,30,35	24.3	16	58,65	6.86
8	19,22,31,34	24.3	17	59,64	6.57
9	20,21,32,33	24.4	18	60,63	6.57
			19	61,62	6.60

Second, groups 1, 4, 5, and 15 through 19 strained much less than the remaining actuators. This is due to their alignment parallel to the panel x-axis. The composite facesheet is orthotropic, and its elastic modulus is highest in the x-direction, thereby providing greater resistance to stretching. Third, net actuator strain increases with increasing distance from the panel center. For example, actuators 4 and 20 are positioned in the same angular orientation with respect to the x-axis. At full energization, however, actuator 20 strains 6.5% more. Simply stated, the outer actuators stretch more because

there is less panel to push out of the way. The deformations resulting from the net actuator strains are now discussed.

4.3.2 Deformation Analysis

In each actuation case, deformation data for each gridpoint was collected. READZ, a NASTRAN subroutine, was used to fit the displacement data to the first 36 Zernike polynomials. An additional Matlab routine was written to calculate the rms surface error of each actuator induced deformation. The READZ algorithm essentially is a Graham-Schmidt orthogonalization with respect to Zernikes. The algorithm fits the Zernikes only to displacements in the z-direction. Stretching in the x and y directions are assumed small, and are ignored. Also, deformations of spatial frequency above the seventh order cannot be described by the first 36 Zernikes, and are discarded. As in the previous section, actuators within the defined groups exhibit very similar deformation behavior. Table 4-4 lists the maximum z-direction displacement and the rms surface error for each actuator group.

Table 4-4 Actuation Displacement and rms Surface Error

Group	Maximum Disp. (μm)	rms SE (μm)	Group	Maximum Disp. (μm)	rms SE (μm)
1	0.428	0.139	11	3.05	0.449
2	1.34	0.418	12	3.36	0.627
3	4.13	1.39	13	2.68	0.612
4	0.336	0.079	14	17.9	8.02
5	0.330	0.081	15	0.587	0.143
6	1.46	0.379	16	0.677	0.316
7	1.34	0.438	17	2.36	1.12
8	1.22	0.368	18	4.72	2.25
9	1.49	0.479	19	6.99	3.28
10	1.81	0.181			

The Zernike representation of panel deformations in combination with Table 4-4 provide interesting insights into the actuator performance. Figure 4-7 plots the distribution of Zernike coefficients within the deformations generated by group 2 actuators. Figure 4-8

illustrates the actual deformed surface. Appendix A.5 contains remaining distributions & mesh plots. From both figures it is clear that group 2 actuators (#'s 3, 6, 9, 12 in Fig. 4-6) have a strong influence primarily over Zernikes #4 and #6, corresponding to y and x axis astigmatism, with a secondary influence over Zernikes #5 and #7.

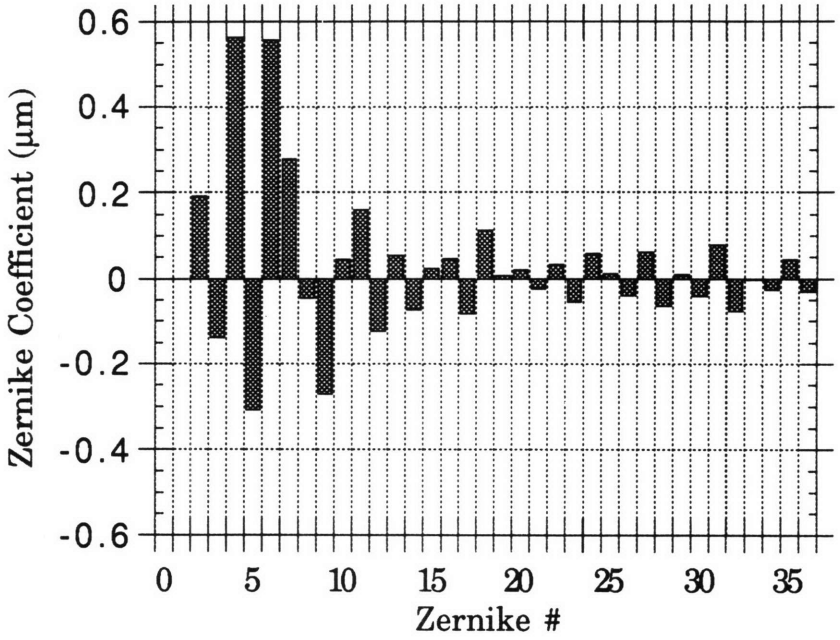

Figure 4-7
Zernike Influence Distribution over Group 2 Deformations

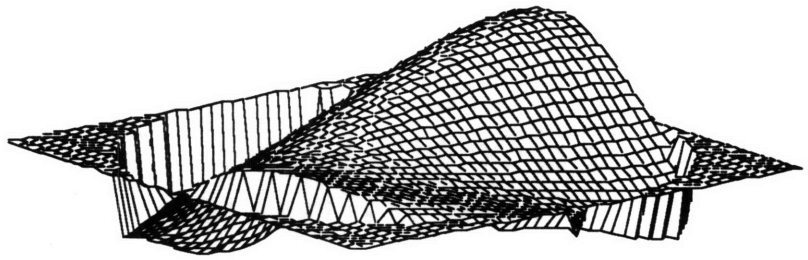

Figure 4-8
Actuator Group 2 Panel Deformation at 500 V

Most other actuator groups also showed a primary influence over astigmatism, with secondary influences over the remaining first 11 Zernikes. Little change in the higher

Zernikes was noted. In nearly all of these cases, the rms surface error ranged from 0.1 μm to 0.6 μm at full actuation. Notable exceptions occur in groups 15 through 19. In each case, the actuators, lying within the strip along the panel x-axis, affected mostly Z3, a rotation about the x-axis, with little effect on any other Zernike. In cases 17 through 19, the effect was large, producing an rms surface error greater than 1.0 μm. Table 4-5 lists Zernikes most affected by each actuator group.

Table 4-5 Zernikes Most Affected by Actuator Groups (in order of influence)

Group	Zernike #	Group	Zernike #
1	3,2,6,9	11	6,4,10,9
2	4,6,5,7	12	6,2,4,5
3	2,3,6,4	13	4,6,3,5
4	6,7,4,10	14	2,3,6,4
5	6,7,15,16	15	3
6	4,3,10,15	16	3
7	4,2,7,11	17	3
8	4,7,11,6	18	3
9	2,4,10,6	19	3
10	6,7,11,2		

From the above data, the transfer function relating panel deformation to actuator energization can be assembled. Assuming that the Zernike distribution within a deformation remains constant, and the Zernike magnitudes increase linearly with input voltage to the actuator for small voltages, each term in the transfer function matrix, designated A_{ij}, is formed by the finite difference:

$$A_{ij} = \frac{\partial Z_i(V_j)}{\partial V_j} = \frac{Z_i(V_j) - Z_i(0)}{V_j - V_0} = \frac{\text{value of Zernike i at 500V}}{\text{500 V in actuator j}} \qquad (4.5)$$

For each panel, **A** is a 36-by-66 matrix. Row 1 is a zero row, as Z1 representing piston has been removed. For the entire reflector, **A** is a 216-by-396 block diagonal matrix. It is apparent that there are more columns in **A**, representing the actuators, than there are rows, representing the Zernike "degrees of freedom" being controlled. Therefore, there are dependent columns, and the problem is overconstrained. Many actuators are redundant,

and will prove unnecessary in reducing surface error. This situation was not noticed in the initial layout of actuators, but still serves as a useful starting point in the control algorithm. Its purpose, as well as that of other actuator layouts, are discussed in the following chapter.

4.4 Conclusion

Chapter 4 has focused on the development and characterization of structural model of a composite reflector panel under loading by surface mounted piezoelectric actuators. The structural model of the hexagonal panel was created within NASTRAN, based on an empirically verified model used in the PSR program. The piezoelectric (PZT) actuators were integrated into the panel model as rod elements, and their electromechanical strain behavior was modeled as an equivalent thermal strain assuming linear strain behavior over a limited actuation range. Each panel model was mounted with 66 PZT actuators aligned in a configuration to simulate the radial and azimuthal behavior of Zernike polynomials. Individual actuators were energized, and the resulting deformations were characterized using 36 Zernike polynomials. From this, a control "transfer function" was developed. This transfer function related actuation energization to panel deformation defined in terms of Zernikes, thereby providing a link to the Zernike based optical model for the active correction of surface aberrations. The characterization of the deformations showed that (1) a great deal of symmetry exists among actuators in terms of net strain and resulting panel deformations, and (2) the piezo actuators induce primarily lower order ($\leq$ Z11) Zernike deformations. Few actuators showed any strong influence over higher order Zernikes, a fact that will play an important role in the control scheme developed in chapter 5.

Chapter 5

Control Scheme

Previous chapters have focused on the development and performance characterization of optical and structural models of the segmented reflector. These models are now integrated into an active control scheme for the correction of panel surface aberrations. This integration involves several steps. First, the main assumptions made in developing the control scheme are briefly discussed. Second, two test aberrations based on thermal gradient models for composite reflector panels are developed, and their effects on both structural and optical models of the reflector are quantified. These aberrations serve as worst case scenarios, providing justification for the use of active control on the panels. Third, two control algorithms, both based on a constrained least squares minimization, are developed. One is modified with an emphasis on surface error minimization, while the other is modified for wavefront error minimization. Fourth, three control cases, each using a different number and configuration of actuators for the correction of the test aberrations, are presented. Performance results are then presented in chapter 6.

5.1 Assumptions

In developing the control scheme for the correction of panel surface aberrations, three basic principles were followed. The first is the assumption that for small perturbations, the performance output of both the structural and optical models are linear. This applies to the panel deformations caused by the actuators as well as the wavefront error of the reflector. Therefore, twice the voltage into those actuators producing the deformation doubles the magnitude of the deformation. This linearity also applies when summing the deformations produced by several actuators. Similarly, doubling the magnitude of the deformation doubles the wavefront error. This linear behavior in both structural and optical models allows for a relatively simple solution to a system of linear equations.

Second, the mode of interface between the two models is the consistent definition of the first 36 Zernike polynomials to describe surface deformations. Because the series of Zernikes used is finite, all deformations are observed and corrected in the system only as linear sums of these Zernikes. Any deformations which are of spatially higher frequencies that those described by the defined Zernikes are unobservable and therefore uncorrectable.

Third, the observations, or "feedback", produced by the COMP optical model are global in nature. Essentially, this means that the control scheme used for the minimization of wavefront error is not concerned with the fact that a particular panel may suffer from coma, astigmatism, etc. Rather, the emphasis is on the aggregate effect of all panels on the wavefront error. As discussed in section 3.3, a panel's position in the reflector as well as the nature of its deformation play a role in its contribution to the wavefront error. Therefore, wavefront error control may allow significant aberrations to remain in one panel while eliminating those of another panel which have a greater impact on the overall wavefront error. The effects of the test aberrations on the performance parameters are now evaluated.

5.2 Test Aberrations

To test the control scheme's ability to correct significant error in the reflector panels, two test aberrations were developed. The first, based on a thermal model of the SMILS reflector, represents a "realistic" error which could be encountered by such a reflector during operation. The second aberration is contrived with the intention of testing the controllers' ability to reduce higher order aberrations. These aberrations are described, and their effects on the reflector panels' physical and optical properties are quantified. Performance parameters of interest are now defined.

5.2.1 Definition of Performance Parameters

Several performance parameters were measured for each test aberration and control case, and are defined follows:

- Residual error norm (N_e) - the Euclidean norm of the residual error vector $\vec{e}$ after correction, each vector component representing the coefficient of a Zernike polynomial. The residual error norm has units of microns. This is basically the magnitude of the remaining error after correction.
- rms SE (μm) - rms surface error over all six reflector panels after correction. This is determined by first multiplying the residual error vector $\vec{e}$ by the matrix **D**, representing the transformation of Zernike coefficients to point displacements. The rms SE is then calculated from these displacements.

• Strehl ratio (SR) - the ratio between peak intensity values of an aberrated point spread function and the nominal point spread function, and ranges from zero to one. Strehl ratio is measured from the point spread function generated by SAO Image (Fig. 3-1). A perfectly corrected system has a SR = 1.

• Eigenvalue (Λ) - the effective eigenvalue of the residual error vector $\vec{e}$ when decomposed into a linear sum of the S-matrix eigenvectors (Eq. 3.10). This is a measure of the error's ability to degrade the Strehl ratio. A larger eigenvalue error degrades the Strehl ratio more than a smaller eigenvalue error given that both errors were scaled to the same Euclidean norm.

• rms WFE (μm) - the rms wavefront error over the entire reflector system of six panels, as calculated within COMP. This also is a measure related to the degradation of the Strehl ratio. For small errors, the Strehl ratio falls off quadratically with WFE (Eq. 3.18).

• Actuator norm (N_a) - defined as the rms actuator energization value for a test case solution, scaled to a percentage of the maximum actuation of 500 V, multiplied by the number of actuators used. A dimensionless number, N_a is a crude measure of the amount of effort required to perform the correction.

These performance parameters form the core of the information gathered on both the test aberrations and the residual errors after correction.

5.2.2 Thermal Aberration

The first aberration, developed to approximate on-orbit conditions, is based on a thermal gradient model of the reflector panels. Two assumptions were made in modeling the gradient. First, all deformations within the system are due to thermal loading only. Aberrations caused by surface roughness and gravity loading were not considered. Second, the reflector alignment and curvature was assumed to be perfect once the system has been passively cooled to operating temperatures. This assumption contradicts experimental results which have noted significant changes in panel curvature with changing temperature.[38]

The gradient data for NASTRAN was taken from a thermal model developed for the SMILS telescope. Because the size and configuration of the SMILS reflector panels are nearly identical to those of the hypothetical reflector, a good representative thermal

---

[38]Hochberg, E., 1991, pp. 4-6.

aberration was thought possible. As mentioned in chapter 1, SMILS is a segmented infrared reflector designed for operation at ≈100 K under passive cooling, and an operating wavelength range of 80 μm to 700 μm. Near 100 K, the average spatial temperature gradient across the reflector aperture was estimated to be 2.4 K, with a through-the-thickness gradient of 0.07 K.[39] Therefore, a temperature profile ranging from 98.8 K to 101.2 K was imposed across the six reflector panels, with the mean operating temperature of 100 K placed along the reflector's centerline. The gradient across each panel was 0.8 K. Because the SMILS gradient model did not specify a distribution of temperature across the panel, the gradient is assumed to propagate in a linear fashion. Since the prescribed thickness gradient was very low, the temperature was modeled as constant through the thickness below any point on the surface. Figure 5-2 illustrates the gradient across each panel and its orientation to the panels' material reference axes. The arrow indicates the direction along which the gradient travels on each panel.

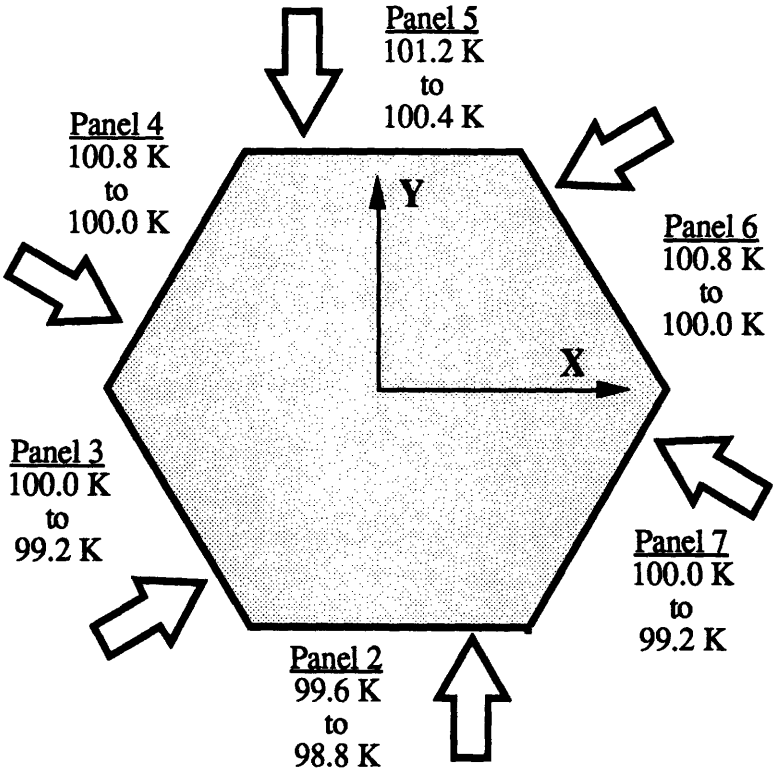

Figure 5-1
Thermal Gradient Across Reflector Panels

---

[39]Tsuyuki, G., French, L. "On-Orbit Thermal Performance of a Submillimeter Telescope Primary Reflector Panel", Jet Propulsion Laboratory, 1991, pp. 7-9.

The thermal gradient was applied to the panel model from each of six orientations, and the deformation output was fit to Zernike polynomials using the NASTRAN subroutine, READZ. Figure 5-2 illustrates the physical effects of the planar gradient on panels 2 and 5. The deformation is symmetric about both the panels' x and y axes. The symmetry is due to the gradient's alignment with the orthotropic facesheet's material reference axis. Figure 5-3 displays a Zernike distribution composed almost entirely of Z6 and Z5, x-axis astigmatism and defocus, amounting to a rms surface error of 1.25 μm for each of panels 2 and 5, with a maximum point deflection of 4.46 μm.

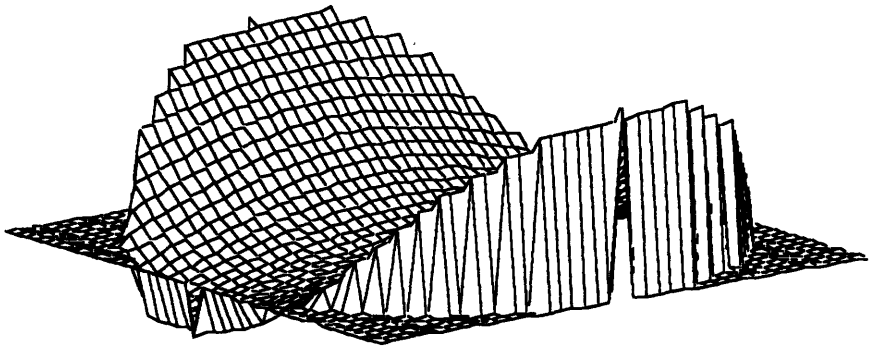

Figure 5-2
Thermal Gradient Surface Deformation in Panel 2

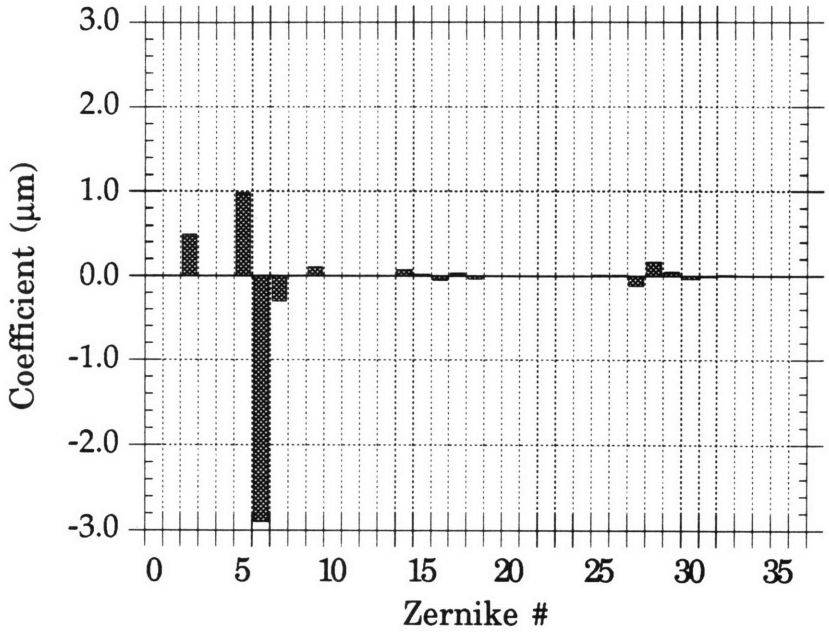

Figure 5-3

Zernike Distribution of Thermal Deformation in Panel 2

The deformations of panels 3, 4, 6 and 7, shown in Figure 5-4, are not as symmetric as those of panels 2 and 5. The 60 degree rotation of the panels' material reference axes with respect to the planar gradient produces a deformation, when described by Zernikes, consisting primarily of Z6 and Z3, x-axis astigmatism and y-axis tilt, with some Z5 (defocus) present.

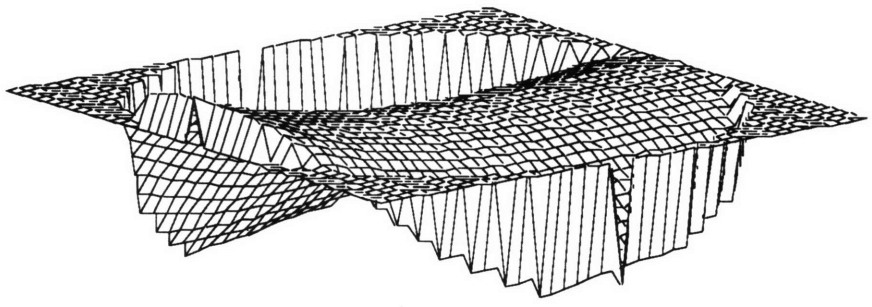

Figure 5-4

Thermal Gradient Surface Deformation in Panel 3

The predominance of Z6 is apparent in the Zernike distribution of Figure 5-5. The net surface deformation is less than that found in panels 2 and 5, equivalent to an rms surface error of 0.68 μm, with a maximum point deflection of 2.26 μm The rms surface error over the entire reflector is 0.91 μm.

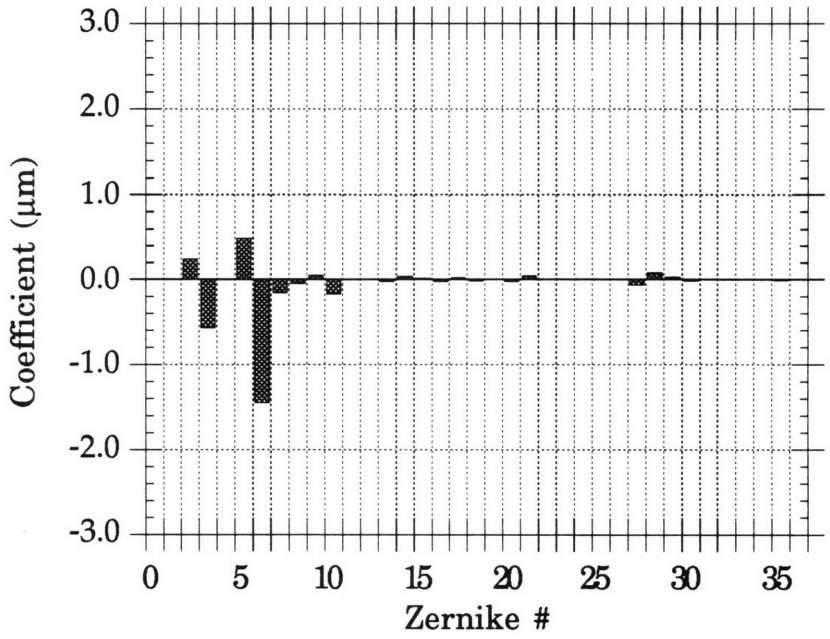

Figure 5-5

Zernike Distribution of Thermal Deformation in Panel 3

Figure 5-6 provides a rough contour plot of the entire reflector under thermal deformation. The light areas represent deformation in the positive z-direction (out of page), whereas dark regions represent receding deformations. As in Figure 5-1, the high end of the gradient begins at panel 5, and continues across the reflector in a planar fashion through panel 2. The two halves of the reflector on either side of the midline exhibit identical yet inverted deformations. This phenomenon is a result of the assumption of a uniform gradient. Therefore, panels experiencing temperature ranges above 100 K exhibit an equal but opposite deformation to those experiencing temperature ranges below 100 K.

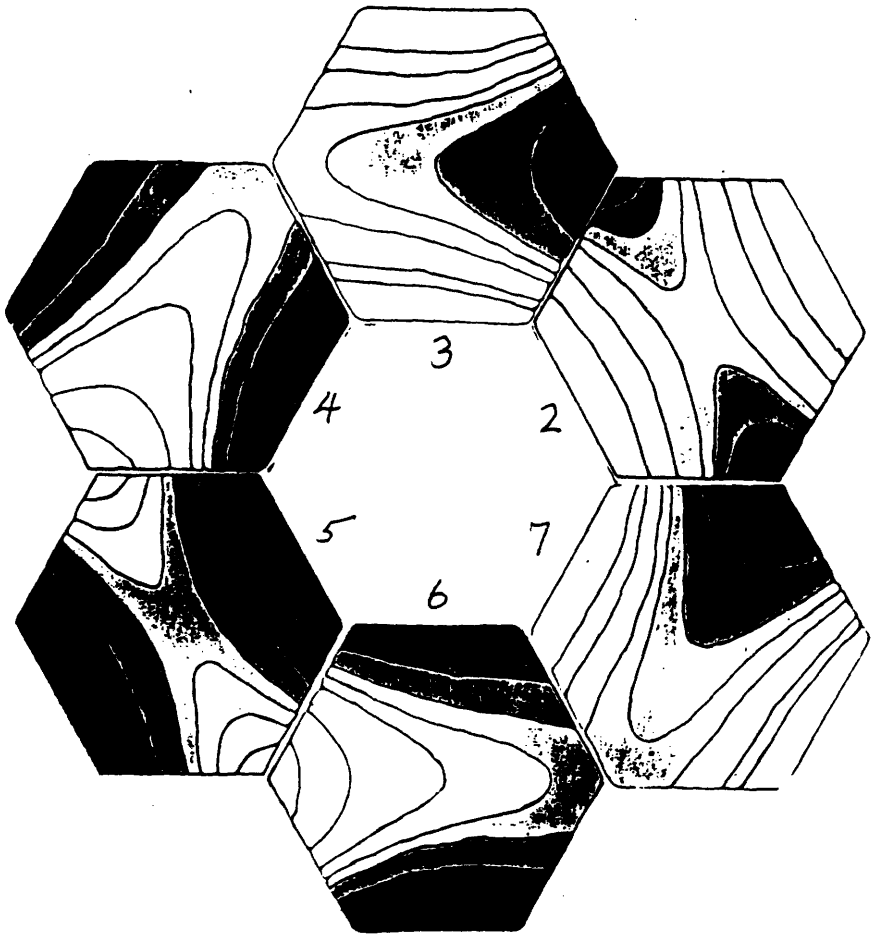

Figure 5-6
Thermal Aberration Contour Plot

The effects of the thermal aberration on the optical performance of the reflector are now considered. A least squares fit of the thermal aberration defined by Zernikes to the S-matrix produced an effective eigenvalue of 0.0911, with an error norm of 5.54 μm. The rms wavefront is 1.67 μm (λ/6). This is well beyond the λ/14 limit for the use of the linear analytic model for prediction of the Strehl ratio. Therefore, the Strehl ratio was measured directly from the PSF image of the aberrated system (Fig. 5-7) as 0.368.

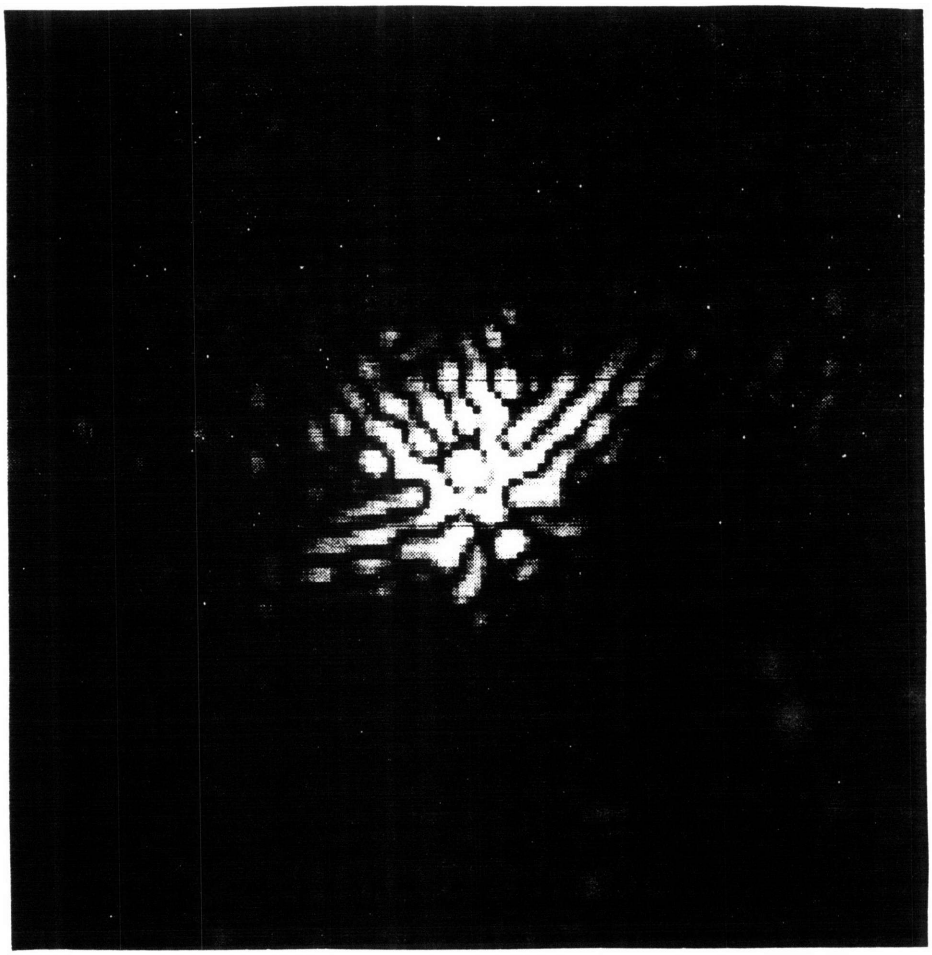

Figure 5-7
Point Spread Function Under Thermal Aberration (Sao Image)

The one dimensional intensity distribution, also taken from the PSF of Figure 5-7, shows a considerable scattering of light in to four distinct lobes (Fig. 5-8), centered at 1.5", 3.0", 4.5" and 7.0" from the image center. Correspondingly, there is a significant decrease in the scattered intensity between lobes. The effect is a selective obliteration of secondary images falling within the lobes, and a noted increase in resolution for those objects located within the intensity "wells".

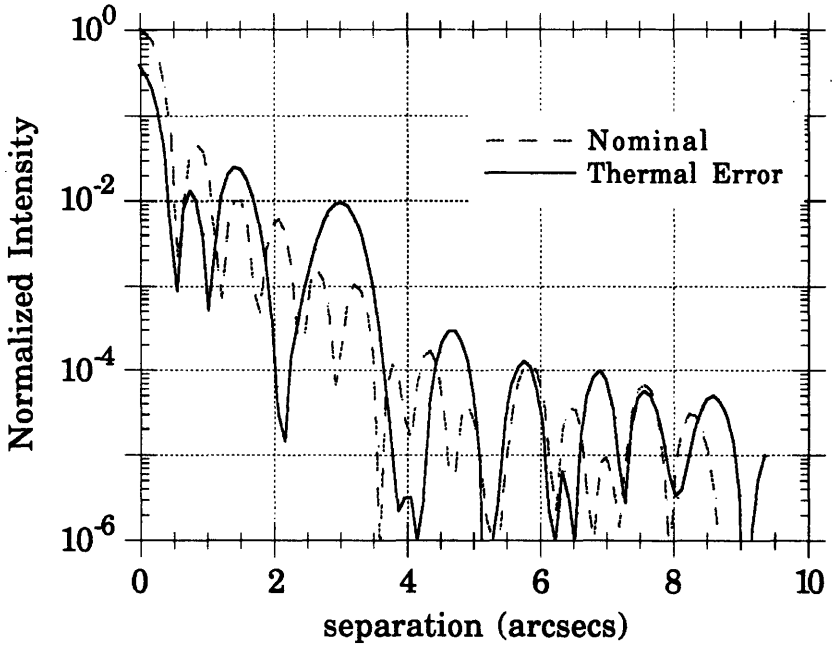

Figure 5-8

One-Dimensional Intensity Distributions - Nominal vs. Thermal

Appendix A.6 further illustrates this phenomenon with additional data derived from intensity distributions of various star/dwarf pairs. From these data, it is apparent that such a phenomenon may improve the chances for detection of properly positioned objects. Table 5-1 summarizes the effects of the thermal aberration on the reflector performance parameters.

Table 5-1 Effects of Thermal Aberration on Reflector Performance

Operating Wavelength	Eigenvalue	Residual Error Norm	Strehl Ratio	rms Surface Error	rms Wavefront Error
10.0 μm	0.0911	5.54 μm	0.368	0.9119 μm	1.67 μm

In conclusion, a linear thermal gradient of 2.4 K produced fairly symmetric panel deformations dominated by Z5 and Z6, defocus and astigmatism, resulting in a wavefront error of 1.67 μm. Although the Strehl ratio was degraded to 0.368, the intensity distribution indicates that the resolution of dim secondary objects may be improved at certain angular bandwidths. The effects of the combined aberration are now discussed.

5.2.3 Combined Aberration

After analysis of the thermal aberration, an additional aberration was developed to evaluate the effects of some higher order Zernikes not predominant in the thermal error. This aberration, named the combined aberration, is a combination of the thermal aberration and an eigenvector of the optical S-matrix. This eigenvector, associated with one of the larger eigenvalues of the S-matrix, consists primarily of Z10 (primary trifoil), Z13 and Z25 (third and fifth order spherical aberrations). Combined with the thermal aberration, the resultant aberration produced a surface as illustrated in Figure 5-9. Figure 5-10 shows the associated Zernike distribution. Panels 2 and 5 were deformed to an rms surface error of 1.756 μm, with the remaining panels deformed to a lower rms value of 1.36 μm. The overall surface error is 1.51 μm.

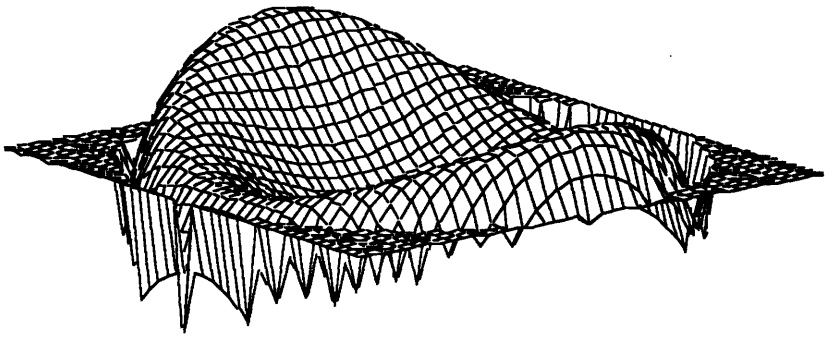

Figure 5-9
Combined Error Surface Deformation in Panel 2

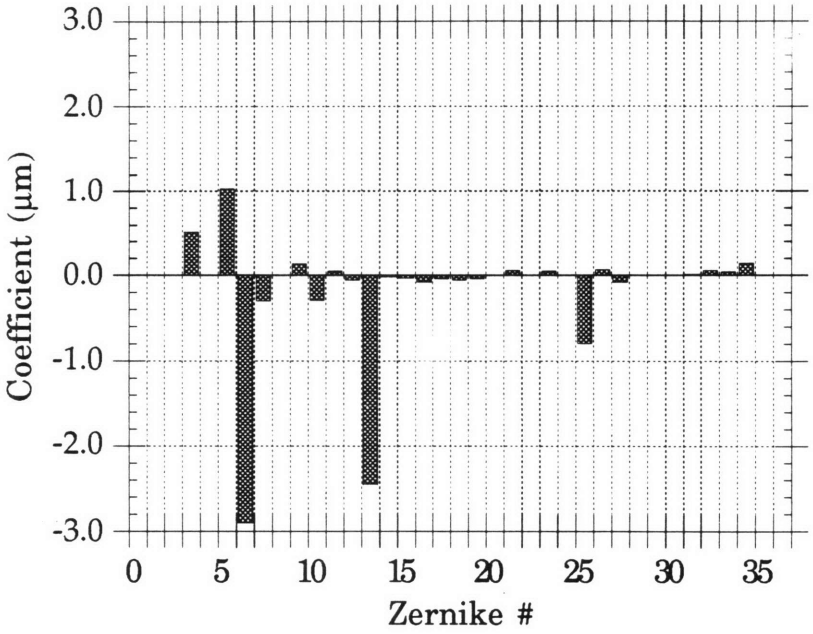

Figure 5-10

Zernike Distribution for Combined Aberration - Panel 2

In terms of optical performance parameters, the associated eigenvalue is 0.087. The error norm, scaled to produce an rms wavefront error of 2.50 μm (λ/4), is 8.572 μm. The Strehl ratio falls to 0.086 (Fig. 5-11).

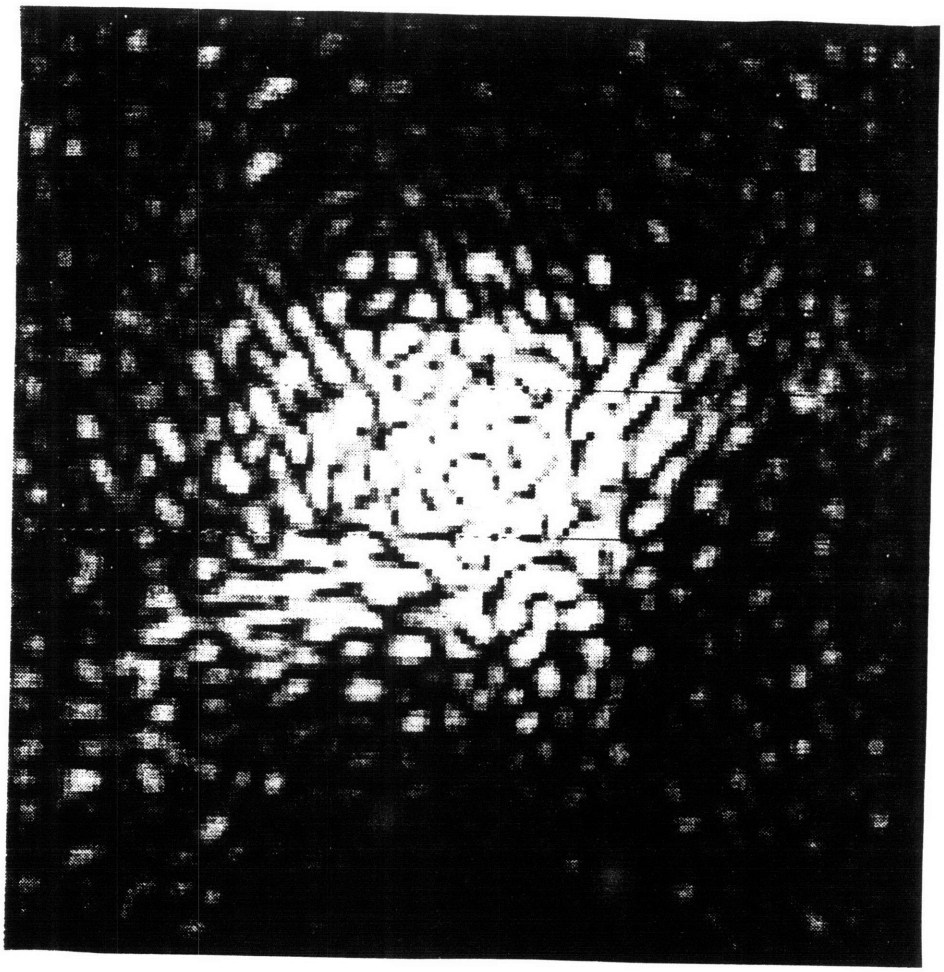

Figure 5-11
Point Spread Function Under Combined Aberration (Sao Image)

The one dimensional intensity distribution, shown in Figure 5-12, clearly illustrates the severe degradation of the nominal diffraction pattern. Energy from the central peak has been scattered across nearly the entire field of view, effectively obliterating all but the brightest secondary objects which may lie within.

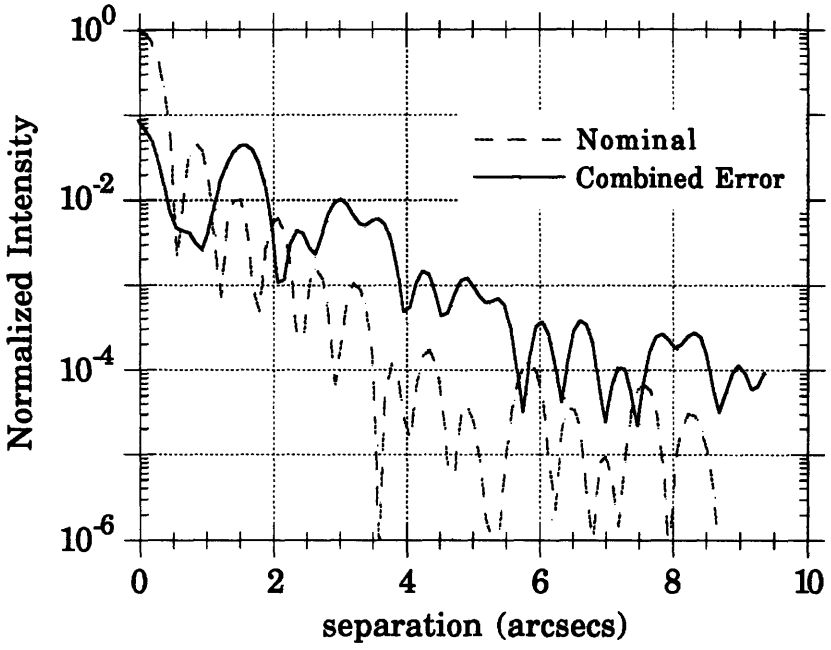

Figure 5-12

One Dimensional Intensity Distributions - Nominal vs. Combined

Due to this extensive scattering, no comparison between nominal and aberrated object-background ratios was made. Table 5-2 summarizes the effects of the combined aberration on the reflector system.

Table 5-2 Effects of Combined Aberration on Reflector Performance

Operating Wavelength	Eigenvalue	Residual Error Norm	Strehl Ratio	rms Surface Error	rms Wavefront Error
10.0 μm	0.087	8.572 μm	0.086	1.505 μm	2.50 μm

In conclusion, the combined aberration worsened the effects of the thermal aberration by introducing higher order Zernike terms at larger amplitudes. The increased wavefront error of 2.5 μm degraded the intensity distribution to the point where no dim secondary objects could be detected. In both test aberrations, it was shown that deformations in the form of Zernikes beyond those representing rigid panel motions produce considerable degradation in image quality. This provides sufficient justification to seek ways to actively correct for

these higher order aberrations. The control algorithm developed to perform this correction is now explained.

5.3 Control Algorithm

The control algorithm is fundamentally a weighted least squares fit for linear systems. In general, the weighted least squares fit can be represented as:

$$\min ||\vec{e}||^2 = \min_{\mathbf{x}} \mathbf{G}||\mathbf{Ax}-\mathbf{b}||^2 \tag{5.1}$$

where, in this analysis, **A** is an m-by-n control matrix, x is the actuation vector in n-dimensional space, b is an m-dimensional input error, and **G** is a symmetric weighting matrix. Eq. 5.1 can be expanded into a quadratic cost function **L**:

$$\min_{\mathbf{x}} \mathbf{L} = \min_{\mathbf{x}} \langle\langle \mathbf{GAx}-\mathbf{Gb}), (\mathbf{Ax}-\mathbf{b}) \rangle\rangle$$

$$= \min_{\mathbf{x}} \left\{ \frac{1}{2}(\mathbf{Ax})^T\mathbf{G}(\mathbf{Ax}) - (\mathbf{Ax})^T\mathbf{Gb} \right\}$$

$$= \min_{\mathbf{x}} \left\{ \frac{1}{2}\mathbf{x}^T\mathbf{A}^T\mathbf{GAx} - \mathbf{x}^T\mathbf{A}^T\mathbf{Gb} \right\} \tag{5.2}$$

The cost function **L** is constrained, however, by the simple inequality:

$$|x_i| \leq V_{max} \tag{5.3}$$

This constraint represents the upper and lower bounds for actuator energization, ±500 V in this case. The general cost function **L** is now modified for two specific purposes; first, the constrained control of surface deformations with respect to surface error, and second, with respect to wavefront error.

5.3.1 Minimization of Surface Error

The cost function described by Eq. 5.2 can be altered to minimize with respect to surface error by choosing an appropriate weighting matrix. This choice begins with the A-matrix. The control matrix **A** is described with respect to Zernike polynomials. The weighting matrix must correct for surface error; therefore, a new matrix, **D**, is required to transform

the Zernike surfaces into any number of point displacements. This transformation is simply the polynomials describing the Zernikes as shown in Appendix A.4. The number of transformed displacement points is 331 per panel, equal to the number of gridpoints which define the structural model front surface. Generating more displacement points would not improve the accuracy of the weighting matrix, as the Zernikes already are approximations of the true surface. Therefore, for each panel, **D** is a 331-by-36 matrix. Over the entire reflector, it is a 1986-by-216 block diagonal matrix (diagonal because the panels deform independently of each other). A new quadratic cost function can be derived by substituting the product **DA** for **A** in the first line of Eq. 5.2. The final result is:

$$\min_{x} \mathbf{L_D} = \min_{x} \left\{ \frac{1}{2} x^T A^T (D^T D) A x - x^T A^T (D^T D) b \right\} \qquad |x_i| \le V_{max} \qquad (5.4)$$

where $\mathbf{D^TD}$ is the square weighting matrix with respect to surface error.

5.3.2 Minimization of Wavefront Error

The modification of the quadratic cost function **L** to minimize with respect to wavefront error is simpler than that for surface error. The weighting matrix for wavefront correction has already been developed in chapter 3 under the guise of the S-matrix. **S**, the transfer function relating wavefront error to surface deformation, contains the necessary information for wavefront correction, and is defined using Zernike polynomials. Therefore, a ready interface between **A** and **S** exists, and no modification is needed. The resulting cost function is:

$$\min_{x} \mathbf{L_S} = \min_{x} \left\{ \frac{1}{2} x^T A^T S A x - x^T A^T S b \right\} \qquad |x_i| \le V_{max} \qquad (5.5)$$

This weighted cost function and that of Eq. 5.4 were minimized using NPSOL (Nonlinear Programming SOLver), a Matlab subroutine developed at the Stanford Systems Optimization Laboratory. Required input includes the cost function and its gradient with respect to **x**. A resource macro contains the cost function's operating parameters such as the control and weighting matrices, variable dimensions, and actuator constraints.[40] The optimization method used by NPSOL to minimize the quadratic cost function is not

---

[40]Wette, M. "NPSOL-in-Matlab Users' Guide", Jet Propulsion Laboratory technical report, 17 December 1991, pp. 3-7.

explicitly known. The most common solution methods for nonlinear functions with inequality constraints, however, are based on Lagrangian Multiplier theory.[41] The three control cases implemented through NPSOL for the correction of the test aberrations are now discussed.

5.4 Control Cases

Three control cases were developed for each control algorithm to evaluate the ability of the piezo actuators to correct for surface aberrations in the reflector panels. Each case involves a different number and configuration of actuators. The cases are referred to as overconstrained, determinate, and underconstrained. The design criteria for each are discussed, and the actuator configurations used in each case are described.

5.4.1 Overconstrained Case

The first test case evaluated is the overconstrained case. It is termed overconstrained because the number of actuators per panel, 66, exceeds the number of degrees of freedom defined on each panel, 35 (Z1 was not considered). In controlling the surface error, all actuators are available for energization up to ±500 V. Therefore, the control A-matrix, relating changes in the Zernike coefficients to actuator energization, has full rank of 210 plus 186 redundant actuators. Because it is full rank, the A-matrix should potentially support at least one combination of actuators capable of completely correcting the surface aberration. The objective of the overconstrained case was to verify this potential and also provide a stepping stone for the determinate control cases.

Each test aberration was introduced into the cost functions described in Eq. 5.4 and Eq. 5.5 as the column vector b. The surface and wavefront control cost functions L_D and L_S were minimized using the full rank A-matrix. In both functions, the error created by each aberration was completely eliminated. Surface error and wavefront error were both zeroed, returning the reflector to its nominal shape. The four solution sets of the cost functions, the vectors $\vec{x}$ describing the energization level of each active actuator, were recorded for use in the two remaining control cases. Table 5-3 highlights the results of these solution sets. Test cases 1 and 2 represent the cost function solutions for the correction of the combined

---

[41] Bertsekas, Prof. Dimitri. Nonlinear Programming (6.252) lecture notes, section 4.4 (1992), pp. 1-3.

aberration, and test cases 3 and 4 represent those for the correction of the thermal aberration.

Table 5-3 Overconstrained Case Solution Results

	Test 1	Test 2	Test 3	Test 4
Type of Correction	combined error surface control	combined error WFE control	thermal error surface control	thermal error WFE control
no. of actuators	396	396	396	396
max. actuation	471 V	448 V	56 V	60 V
|mean| actuation	137 V	132 V	14.1 V	14.7
In all cases, "perfect" correction achieved (i.e, rms SE = rms WFE = 0, Strehl ratio =1)				

The use of these overconstrained solution sets in the determinate and underconstrained control cases is now discussed.

5.4.2 "Determinate" Case

The "determinate" control case is considered the first step in a crude optimization for actuator placement. The optimization centers on choosing the number of actuators roughly equal to the number of degrees of freedom in the system. An arbitrary decision was made to select those actuators whose actuation value exceeded a given threshold when used in the overconstrained control test cases. Those actuators with actuation values below this threshold were "discarded". This threshold was chosen to be the mean absolute actuation values in tests 2 and 4, as defined in Table 5-3. These values for tests 2 and 4 are 132 V and 14.7 V, respectively. The former was chosen to select the actuators used in the two determinate tests involving the combined aberration, and the latter was used for the tests involving the thermal aberration. Table 5-4 lists the pertinent parameters for each of the four determinate tests. The listed actuator groups, as defined in Table 4-3, are those with the greatest number of active actuators.

Table 5-4 Determinate Test Case Parameters

	Test 5	Test 6	Test 7	Test 8
Type of Correction	combined error surface control	combined error WFE control	thermal error surface control	thermal error WFE control
actuation threshold	±132 V	±132 V	±14.7 V	±14.7 V
Panel 2 actuator groups	4, 5, 8, 13	5, 8, 10, 11	4, 5, 11, 14	4, 5, 11, 14
Panel 3 actuator groups	1, 5, 8, 10	1, 8, 10, 11	5, 9, 12, 14	5, 9, 12, 14
Total no. of actuators	168	171	180	180

Note that in each test the number of actuators was lower than the number of degrees of freedom requiring control, 210, thereby explaining the term "determinate". This was acceptable, however, in light of the fact that a number of actuators exactly equal to the number of degrees of freedom would have produced a totally corrected system. This would not provide a performance comparison of each control solution, as the results would be identical. Therefore, slightly underconstrained systems were desirable. The number of actuators and their positions on the panels varied between tests, however. As seen in Table 5-4, the numbers of actuators used in tests 5 and 6, both involving correction of the combined aberration, differs by 3. In addition, the layouts of each, shown in Figure 5-13, differ slightly in the choice of actuators used. For panel 2, shown here, test case 5 used 28 actuators lying primarily in the outer ring and the horizontal radial arm. Test case 6 used 30 actuators more evenly distributed over the panel. In both test cases, most of the actuators have their greatest influence Z4, Z6 and Z3 (astigmatism and tilt).

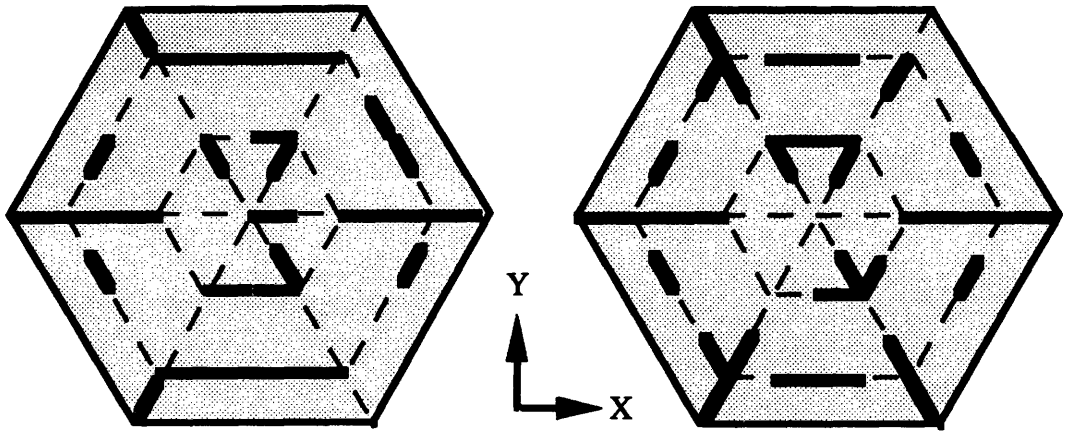

Figure 5-13
Comparison of Test Cases 5 and 6 - Actuator Layouts on Panel 2

The number and layout of actuators used in test cases 7 and 8 are identical to each other. Both use 180 actuators which are distributed in the patterns illustrated in Figure 5-14. On panel 2 there are 42 active actuators distributed mostly over the outer ring and two radial arms. Panel 3, mounted with 27 active actuators, shows a concentration of actuators on its right half, corresponding to the large positive deflection occurring at that edge of the panel.

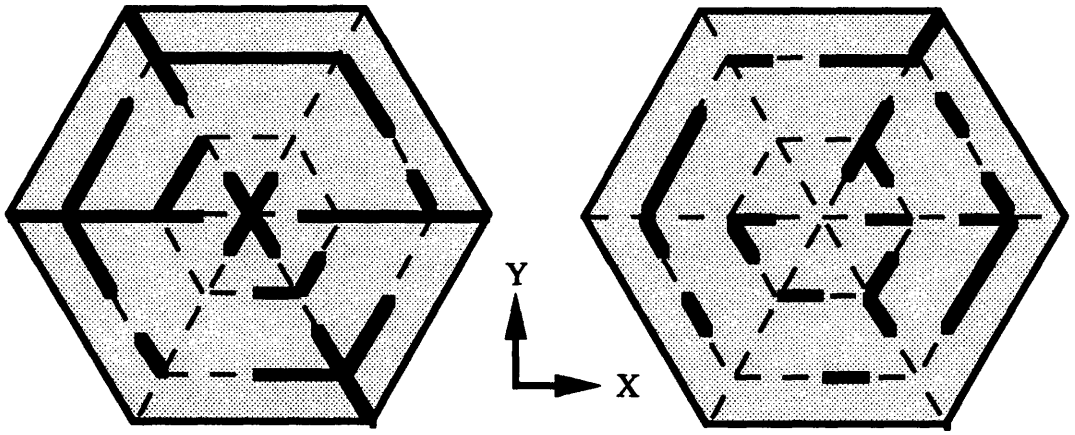

Figure 5-14
Test Cases 7 and 8 Actuator Layouts

The layout of each test case was integrated into its respective cost function by modifying the A-matrix. Because it is assumed that the deformations due to one actuator are independent of those of all other actuators, unwanted actuators are "removed" from the system by zeroing the columns of the A-matrix corresponding to those actuators. This left

the A-matrix with rank equivalent to the number of active actuators. Through the Matlab subroutine NPSOL, new cost function solutions were generated to correct the aberrations using the reduced A-matrix. For each solution, the residual error vector $\vec{e}$, defined in terms of Zernike degrees of freedom, was introduced into the COMP optical model, and performance parameters were measured. These are discussed in chapter 6. The final control case, underconstrained, is now discussed.

5.4.3 Underconstrained Case

The underconstrained control case takes the "optimization" scheme of the determinate case one step further. Its objective was to evaluate the ability of relatively few actuators to correct surface aberrations sufficiently to provide significant improvement in image quality. Whereas the determinate test cases used 170-180 actuators over six reflector panels, the underconstrained test cases utilized 50-70 actuators to achieve sufficient correction. "Sufficient" is defined as a level where the linear analytic form of the Strehl ratio accurately predicts the true Strehl ratio within 5%. From the optical analysis performed in chapter 3, this requires an improvement of Strehl ratio to 0.8 or greater.

As in the determinate case, a minimum actuation threshold was imposed on the results of test cases 1 through 4. For test cases 9 and 10, involving the combined aberration, the threshold is ±200 V. Actuators for test cases 11 and 12, involving the correction of the thermal aberration, were chosen using a threshold of ±250 V. Table 5-5 lists the operating parameters for the underconstrained test cases. The listed actuator groups represent those groups with the greatest number of active actuators.

Table 5-5 Underconstrained Test Case Parameters

	Test 9	Test 10	Test 11	Test 12
Type of Correction	combined error surface control	combined error WFE control	thermal error surface control	thermal error WFE control
actuation threshold	200 V	200 V	250 V	250 V
Panel 2 actuator groups	5, 8	8, 16	4, 8	4, 8
Panel 3 actuator groups	5, 8	8, 16	4, 8	4, 8
Total no. of actuators	69	51	60	60

The higher actuator threshold reduced the number of actuators available in test case 9 to 69. Twelve of these are present on panel 2, concentrated primarily in actuator group 5 (Fig. 5-15). Group 5 is the actuator group with the greatest influence over the higher order Zernikes present in the combined aberration as well over astigmatism, and therefore was selected to remain. Test case 10, minimizing wavefront error, showed a primary selection of actuators in group 8, controlling astigmatism. The number of active actuators on panel 2 was reduced to 8 in test case 10.

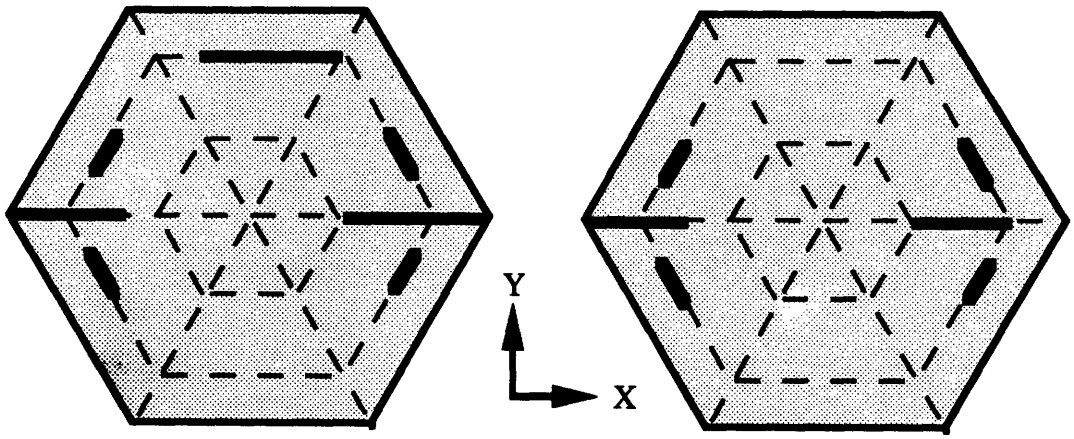

Figure 5-15
Comparison of Test Cases 9 and 10 - Actuator Layouts on Panel 2

As in test cases 7 and 8, the actuator layouts of test cases 11 and 12 are identical in number and configuration. Each uses a total of 60 actuators, 14 of which appear on panel 2. The

actuator pattern on this panel is very symmetric, with most of the actuators lying on the outer ring (Fig. 5-16). These actuators belong primarily to groups 4 and 8, known to be most influential over Z4 and Z6 (astigmatism). Only 7 actuators are present for the correction of panel 3, again concentrated along the right half of the panel. The lower number of actuators on panel 3 may be attributed to the smaller amplitude of the thermal aberration on this panel compared to that of panel 2.

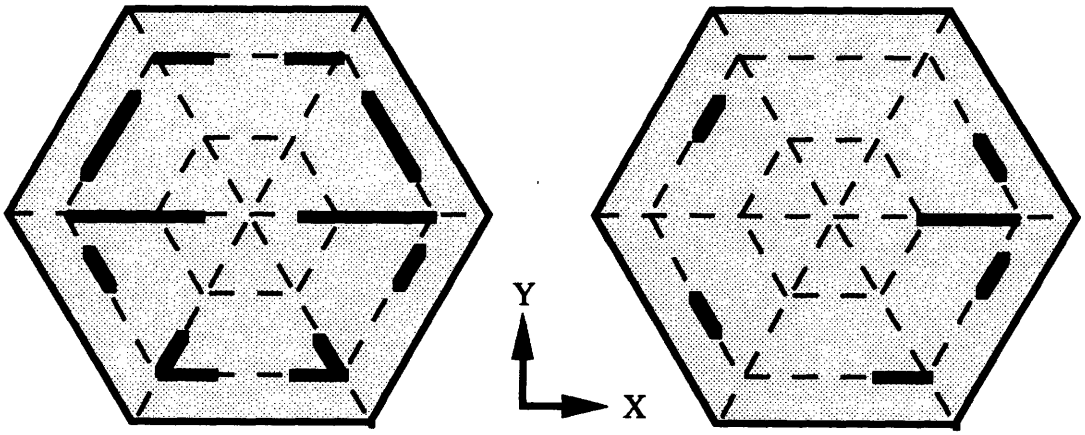

Figure 5-16
Test Cases 11 and 12 Actuator Layouts - Panels 2 and 3

As in the determinate test cases, the A-matrix for each underconstrained test case was generated by zeroing those columns of the original A-matrix corresponding to inactive actuators. While the A-matrix is still a 216-by-396 matrix, its rank is reduced to the number of remaining actuators. The new cost function solutions and resulting performance improvements are now discussed for both determinate and underconstrained test cases.

5.5 Conclusion

This chapter has focused on the development of a control scheme to evaluate the abilities of surface mounted piezoelectric actuators to minimize surface aberrations described by higher order Zernike polynomials. Two test aberrations based on a thermal gradient model of composite reflector panels were created through NASTRAN. These aberrations, consisting mainly of astigmatism (Z6) and third order spherical (Z13), were evaluated for their effects on the reflector's optical performance through COMP. The resulting degradation in image quality proved sufficient justification for the use of active control of these higher order aberrations. Two control algorithms, both based on a constrained least squares fit, were developed for the minimization of surface and wavefront errors. Three control cases were

then introduced, each representing a different number and configuration of actuators to be used in the control algorithms. The first, over constrained case utilized all 396 available actuators for correction, and completely eliminated the test aberrations in both control algorithms. The most active actuators of the overconstrained case were then selected for use in the last two control cases, determinate and underconstrained.

The determinate control case, the first crude optimization of actuator placement, retained between 168 and 180 actuators over the six panels for correction of the test aberrations. These actuators were concentrated primarily in the outer ring of the original panel layout, where the greatest influence over Z6 and higher Zernikes was found. The underconstrained control case used 51 to 69 actuators for correction of the test aberrations with respect to surface and wavefront error, respectively. Again, the majority of actuators were found in the outer ring of the layout. In both determinate and underconstrained control cases, the test cases involved in the correction of the thermal aberration used identical actuator layouts for the minimization of both surface error and wavefront error. This may be a result of the low energy, large scaled nature of the thermal aberration, effectively described using only Zernikes below Z6. The comparative correction results of the thermal aberration for wavefront and surface error minimization are the focus of chapter 6, which presents the results of the described test cases.

Chapter 6

Results

This chapter presents results for the test cases performed in both the determinate and underconstrained control cases (tests 5 through 12). Within each control case, results for the correction of combined and thermal aberrations are analyzed. For each aberration, correction performance parameters obtained by implementation of weighted cost functions for surface and wavefront error correction are discussed. In addition, Zernike coefficient distributions are presented for selected panels in each test case. For test case 11, the underconstrained correction of the thermal aberration to minimize surface error, intensity function distribution data is compared to that of the nominal and thermally aberrated reflector systems. This is used to evaluate the reflector's ability to resolve dim secondary objects after correction. The performance results of test cases 11 and 12 are then compared to determine the superiority of either control algorithm. Lastly, sources of modeling error are presented and their effects on the correction results quantified.

6.1 Determinate Control Case

This section presents the results from test cases 5 though 8: the correction of both the combined and thermal aberrations using determinate control cases.

6.1.1 Correction of Combined Aberration

The results of test cases 5 and 6 represent the performance values of the reflector system when the determinate control cases were implemented towards the elimination of the combined aberration. Both cases 5 and 6, correcting with a weighting towards surface and wavefront error respectively, showed an excellent reduction in error. Figures 6-1 and 6-2 illustrate the Zernike distribution of the residual error $\vec{e}$ on panel 2 for each case. Compared to the aberrated distributions in Figure 5-10, it is apparent that the Zernikes which comprise most of the combined aberration, Z5, Z6 and Z13, were reduced to magnitudes comparable to those of the remaining Zernikes.

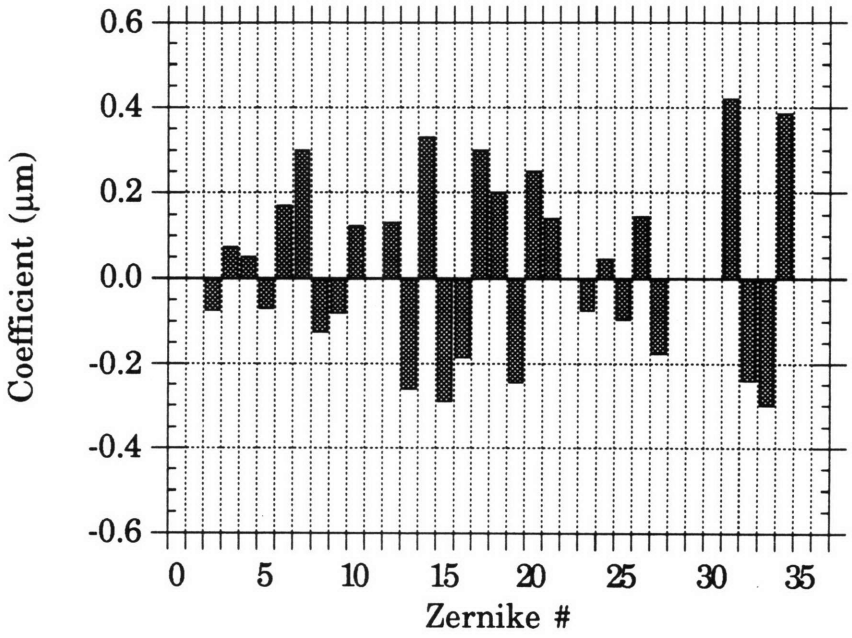

Figure 6-1

Zernike Distribution for Test Case 5 - Panel 2

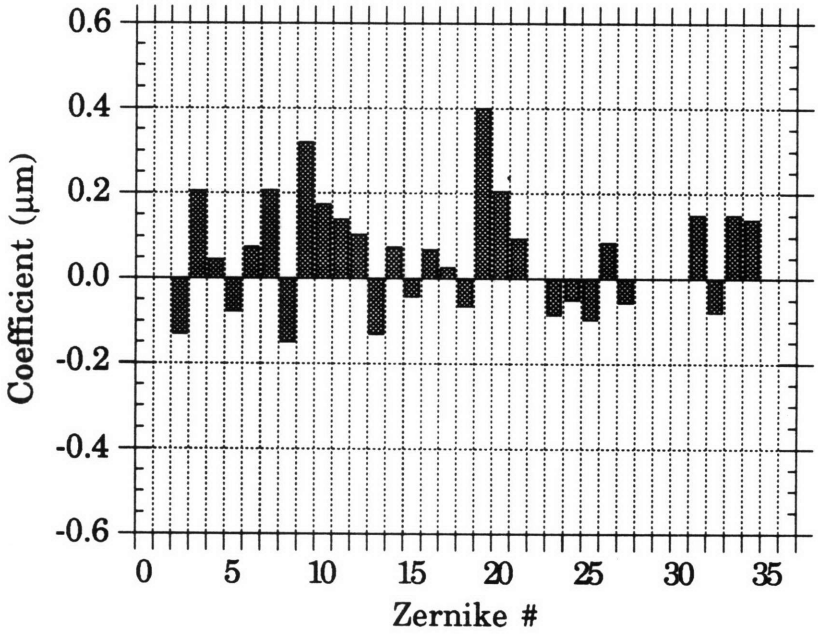

Figure 6-2

Zernike Distribution for Test Case 6 - Panel 2

In fact, many of the corrected Zernikes of test case 5 showed a slight increase in magnitudes, with the exception of Z5 and Z25, both of which were lowered considerably to avoid their relatively strong effects on surface error for a given input. The brunt of the residual error has been shifted to Z14 through Z20 and Z31 through Z34, all of which showed weaker effects on surface error (see Fig. 3-8). This correction results in a residual error norm N_e of 2.27 μm. The corrected Zernike coefficients of test case 6, while also slightly larger in magnitude than the original aberration Zernikes, showed an emphasis on Z9 and Z19, representing first and third order comas. These Zernike terms have relatively benign effects on wavefront error (see Fig. 3-7). This distribution produced a N_e equal to 2.56 μm, slightly higher than that of test case 5, as would be expected from a control algorithm not geared toward the correction of purely the error magnitude.

Translated into surface displacements, the residual aberrations of cases 5 and 6 produced total rms surface errors of 0.164 μm and 0.307 μm, respectively. It is clear from Figure 6-3 that test case 5 has done well in minimizing the panel surface deformations.

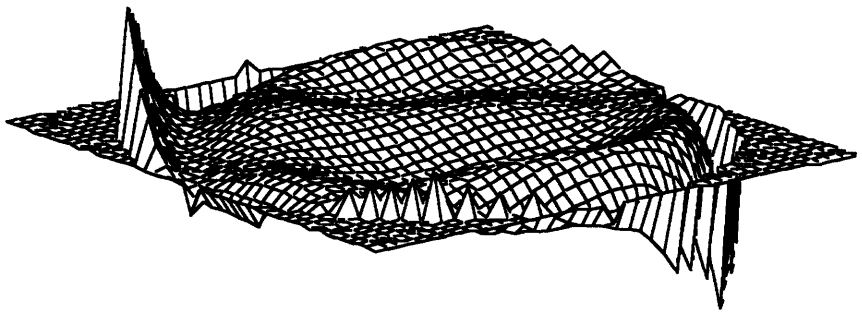

Figure 6-3
Residual Surface Error on Panel 2 - Test Case 5

Test case 6, correcting for wavefront error, does not attempt to eliminate the surface error completely, selectively reducing only those Zernikes most detrimental to wavefront quality. Therefore, large scale deformations are still evident in the residual error (Fig. 6-4). These figures may be somewhat misleading, however. The large deformations seen on the edges result from the projection of the residual aberrations onto unit circles rather than onto hexagons. In reality, such fringe effects do not exist.

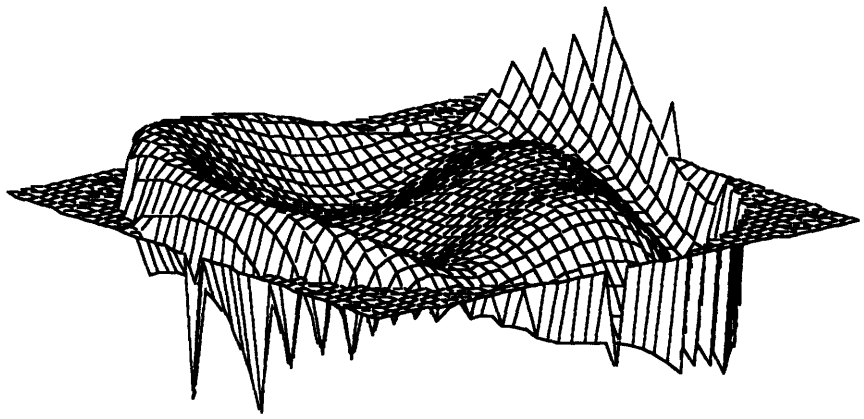

Figure 6-4
Residual Surface Error on Panel 2 - Test Case 6

Both test cases provided excellent improvement of optical performance parameters, as well. COMP analysis calculated a residual rms WFE of 0.39 μm (λ/25) for test case 5 and 0.27 μm (λ/37) for test case 6. As both of these values are well within the linear perturbation range as defined in chapter 3, the resulting Strehl ratios were determined analytically. The predicted Strehl ratios for test cases 5 and 6 were 0.937 and 0.969, respectively; a vast improvement over the aberrated Strehl ratio of 0.086. These predictions were matched to within 2% of the Strehl ratios calculated by COMP. The small discrepancy is due to the approximate nature of the numerical S-matrix generated for Zernike polynomials rather than to a weakness in the analytic model. The resulting point spread functions of both test cases were very close in quality to the nominal image shown in Figure 3-1, showing only a slight loss of sharpness near the center.

The actuator efforts required for both corrections were similar, also. The actuator norm N_a of test case 5, utilizing 168 actuators, amounted to a value of 113.1. Test case 6 exhibited a slightly higher N_a of 114.6 over 171 actuators. In both tests, this equated to an rms voltage of approximately 340 V for each actuator. This is a relatively high actuation level, required to minimize the higher energy Zernikes Z13 and Z25. More strain energy is associated with the higher order terms, and require greater effort to correct them. Table 6-1 summarizes the results for test cases 5 and 6 in comparison with those of the combined aberration.

Table 6-1 Determinate Correction Results of Combined Aberration

	Uncorrected Combined Aberration	Test Case 5 Results	Test Case 6 Results
Error norm (N_e)	8.57 μm	2.27 μm	2.56 μm
Act.norm (N_a)	N/A	113.1	114.6
Eigenvalue (Λ)	.087	.0305	.0113
rms WFE (μm)	2.49	.392	.272
rms SE (μm)	1.51	.164	.307
Strehl ratio	.086	.959	.972
# of actuators	N/A	168	171
operating wavelength = 10 μm			

In conclusion, both determinate control cases for the minimization of the combined aberration showed excellent correction, returning the image Strehl ratio to better than 95%, although the overall power consumption for each case was rather high. Correction results for the determinate control of the thermal aberration are now discussed.

6.1.2 Correction of Thermal Aberration

The determinate control cases for correction of the thermal aberration are represented by test cases 7 and 8. Both cases performed nearly perfect corrections of the panels' surfaces. Each case, using 180 actuators, reduced the residual error norm N_e to the order of 0.1 μm ($\lambda/100$). Most of the residual Zernike coefficient values were fairly constant around 0.01 μm (Fig. 6-5). This resulted in corrected surface and wavefront error values on the order of 0.01 μm ($\lambda/1000$). Strehl ratio was corrected to 1.0 within 3 significant figures, and the point spread function was returned to its nominal state.

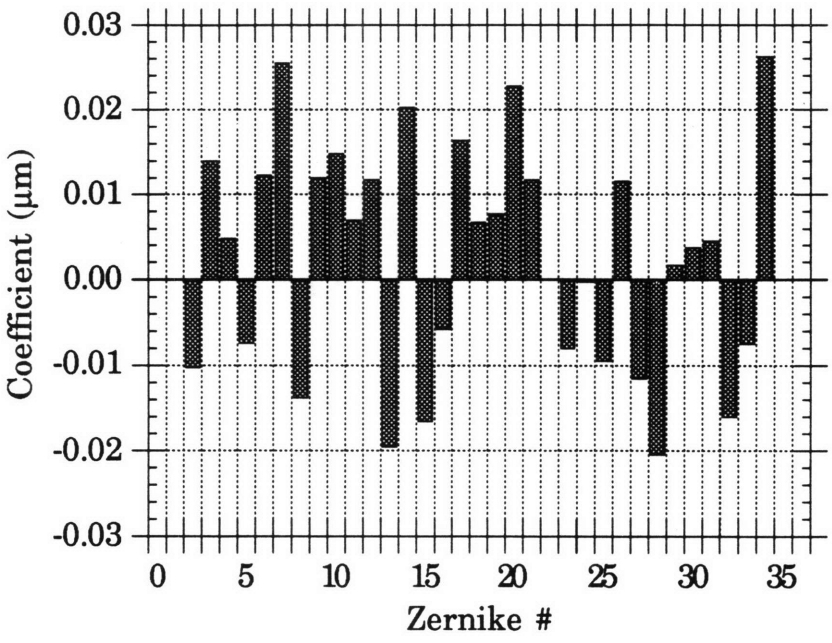

Figure 6-5

Zernike Distribution for Test Case 7 - Panel 2

In addition, the actuator norm N_a was only 13.0, equal to an rms actuation voltage of 36 V per actuator. This low value for N_a can be accounted for by the nature of the thermal aberration. From Table 5-4, it is seen that primarily actuator groups 4, 5 and 14 are used in test cases 7 and 8. These groups most strongly affect Zernikes Z2, Z6 and Z7, representing y axis tilt and astigmatism, and primary trifoil. The thermal aberration consists almost entirely of Zernikes #5 and #6. As stated previously, these are large scale, relatively low energy shapes. This fact, in addition to the large number of actuators available for correction of Z6 performed a thorough reduction of the aberration possible with relatively little effort. Table 6-2 lists the residual performance data for both test cases in comparison to the thermal aberration.

Table 6-2 Determinate Correction Results of Thermal Aberration

	Uncorrected Thermal Aberration	Test Case 7 Results	Test Case 8 Results
Error norm (N_e)	5.54 μm	.088 μm	.144 μm
Act.norm (N_a)	N/A	13.0	13.9
Eigenvalue (Λ)	.091	.0274	.0122
rms WFE (μm)	1.67	.016	.015
rms SE (μm)	0.91	.008	.011
Strehl ratio	.368	.999	.999
# of actuators	N/A	180	180
operating wavelength = 10 μm			

In conclusion, the determinate control case produced nearly perfect correction of both combined and thermal aberrations. All four test cases recovered the Strehl ratio to better than 95% using 168 to 180 actuators over the six panels. The correction of the combined aberration, test cases 5 and 6, required nearly an order of magnitude greater actuator effort than that of the thermal aberration in test case 7 and 8, however. This clearly illustrates the increased difficulty in eliminating higher order($\geq$ Z10) Zernike deformations from an aberration when using a limited number of actuators. The effects of this difficulty for an even smaller number of actuators are now considered.

6.2 Underconstrained Control Case

This section presents the results from test cases 9 though 12: the correction of both the combined and thermal aberrations using underconstrained control cases. These test cases provide a more "realistic" approximation to the level of correction attainable by a relative handful of actuators.

6.2.1 Correction of Combined Aberration

The results of test cases 9 and 10 represent the performance values of the reflector system when the underconstrained control cases were implemented towards the elimination of the combined aberration. Test cases 9 and 10, utilizing 69 and 51 actuators respectively, did not reduce the combined aberration sufficiently to achieve acceptable results. Figures 6-6

and 6-7 illustrate the residual Zernike distributions of the residual error $\vec{e}$ on panel 2 for each test case. In comparing these distributions to that of the combined aberration (Fig. 5-10), it is clear that the actuators used in these test cases have little influence over most of the higher order Zernikes (Z11 through Z36). The actuator groups used in both cases, groups 5, 8 and 16, affect primarily Z3, Z4 and Z6, each of which was attenuated. Z6 in particular has been attenuated from nearly 3.0 μm to less than 0.5 μm . Z13 and Z25 (third and fifth order spherical aberration) remained relatively unchanged, however, allowing most of the original aberration to remain.

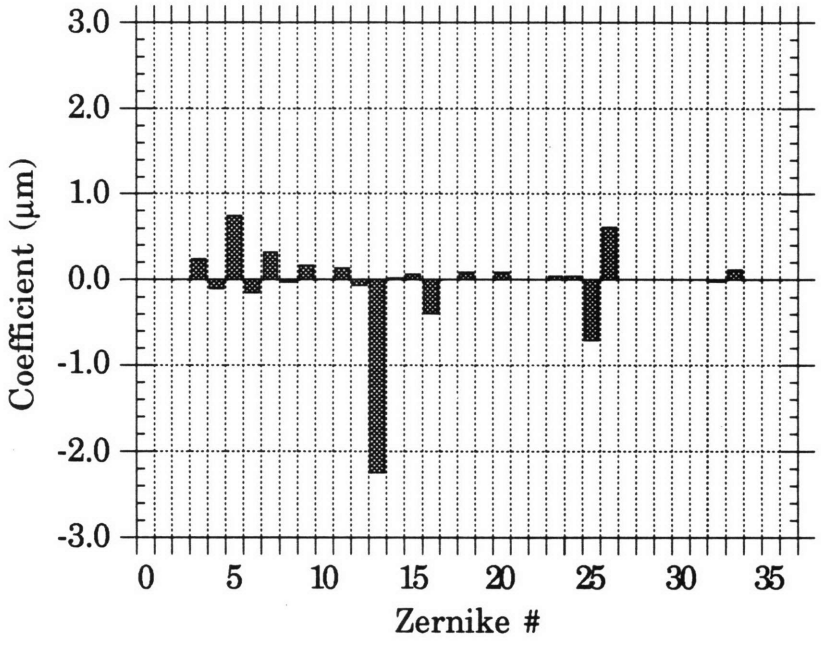

Figure 6-6
Zernike Distribution for Test Case 9 - Panel 2

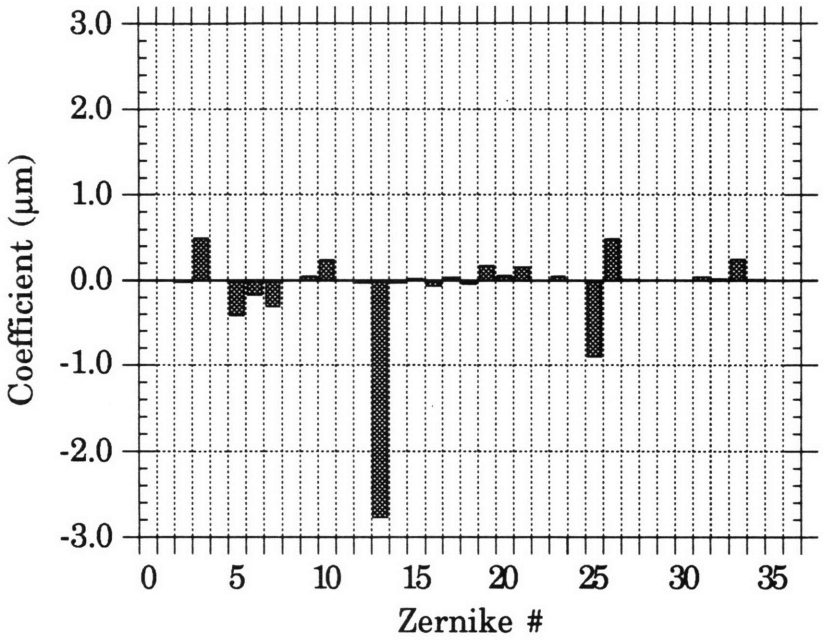

Figure 6-7

Zernike Distribution for Test Case 10 - Panel 2

The poor correction of Z13 and Z25 is apparent in the residual error $\vec{e}$. The residual error norm N_e for test case 9 is 5.98 μm, not a significant reduction from the original value of 8.57 μm. N_e for test case 6 is even worse, corrected only to 7.04 μm. The effects of Z13 and Z25 are visible in the residual surface error, also. As shown in Figures 6-8 and 6-9, the surface error is caused mostly by Z13 in both test cases, producing overall rms values of 1.16 μm and 1.35 μm for test cases 9 and 10, respectively. Neither correction is significantly smaller than the original value of 1.51 μm.

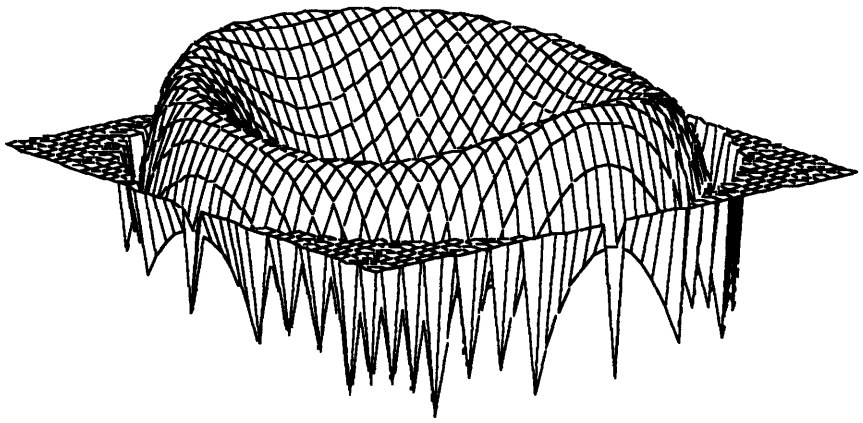

Figure 6-8
Residual Surface Error on Panel 2 - Test Case 9

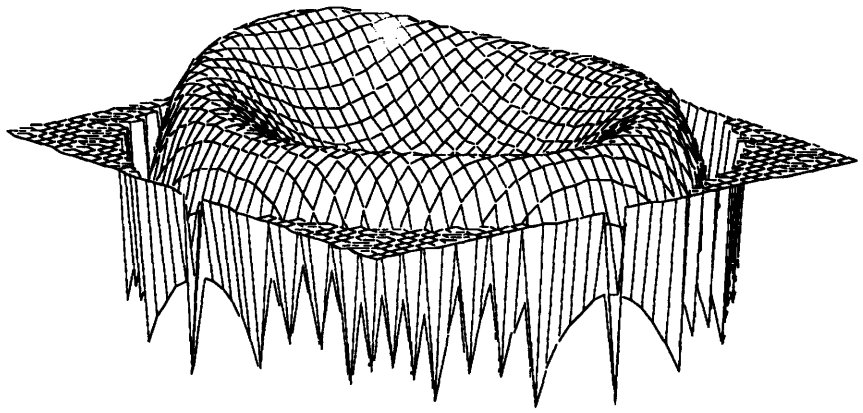

Figure 6-9
Residual Surface Error on Panel 2 - Test Case 10

The optical performance parameters were also poorly corrected. COMP analysis calculated a residual rms WFE of 1.88 μm for test case 9 and 1.72 μm for test case 10. Both residual errors were too large to be considered linear; therefore, COMP was utilized to determine the resulting Strehl ratios. Figures 6-10 illustrates the corrected point spread function map of test case 9. While the image has regained some symmetry not seen in the original aberrated image (Fig. 5-11), the scattering is still too great to resolve dim off-axis objects. The Strehl ratio was improved to only 0.234.

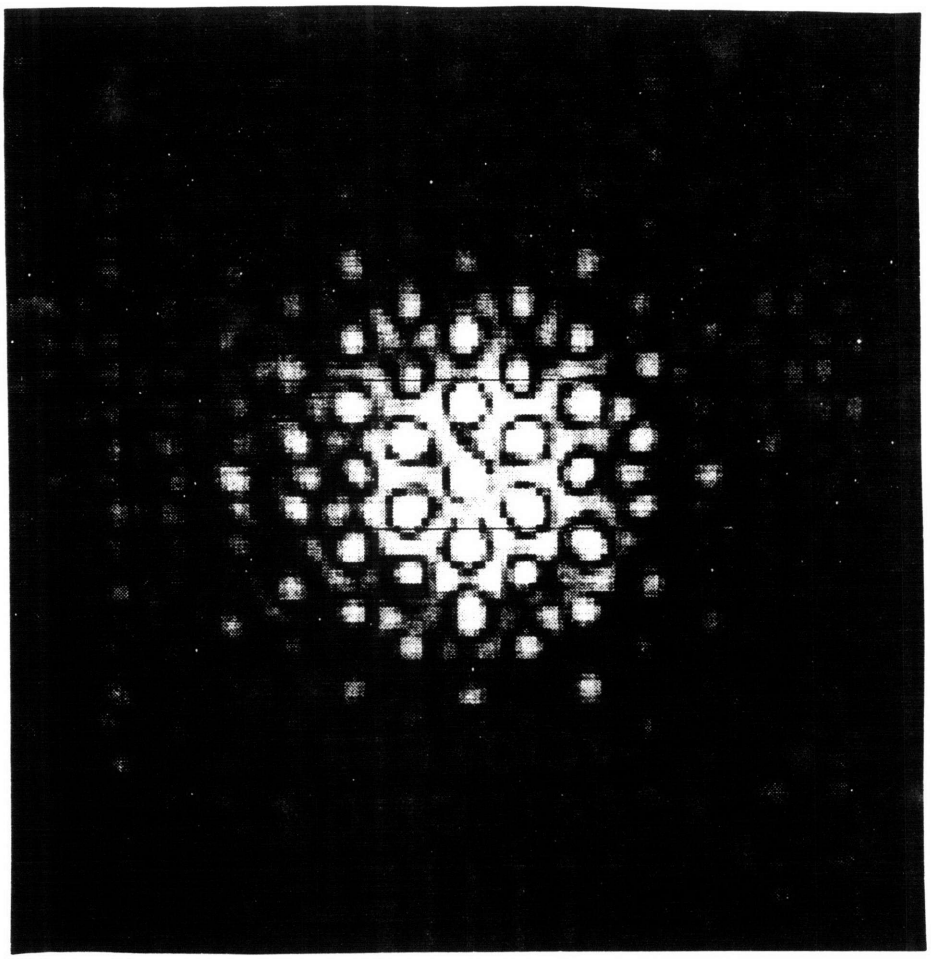

Figure 6-10
Corrected PSF Image - Test Case 9

The correction performed by test case 10, although still insufficient to consider the residual error a linear perturbation, improved the Strehl ratio and intensity distribution quality considerably over that of test case 9 (Fig. 6-11). The corrected SR is 0.283, a 20% increase over test case 9. In addition, the point spread function (PSF) has regained superior resolution of the primary diffraction lobes around the central point.

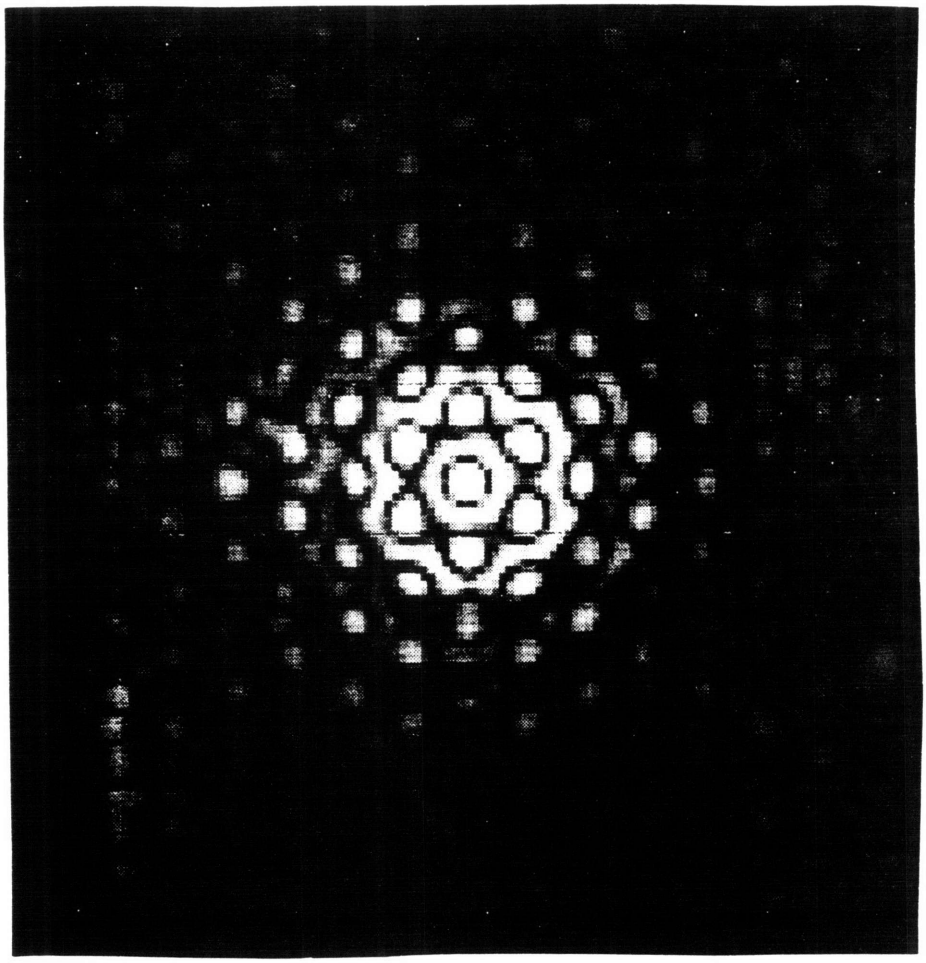

Figure 6-11
Corrected PSF Image - Test Case 10

Another remarkable fact is the actuation effort required for the two cases. Both cases showed actuation levels on the order of 340 V per actuator, similar to those of test cases 5 and 6. Test case 10 utilized only 51 actuators for correction as opposed to 69 for test case 9. Therefore, the total effort for case 10 is 26% less than that of case 9. Table 6-3 summarizes the corrected performance parameters for test cases 9 and 10 compared to the combined aberration.

Table 6-3 Underconstrained Correction Results of Combined Aberration

	Uncorrected Combined Aberration	Test Case 9 Results	Test Case 10 Results
Error norm (N_e)	8.57 μm	5.98 μm	7.04 μm
Act.norm (N_a)	N/A	45.1	34.1
Eigenvalue (Λ)	.087	.0982	.0588
rms WFE (μm)	2.49	1.88	1.72
rms SE (μm)	1.51	1.16	1.35
Strehl ratio	.086	.234	.283
# of actuators	N/A	69	51
operating wavelength = 10 μm			

In conclusion, the reduced number of actuators used in the underconstrained correction of the combined aberration could not produce a significant improvement in the performance parameters of the reflector system. This is due partly to the fact that the remaining actuators had little or no influence over the higher order Zernike deformations. However, correction with respect to wavefront error provided a correction 20% higher in Strehl ratio with 25% less actuator effort than the correction with respect to surface error. Such superior correction is now investigated in test cases 11 and 12, correcting for the thermal aberration.

6.2.2 Correction of Thermal Aberration

The results of test cases 11 and 12, involving the correction of the thermal aberration using the underconstrained control cases, are the most interesting as they most closely approximate actual operating conditions encountered by the reflector system. The results of test case 11 are presented first, followed by those of test case 12. Both sets of results are then summarized and compared.

6.2.2.1 Minimization of Surface Error

Test case 11, correcting with respect to surface error, provided a very good minimization of the residual error $\vec{e}$. The corrected Zernike distributions in the reflector panels, shown in Figures 6-12 clearly illustrates a significant reduction in the Zernikes most prominent on panel 2 under thermal aberration, Z2 through Z6. In panel 2 the most dominant Zernike

term, Z6 (x-axis astigmatism), was reduced from nearly 3.0 μm to 0.10 μm. Z5 (defocus), another prominent term in the original aberration, was scaled down by more than a factor of two to 0.4 μm. On the contrary, higher order Zernikes such as Z28 and Z36 grew considerably in magnitude. As shown in section 3.3, these Zernikes are relatively weak in their effects on the surface error. It therefore makes sense that the prominent Zernikes were reduced at the cost of enlarging these weaker Zernikes.

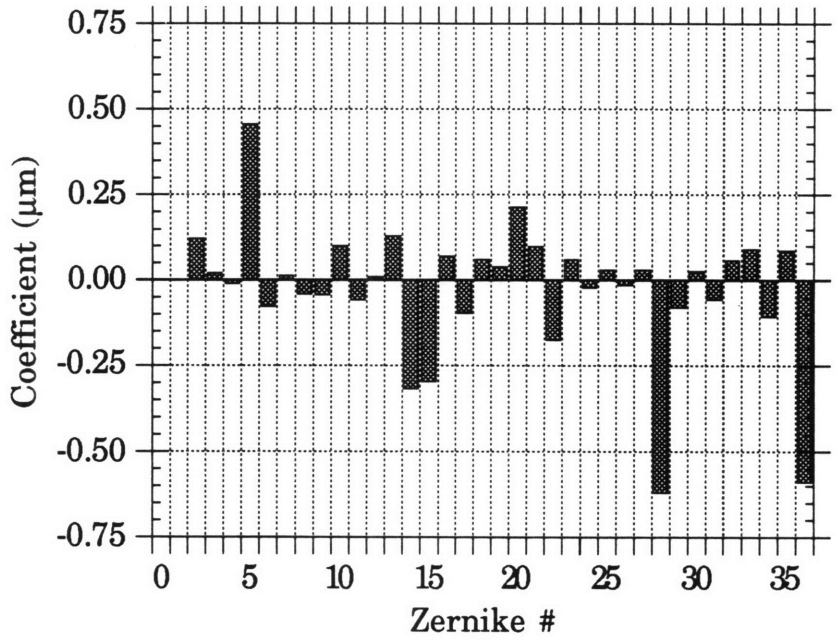

Figure 6-12

Zernike Distribution for Test Case 11 - Panel 2

Panel 3 showed similar results (Fig. 6-13). Both Z5 and Z6 were reduced in magnitude by a factor of four, with a corresponding increase in the higher Zernike terms Z28 and Z36. In addition, Z2 and Z3 (x and y-axis tilt) were completely eliminated. This may account for the significant increase in Z10 (primary trifoil), another Zernike with relatively weak influence on surface error. The Zernike corrections of all six panels resulted in a residual error norm N_e of 2.58 μm.

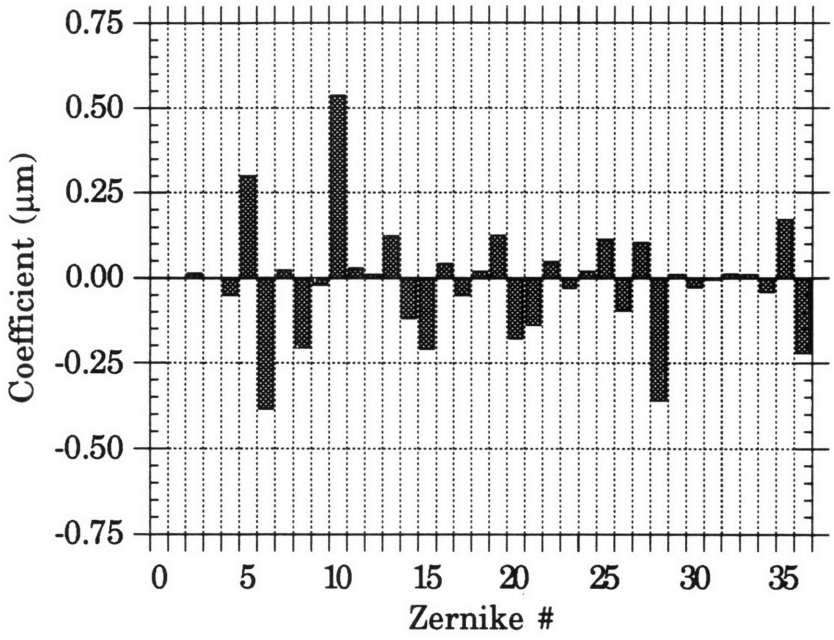

Figure 6-13
Zernike Distribution for Test Case 11 - Panel 3

Translated into surface deformations, the residual rms surface error over all six panels was 0.324 μm, down from 0.912 μm. Figures 6-14 and 6-15 illustrate the relatively flat residual errors after correction. Note again that much of the edge deflections are phenomena of the Zernike description on the unit circle.

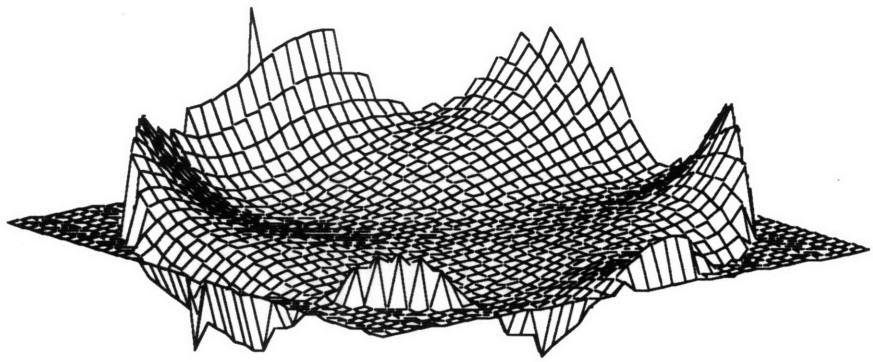

Figure 6-14
Residual Surface Error on Panel 2 - Test Case 11

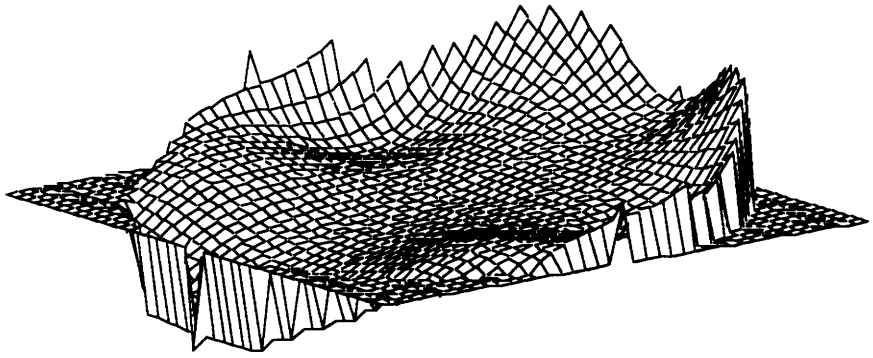

Figure 6-15
Residual Surface Error on Panel 3 - Test Case 11

The actuator effort required for the correction of test case 11, in terms of the actuator norm N_a, was 28.6, equivalent to an rms actuation voltage of 238 V for each of the 60 active actuators. Although the number of actuators used in test case 11 is 1/3 that of the number used in test case 7, the determinate correction of the thermal aberration with respect to surface, the total actuator effort in test case 11 is greater, possibly because the "ideal " actuators needed for the correction of the thermal aberration were not retained in the underconstrained case. This suggests that an alternate method of selecting actuator positions other than by setting a minimum actuation threshold is required.

The improvements in optical performance results were very good. The rms WFE was reduced to 0.588 μm ($\lambda/17$), from which the analytic Strehl ratio was predicted to be 0.862. This differed by only 1% from the measured Strehl ratio of 0.871. This increase in Strehl ratio was accompanied by a significant clarification of the original aberrated point spread function (Fig. 6-16). While the corrected PSF does not exhibit the distinct diffraction rings of the nominal PSF, the image has regained much of its symmetry, and the central point and first diffraction ring are better defined.

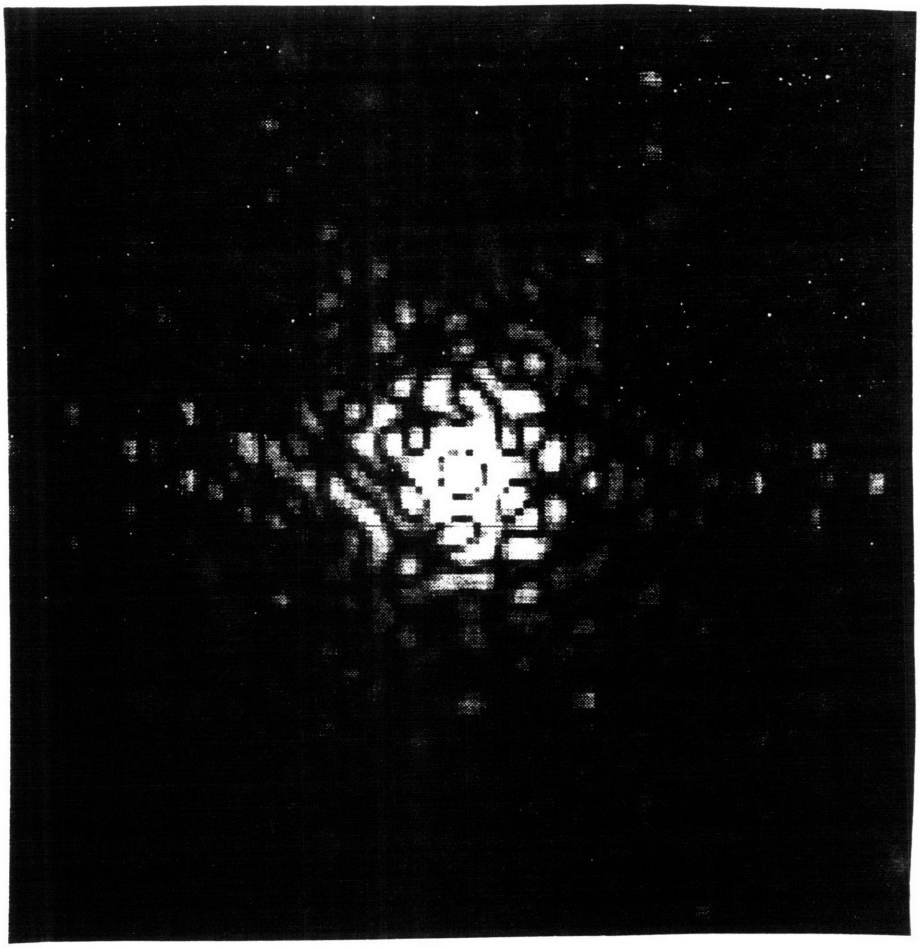

Figure 6-16
Corrected PSF Image - Test Case 11

A one dimensional intensity distribution plot, derived from Figure 6-16 by measuring the intensity values along the vertical axis, better illustrates the residual scattering of test case 11 (Fig. 6-17). The corrected distribution matches the nominal distribution closely up to an angular separation of 2.5 arcseconds (12 μrads), with the exception of an increase at 1.5 arcseconds. Beyond 2.5 arcseconds, however, the corrected distribution scatters lights considerably, obliterating the nominal diffraction pattern.

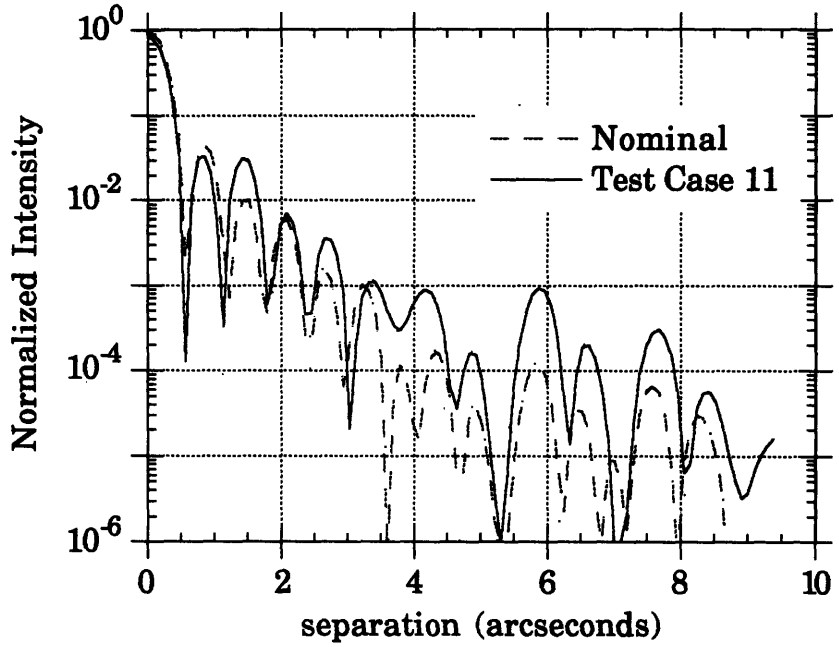

Figure 6-17

One Dimensional Intensity Distribution - Nominal vs. Test Case 11

Table 6-4 lists data taken from Appendix A.6, which tabulates the peak dwarf-to-scattered background signal ratios for several star/dwarf combinations at various angular separations. Values are given for each combination under nominal, thermally aberrated and corrected conditions.

Table 6-4 Peak Dwarf-to-Scattered Background Signal Ratios

Object Combination	Separation (aseconds)	Nominal Ratio	Aberrated Ratio	Test Case 11 Ratio
3600 K star/ 2400 K dwarf	1.0	2.44	6.22	3.02
6000 K star/ 2400 K dwarf	3.0	15.9	1.05	9.42
"	4.0	35.2	209.	3.50

The three combinations illustrate the nature of the test case 11 correction. The first row of data shows the approach of the corrected ratio toward the nominal value. Unfortunately, the thermally aberrated ratio was superior to begin with. The second row illustrates an

"ideal" correction in which the corrected value approaches the nominal value from an otherwise poor dwarf-to-background ratio. The final row represents the unwanted correction, where a superior aberrated value has been corrected to a lower ratio than that of the nominal. From these data, it can be said that a good correction of the Strehl ratio does not necessarily correspond to an improvement in scattering over the field of view.

In conclusion, the results of test case 11 indicate that an underconstrained system weighted towards the minimization of surface error can effectively correct a thermal aberration above what is considered good (SR $\geq$ 0.8). The total actuator effort required for correction is higher than that for the equivalent determinate correction, however, indicating that a better selection of an underconstrained actuator layout was possible. Lastly, the analysis of the corrected intensity distribution indicated that an improved Strehl ratio does not necessarily correlate with an improved distribution. The results of test case 12 are now discussed for later comparison with test case 11.

6.2.2.2 Minimization of Wavefront Error

Test case 12, correcting the thermal aberration with respect to wavefront error, also significantly reduced the size of the residual error vector $\vec{e}$. Figures 6-18 illustrates the residual Zernike coefficient distributions in panels 2 and 3. It is apparent that the Zernikes most dominant in the thermal error, Z2 through Z6, have been reduced to levels comparable to the remaining Zernikes.

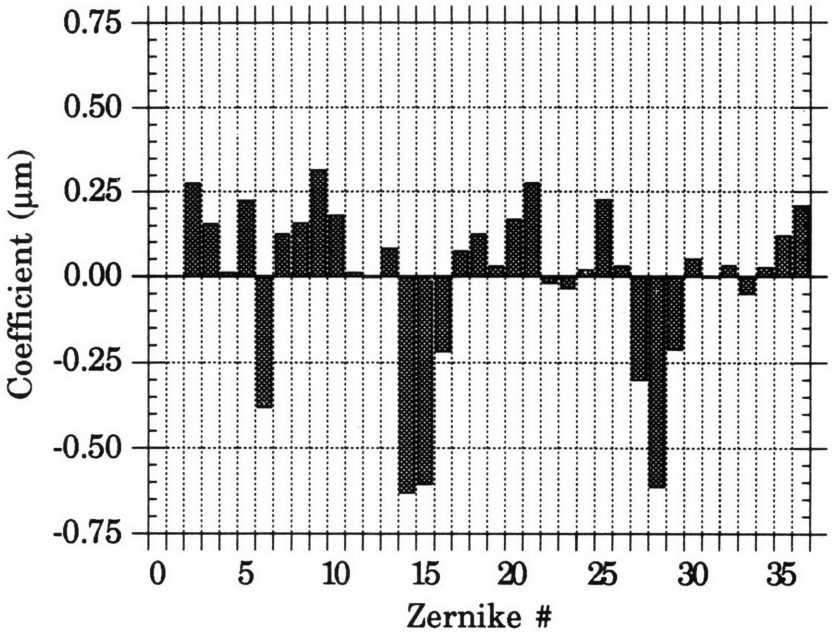

Figure 6-18

Zernike Distribution for Test Case 12 - Panel 2

Z6 (y-axis astigmatism), the largest term in both panels 2 and 3, was lowered to below 0.50 µm. Z5 (defocus), previously evaluated as the Zernike most detrimental to wavefront error (see section 3.3), was reduced below 0.25 µm. To counter the reduction in Z2 through Z6, higher order Zernikes such as Z14, Z15 and Z28 increased substantially in magnitude. These terms in the residual error of panel 2 are larger than 0.60 µm, all of which were near zero in the original aberration. Similar results are seen in panel 3 (Fig. 6-19).

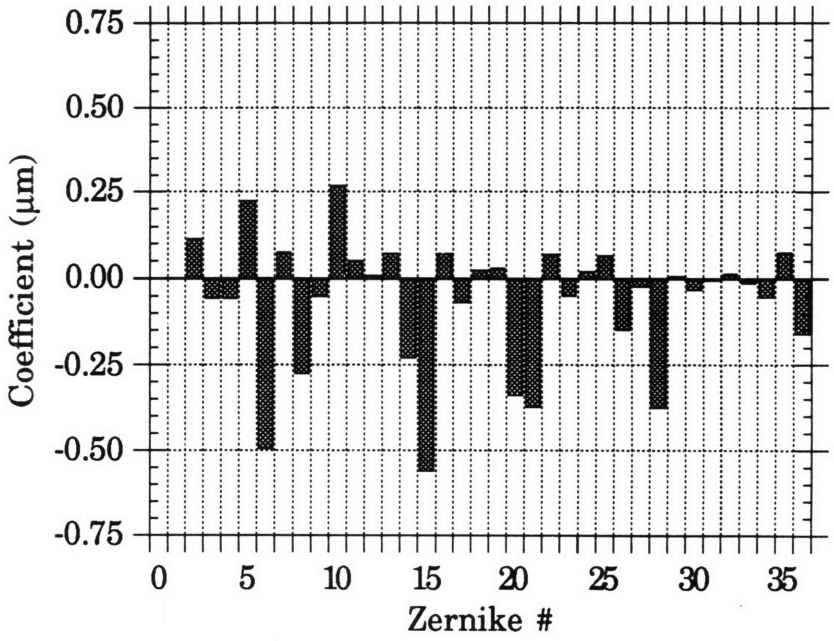

Figure 6-19

Zernike Distribution for Test Case 12 - Panel 3

In addition, panel 3 exhibited a considerable increase in Z20 and Z21, as both terms approached 0.35 μm in magnitude. Shown in Figure 3-7, all of the aforementioned higher order Zernikes have considerably less effect on wavefront error in comparison to Z2 through Z6. Therefore, the minimized cost function reduced the most detrimental Zernikes at the expense of increasing the magnitude of these weaker terms. The overall residual error $\vec{e}$ of the reflector system has an error norm of 3.07·μm, a 45% reduction from the original norm of 5.54 μm. This reduction is reflected in the residual surface errors in the panels. Illustrated in Figure 6-20, the corrected surface of panel 2 is fairly flat in the center. Panel 3, shown in Figure 6-22, is also relatively smooth in the center, although the effects of Z6 and Z15 are still noticeable. The overall rms surface error was 0.388 μm.

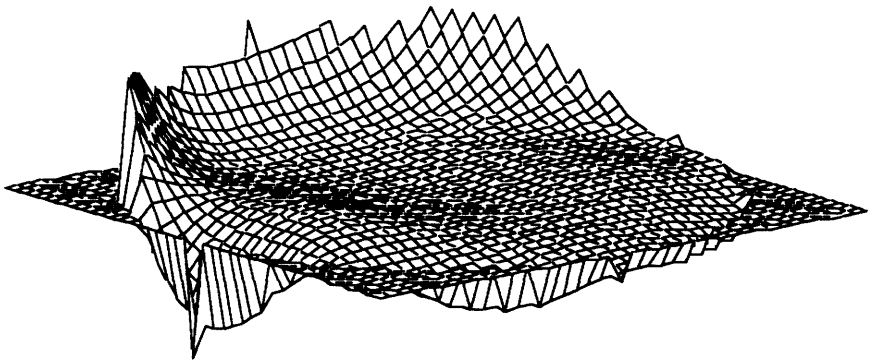

Figure 6-20
Residual Surface Error on Panel 2 - Test Case 12

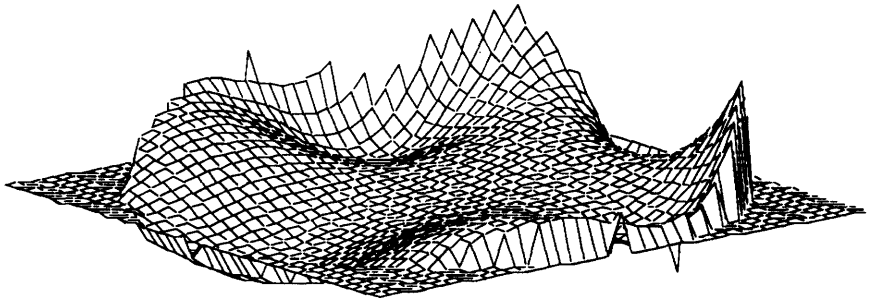

Figure 6-21
Residual Surface Error on Panel 3 - Test Case 12

The improvements in the optical performance parameters were substantial. The eigenvalue Λ of the residual error, its relative strength in degrading the Strehl ratio, was reduced three-fold to 0.031. This improved the rms WFE to 0.538 μm, also a factor of three. The resulting Strehl ratio, as predicted by the linear analytic model, was 0.884. This is slightly more than 1% from the measured value of 0.891. This substantial increase in Strehl ratio brought about a recovery of the point spread function nearly identical to that in test case 11 (Fig. 6-16). Slight differences can be seen, however, in the one-dimensional intensity distribution of Figure 6-22. In addition to a higher Strehl ratio, the distribution of test case 12 followed the nominal distribution more closely up to o 2.0 arcseconds. From 4.0 to 6.0 arcseconds, however, the distribution of test case 12 shows a slightly greater scattering of light over that of test case 11. It was therefore assumed that dwarf-to-background data similar to that in Table 6-4 would be obtained for test case 12.

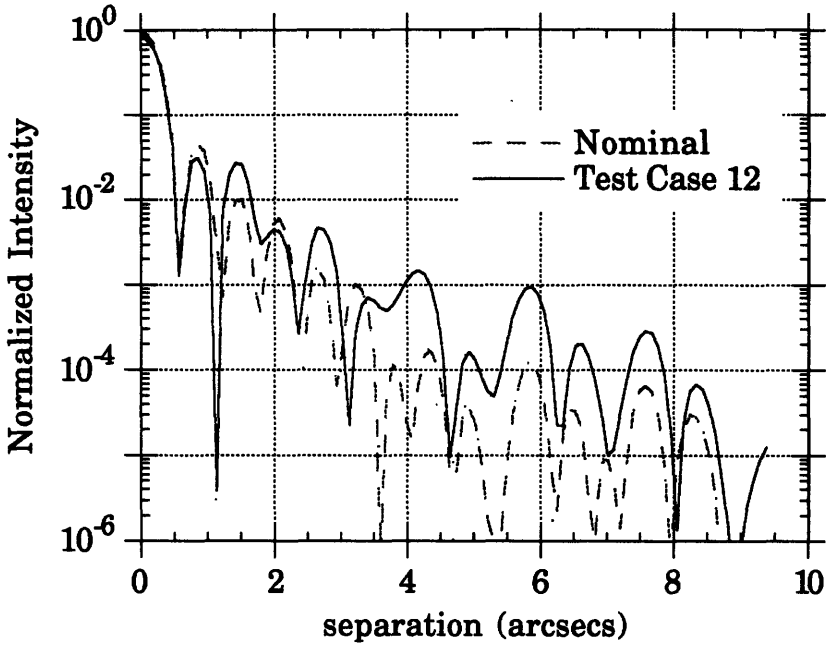

Figure 6-22

One Dimensional Intensity Distribution - Nominal vs. Test Case 12

A comparison between test cases 11 and 12 is now made to find any advantage in using one control algorithm over the other for the underconstrained correction of the thermal aberration. The comparison is made with the emphasis placed on the corrected image quality and actuator effort.

6.2.2.3 Test Case Comparison

Table 6-5 summarizes the results of the previous two sections for test cases 11 and 12. The final column represents the increase or decrease in values of test case 12 relative to those of test case 11.

Table 6-5 Underconstrained Correction Results of Thermal Aberration

	Thermal Aberration	Test Case 11 Results	Test Case 12 Results	Case 12/ Case 11
Error norm (N_e)	5.54 μm	2.58 μm	3.07 μm	+18.9 %
Act.norm (N_a)	N/A	28.6	31.9	+11.5 %
Eigenvalue (Λ)	.091	.0526	.0311	-41.0 %
rms WFE (μm)	1.67	.588	.538	-8.5 %
rms SE (μm)	0.91	.324	.388	+19.8 %
Strehl ratio	.368	.871	.891	+2.3 %
# of actuators	N/A	60	60	0 %
operating wavelength = 10 μm				

It is apparent that both test cases have sufficiently corrected the thermal aberration to permit linear analysis of the optical system, although the means of achieving this varied between cases. Test case 11 reached a corrected Strehl ratio of 0.871 through the reduction of the surface error to an rms value of 0.324 μm. On the contrary, test case 12 reduced the surface error only to 0.388 μm. Its reduction of the rms WFE to 0.538 μm, however, improved the Strehl ratio to 0.891, a 2.3% increase over test case 11. Aside from different Strehl ratios, the resulting intensity distributions of the two cases differed very little in their resolution of dim off-axis objects. In addition, the improvement in Strehl is offset by an 11.5% increase in the actuator norm of test case 12 over test case 11. Therefore, to achieve this small increase in Strehl ratio required considerably more power from an equal number of actuators. From this, it appears that neither control algorithm has a distinct advantage in providing superior correction of a thermal aberration when operated in an underconstrained system.

One explanation of the small differences in the test results may be the fact that the thermal aberration consists almost entirely of low energy, large scale Zernikes which are readily correctable by many available actuators. This is supported by the previous observation that the test cases used identical actuator layouts to the correct the thermal aberration. Another explanation is the strong correlation between the surface and wavefront errors induced by these low order (≤ Z6) Zernikes, as shown in chapter 3. Therefore, the use of identical actuator layouts is not unusual. Results of test cases 9 and 10, however, indicated a significant advantage to using wavefront control for the correction of higher order aberrations beyond astigmatism and defocus. Although neither test case provided a good

improvement for the Strehl ratio, the relative improvements of wavefront control over surface control in terms of Strehl ratio and actuator effort were considerable. Unfortunately, no further work was done to verify this observation.

The results of test cases 11 and 12 as well as those of preceding test cases are subject to questioning and verification because of errors which were incurred in the process of obtaining the data. Known errors which were present in this research are now discussed, and their effects on the test results are quantified when possible.

6.3 Error Analysis

The primary errors incurred during the collection of information can be traced to modeling assumptions in both the optical and structural models. These errors are divided into groups relating to each model, and are evaluated in that context.

6.3.1 Optical Model Errors

Errors in the optical modeling of the reflector system were, to say the least, expected. The Controlled Optics Modeling Package (COMP), the source program used for the generation of the optical model, was an evolutionary tool at the time of its use, and was being corrected and updated partially in response to the results it produced for this research. Many computational errors plagued the subroutines within COMP, including the incorrect definition of Zernike polynomials, and rays mysteriously vanishing before propagating fully through the system. As it was used for this research, COMP seemingly was successfully corrected for such computational errors. However, several other modeling errors remain, and are presented in order of the severity of their effects.

The first minor modeling assumption made within COMP is the negation of any seams between between the segmented reflector panels. In reality, independently moving panels would have seams approximately 2 mm to 5 mm in width separating them. Such seams would affect the diffraction patterns around the edges of the panels, although it was not considered significant. This effect, however, cannot be quantified short of redeveloping the optical model with seams included.

Another modeling approximation already mentioned is the optical sensitivity C-matrix developed for the higher order model. This matrix, relating wavefront error to changes in

reflector surfaces defined by Zernikes, was constructed using a one step finite difference method. Each Zernike was placed into all panels simultaneously with a coefficient of 2.0 μm, and the resulting optical pathlength difference (OPD) was measured for each ray. The slope $\partial OPD/\partial C_t$ was found to be fairly constant up to coefficients of 3.0 μm, above which it began to rise slowly. Therefore, surface aberrations with Zernike coefficients approaching this value may have been incorrectly represented in terms of their effect on wavefront error when calculated using the linear analytic solution for the Strehl ratio. This was shown to be the case in the tests performed. On the average, the predicted SR was 1% to 2% lower than that calculated by COMP. For the aberrations encountered, this was not considered to be a significant problem.

A similar modeling error arises in the definition of the panels within COMP. Because the deformations, both rigid body and Zernike, are defined about the central rotation point of each panel, any discrepancy in accuracy between panel descriptions would cause identical aberrations on symmetric panels to produce considerably different effects on the wavefront.[42] This error exists in the model presented in this report, as shown in the results of Table 3-1. For example, two eigenvectors which should have had equal effects on the wavefront error are the pistoning of panels 5 and 7 and the pistoning of panels 2 and 4. The eigenvectors are identical in their motions, but occur on opposing panels. However, the corresponding eigenvalues are .6364 and .5345, respectively. This indicates that one aberration has a greater effect on the Strehl ratio although the aberrations are the symmetric about the reflector's center. Therefore, the characterization of the reflector system's performance is somewhat flawed. Perhaps the two most significant optical modeling errors, involving the use of Zernike polynomials, remain to be evaluated.

The two remaining known optical modeling errors stem from the use of a finite series of Zernike polynomials to describe the panel surface aberrations. The first involves the accuracy of the COMP model when compared to the higher resolution NASTRAN structural model. Whereas COMP uses 36 Zernike polynomials transformed by the D-matrix (section 5.3) to generate point displacement data, the NASTRAN model directly outputs displacement data at 331 grid points. Therefore, the Zernike series may have truncated high order deformations which exist in the NASTRAN model. To quantify this, the actuation levels which minimized the errors in test cases 11 and 12 were simulated in

---

[42]Redding, D., Milman, M., Loboda, G. "Linear Analysis of Opto-Mechanical Systems", SPIE Aerospace Sensing Conference, Orlando (1992), p. 15.

the NASTRAN model along with the aberration generated by the thermal gradient. The residual rms surface error was then calculated over the 331 gridpoints using READZ. An rms surface error was obtained from the COMP displacement data through the D-matrix. The comparison of the two models' results are shown in Table 6-6.

Table 6-6 Comparison of NASTRAN and COMP rms Surface Error

	NASTRAN	COMP	% Error
Test Case 11	.324 μm	.333 μm	2.75 %
Test Case 12	.388 μm	.392 μm	1.03 %

From these results, it seems that there was little residual surface error in the NASTRAN model which was unresolvable by the 36 Zernike terms. This may partly be due to the low order nature of the thermal aberration, requiring relatively low levels of actuation from the piezos. For other aberrations where the weight of the deformation lies in higher order Zernikes, the greater effort required from the actuators would produce larger localized deformations, leading to a greater discrepancy between the NASTRAN and COMP descriptions of the surface error.

The second modeling error involves the effect of very high frequency surface roughness on the correction performed by the actuators. This roughness, although unobservable and therefore uncorrectable by the control scheme, is created by manufacturing imprecisions. It has been quantified experimentally to magnitudes of 1 μm to 2 μm rms surface error, although it could possibly be polished down to 0.5 μm.[43] A "back of the envelope" calculation was performed to evaluate the effects of 0.5 μm surface roughness on corrected test case 12. First, the surface roughness was modeled as a combination of all Zernike polynomials from the 8th to the 130th order (Z37 to Z8646), equal to a minimum aberration spatial frequency of 1.0 cm. Plotting the effective eigenvalue Λ for the first 36 Zernikes against Zernike number, the best fit curve to the data produced the following relation:

$$\Lambda \approx .223Z^{-0.6} \tag{6.1}$$

where Z is the number of the Zernike term, and Λ is the corresponding eigenvalue. The average eigenvalue was then approximated by:

---

[43]Conversations w/ E. Hochberg (JPL section 385), November 1991.

$$\Lambda_{avg} \approx \frac{1}{Z_f}\int_0^{Z_f} .223Z^{-0.6} \tag{6.2}$$

where Z_f is the number of Zernike terms in the series, 8646 in this case. For this approximation, $\Lambda_{avg} = .0024$. A relation was then determined between $\partial WFE/\partial SE$ and eigenvalue again using data from the first 36 Zernikes. A first order fit to the data produced:

$$\partial WFE/\partial SE \approx 1 + 20\Lambda \tag{6.3}$$

The effective eigenvalue for the combined aberration of the surface roughness and the residual aberration of test case 12 was taken to be the average of their respective eigenvalues, equal to .0168. A final approximation for the net surface error of the combined aberrations was then made. This was taken to be the root square of the individual rms errors. These data for surface error and eigenvalue were then used to solve Eq. 6.3 for an effective wavefront error. Assuming nearly linear perturbations (WFE $\approx \lambda/14$), the analytic form of Strehl ratio was used to predict SR. The results of this modeling of the surface roughness is summarized in Table 6-7.

Table 6-7 Effects of Modeled Surface Roughness on Reflector Performance

	Test Case 12 Correction	Roughness Only	Net Error (approximate)
rms surface error	.388 μm	.5 μm	.633 μm
eigenvalue	.0311	.0024	.0168
rms WFE	.538 μm	.524 μm	.846 μm
Strehl ratio	.891	.890	.71 - .75
operating wavelength = 10 μm			

From these results, it seems that 0.5 μm of high frequency surface roughness could reduce the Strehl ratio of the corrected system by 20% at λ = 10 μm, although the increase in scattering would be fairly homogeneous over the field of view. Such reduction may be acceptable, although larger magnitudes of surface roughness would have a much greater impact on the Strehl ratio. From an optical standpoint, the unmodeled surface roughness

poses the biggest threat to a good correction using piezo actuators. Additional sources of error found in the structural modeling of the reflector panels may prove equally detrimental.

6.3.2 Structural Model Errors

The structural model of the reflector panels has an advantage over the optical model in being (1) generated by a long standing and widely accepted finite element program, NASTRAN, and (2) based on an existing model which has been verified empirically. However, several modeling errors still exist which are worth discussing.

The first modeling error is the non-linearity of actuator strains and the deformations caused by them. The issue of non-linearity of actuator strains was already addressed in chapter 4, where the restriction on maximum strain of 50 μstrain provided a fairly linear operation envelope for the actuators. The issues of creep and depolarization were not addressed, however, and may play a role in lessening the effectiveness of the actuators. The linearity of summing deformations from multiple actuations was verified previously in the comparison between NASTRAN and COMP residual surface errors after correction through test cases 11 and 12. Therefore, the linear assumptions made for the structural model are fairly accurate, and do not present a major source of error.

A more significant error may occur due to a simplification of the structural modeling. The bond between the piezo actuators and the panel facesheets was assumed perfect, with no shear lag. This has been shown empirically to be false, as much of the strain energy from the actuators is lost on the adhesive. Such a condition would lessen the effect each actuator has on deforming the panel, and would require the use of more actuators to perform a correction. This condition cannot be verified short of the redevelopment of the structural model with an adhesive layer modeled into the actuator elements.

Another error is the insufficient fidelity in the NASTRAN model to resolve the localized high frequency deformations caused by the actuator strains. Similar to surface roughness, these deformations may significantly impact the optical performance of the reflector. Because each actuator is defined at only 3 points, the current model of 331 grid points on a panel face cannot "see" local wrinkling around the energized actuators. To achieve this, the fidelity of the model would need to be increased several-fold. Current NASTRAN codes limit the maximum number of degrees of freedom, thereby making the increase nearly impossible to accomplish. Attempts at this during this research attest to that fact. In

addition, NASTRAN is not a "user friendly" program, and a model of this size would be extremely difficult to manage and debug. Therefore, the lack of fidelity in the structural model is a situation not soon to be remedied.

A final point of uncertainty lay in the actual use of Zernike polynomials to describe the deformations produced by the actuators. The virtual constraint placed at the center of the NASTRAN model prohibited motion of the panel's centerpoint, thereby eliminating the need to model Z1, the pistoning error. Initially, this did not seem to pose a problem for the remaining Zernikes, as they were thought to be defined equal to zero at the panel's center (i.e, $\rho = 0$). This is untrue, however. Those Zernikes which are functions of ρ only (Z5, Z13, Z25, etc.) each have a bias of ± 1 at $\rho = 0$. Therefore, the correct fitting of these Zernikes may have been altered by the center constraint. No attempt was made to evaluate this uncertainty, however.

In conclusion, most known sources of error were traced to the optical and structural models developed for the reflector system. The primary optical errors are based on the use of 36 Zernike polynomials for the description of surface aberrations. This series of Zernikes did not have the sufficient resolution to observe higher frequency local deformations of the structural model or the high frequency surface roughness associated with the manufacturing process. For the test cases cited, the discrepancy between optical and structural model estimations for residual surface error was very small. The unobservable surface roughness, when modeled as very high order Zernikes, appears to significantly degrade the otherwise good correction performed by the piezo actuators. Structural modeling errors, although not as significant, also stem primarily from an inability to resolve localized deformations caused by the actuators. This cannot be easily corrected because of the computational expense involved in creating a larger structural model.

6.4 Conclusion

This chapter has presented the results of the test cases performed to quantify the level of correction attainable by the determinate and underconstrained actuator control cases. Test cases 5 through 8, corresponding to the determinate control case, all exhibited an excellent ability to reduce both wavefront and surface errors to achieve the desired Strehl ratio of 0.8 or above. The correction of the combined aberration, however, required much more actuator effort to counter the high energy higher order Zernike terms prevalent in the aberration. Test cases 9 through 12, operating as underconstrained control schemes,

provided interesting insight into the limits of surface correction through the use of surface mounted piezoelectric actuators. Test cases 9 and 10, correcting for the combined aberration, did not significantly reduce either the surface or wavefront errors to produce a quality image because the active actuators did not have sufficient influence over the larger higher Zernike terms in the aberration. In comparison, however, correcting with respect to wavefront control showed a significantly better Strehl ratio and residual scattering with less actuator effort than that achieved through surface control. This indicates a potential advantage in the correction of higher order aberrations beyond astigmatism using wavefront control methods. Finally, both test cases 11 and 12, using identical actuator layouts, corrected the thermal aberration Strehl ratio from 0.37 to above 0.8. The corrections also returned the intensity distribution to a close approximation of the nominal, although improvements of the dwarf-to-background signal ratios were not consistently positive. Wavefront error control gave a superior Strehl ratio by 2%, although the required actuator effort for this was 12% greater than that for surface control. Therefore, no distinct advantage was found in either control method in correcting thermal gradient induced aberrations in composite reflector panels. Several modeling errors in both structural and optical models indicate that the limited fidelity of these models in resolving high order surface aberrations may considerably misrepresent the actual level of correction attained by the control scheme.

Chapter 7

Conclusions and Recommendations

This chapter summarizes chapter 2 through chapter 6 of the report with respect to the approach stated in chapter 1. The principal steps of the approach are described within the context of each chapter, and conclusions are drawn from the results. Recommendations for improvement and future research are then given.

7.1 Summary and Conclusions

Chapter 2 dealt with the definition of the hypothetical reflector system and its operating parameters. A segmented panel primary composed of six hexagonal composite panels was designed with a maximum diameter of 3.90 m to be used in a Cassegrain telescope configuration. Diffraction limited angular resolution values were determined for various star/dwarf combinations as functions of operating wavelength, based on Black's Law for objects of very dissimilar intensities. In addition, signal-to-noise ratios were determined for several dim secondary objects as functions of telescope temperature, ambient noise and integration time. It was concluded from the above analyses that a minimum angular resolution was obtained at an operating wavelength of 10 μm, and that signal-to-noise ratios were maximized at telescope temperatures at or above 100 K and integration times above 1000 seconds. These operating values were then used as reference points in the remainder of the report.

Chapter 3 developed several principal concepts for the optical analysis of a segmented reflector system. A closed analytic solution for the Strehl ratio was developed assuming small linear perturbations in the panels from the nominal system. In addition, a low order optical model was created to (1) characterize those rigid body motions which most adversely affect Strehl ratio, and (2) verify the predictions for the Strehl ratio (SR) provided by the linear analytic solution. An eigen-decomposition of the analytic optical sensitivity matrix was performed to determine the normal modes of the system with respect to Strehl ratio. It was concluded that opposing piston motions in symmetrically placed panels most severely degrade the Strehl ratio. The analytic solution for SR was then shown to be accurate to within 5% of the low order model SR for rms wavefront errors up to $\lambda/14$. Last, a higher order model using a finite expansion of Zernike polynomials to

describe panel aberrations was developed and characterized through an eigen-decomposition of a numerical optical sensitivity matrix constructed through finite difference approximations. COMP provided information on wavefront and surface errors which resulted from individual Zernike aberration vectors. Analysis showed that several Zernike aberrations beyond piston and tilt errors exist which significantly degrade Strehl ratio, primarily astigmatism, higher order spherical aberration and defocus. In addition, a strong correlation between wavefront and surface errors was noted for these same Zernikes. These results provided sufficient justification for the use of surface mounted actuators to correct for these higher order aberrations.

Chapter 4 focused on the development of structural model of a composite reflector panel under loading by surface mounted piezoelectric actuators. The structural model of the hexagonal panel was created within NASTRAN, based on an empirically verified model used in the PSR program. The piezoelectric (PZT) actuators were integrated into the panel model as rod elements, and their electromechanical strain behavior was modeled as an equivalent thermal strain assuming linear strain behavior over a limited actuation range. Each panel model was mounted with 66 PZT actuators aligned in a configuration to simulate the radial and azimuthal behavior of Zernike polynomials. Individual actuators were energized, and the resulting deformations were characterized using 36 Zernike polynomials equal to those used in the optical model. From this, a control "transfer function" matrix was assembled. This matrix related actuation energization to panel deformation defined in terms of Zernikes, thereby providing a link to the Zernike based optical model for the active correction of surface aberrations. The characterization of the deformations showed that (1) a great deal of symmetry exists among actuators in terms of net strain and resulting panel deformations, and (2) the piezo actuators induce primarily lower order Zernike deformations such as astigmatism and tilt. Few actuators showed any strong influence over Zernikes above Z11, primarily because these higher order deformation shapes require more strain than could be provided by any individual actuator.

Chapter 5 dealt with the development of a control scheme to evaluate the abilities of surface mounted piezoelectric actuators to minimize surface aberrations described by Zernike polynomials. Two test aberrations based on a thermal gradient model of composite reflector panels were created through NASTRAN. These aberrations, consisting mainly of astigmatism (Z6) and third order spherical (Z13), were evaluated for their effects on the reflector's optical performance through COMP. Both aberrations increased the wavefront error beyond what is considered linear with respect to wavelength, and significantly

lowered the Strehl ratio, resulting in a severe degradation of the intensity distribution of the focal plane image. This provided sufficient justification for the use of active control of these higher order aberrations. Two control algorithms, both based on a constrained least squares fit, were then developed for the minimization of surface and wavefront errors. Three control cases were then introduced, each representing a different number and configuration of actuators to be used in the control algorithms. The first, overconstrained case utilized all 396 available actuators for correction, and completely eliminated the test aberrations in both control algorithms. The most active actuators of the overconstrained case were then selected for use in the last two control cases, determinate and underconstrained. The determinate control case, a first crude optimization of actuator placement, retained between 168 and 180 actuators over the six panels for correction of the test aberrations. These actuators were concentrated primarily in the outer ring of the original panel layout, where the greatest influence over Z6 and higher Zernikes was found. The underconstrained control case used 51 to 69 actuators for correction of the test aberrations with respect to surface and wavefront error, respectively. Again, the majority of actuators were found in the outer ring of the layout. In both determinate and underconstrained control cases, the test cases involved in the correction of the thermal aberration used identical actuator layouts for the minimization of both surface error and wavefront error. This was concluded to be a result of the low energy, large scaled nature of the thermal aberration, effectively described using only Zernikes below Z6.

Chapter 6 presented the results of the test cases performed to quantify the level of correction attainable by the determinate and underconstrained actuator control cases. Test cases 5 through 8, corresponding to the determinate control case, all exhibited an excellent ability to reduce both wavefront and surface errors to achieve the desired Strehl ratio of 0.8 or above. The correction of the combined aberration, however, required much more actuator effort to counter the high energy higher order Zernike terms prevalent in the aberration. Test cases 9 through 12, operating as underconstrained control schemes, provided further insight into the limits of surface correction through the use of surface mounted piezoelectric actuators. Test cases 9 and 10, correcting for the combined aberration, did not significantly reduce either the surface or wavefront errors to produce an acceptable image because the active actuators did not have sufficient influence over the larger higher Zernike terms in the aberration. In comparison, however, correcting with respect to wavefront control showed a 20% higher Strehl ratio and lower residual scattering than that achieved through surface control. In addition, less actuator effort was required to perform the wavefront control. This indicates a potential advantage in the correction of

higher order aberrations beyond astigmatism using wavefront control methods. Finally, both test cases 11 and 12, using identical actuator layouts, corrected the thermal aberration Strehl ratio from 0.37 to above 0.8. The corrections also returned the intensity distribution to a close approximation of the nominal, although improvements of the dwarf-to-background signal ratios were not consistently positive. Wavefront error control gave a superior Strehl ratio by 2%, although the required actuator effort for this was 12% greater than that for surface control. Therefore, no distinct advantage was found in either control method in correcting thermal gradient induced aberrations in composite reflector panels. Finally, sources of error in the optical and structural models were discussed, and their effects on the correction results were quantified when possible.

In conclusion, the research presented in this thesis report has addressed the issue of quasistatic shape control of composite reflector panels for the correction of surface aberrations, in particular those aberrations most detrimental to image quality. To find a solution, this issue was reduced to three principal objectives. The first objective required the definition and performance characterization of a reflector system to quantify the effects of various surface aberrations on image quality as defined by the Strehl ratio. This involved the use of both an analytic and optical model of the reflector system. The second objective required the development of a high fidelity structural model of the reflector panels. This was needed to resolve the deformations produced by surface mounted piezoelectric actuators as functions of actuator position and strain level. The third objective involved the integration of the structural and optical models of the reflector system into a control scheme to eliminate those surface aberrations which cause the most damage to image quality. Each of these objectives were met with a good amount of success. However, areas for improvement do exist, especially in light of the several modeling errors which still remain. Recommendations for the elimination of some of these errors are now given, along with recommendations for future research.

7.2 Recommendations

The first group of recommendations concerns the elimination or at least reduction of error in the research already conducted. Two errors in the optical model which should be corrected in future work is (1) the inaccurate definition of the optical model within COMP, and (2) the limited fidelity in observing errors by using 36 Zernike polynomials to describe the surface deformations. The first should be fairly easy to correct if a sufficient number of significant digits is used to define each parameter. Hand "number crunching" should be

avoided in defining the model, as this only aggravates the problem. This correction is contingent, however, on whether or not COMP is working correctly and does not incorrectly perform the diffraction analysis. The second error can be corrected either by increasing both the number of rays sampling the surface and the number of Zernike terms used to model the surface, or by switching to another method of surface fitting, such as zonal contour surfaces. In the case of modeling very high frequency aberrations like surface roughness, neither correction may be sufficient to resolve the entire error, and approximation methods such as the one discussed in the error analysis need to be implemented.

Two errors within the structural model are also considerable concern if future work is to be conducted on this topic. The first error involves the limited fidelity of the NASTRAN model in resolving the high frequency deformations produced in the immediate vicinity of an energized actuator. These deformations, which may cause a considerable level of surface error, are currently invisible because there are too few structural elements defining the panel surface. Although currently very difficult to accomplish, another model with many more gridpoints describing the displacement of the panel should be designed. Interferometric measurements performed by Hochberg involved 256 data points across the diameter of a panel to resolve such localized deformations.[44] A new structural model with this level of resolution would be desirable. The second error lies in the modeling of the adhesive bonding the facesheets to the core. Currently modeled as a laminate layer of the facesheet plate elements, the adhesive layer exhibits constant strain through its thickness, whereas the true adhesive layer strain would vary through its thickness. This could be corrected by modeling the adhesive as a separate solid body element. This should also be applied to the bond between the actuators and facesheet, which is currently modeled as perfect (i.e, no adhesive). Aside from the correction of these current modeling errors, there are several other points worth pursuing in future research.

The first point involves the reflector model used in this research. Consisting of only one ring of six hexagonal panels, this configuration was chosen for its simplicity and symmetry of panel position. A more complex but also more important problem is the characterization of a reflector with several rings of panels, where ideally a panel's effect on image quality is a function of its position in the reflector as well as the nature of its deformation. Revisiting the issues addressed in this thesis using a model such as this would provide much more

---

[44]Hochberg (1991), p. 1.

insight on the active control of reflector panels for larger systems. A second point is the selection of an alternate performance metric. Although Strehl ratio was a good metric to use when improving only the sharpness of a central bright image, it was not sufficient to correct the associated scattering of light onto dim secondary objects. To accomplish this, a metric such as encirclement of energy should be used, where the emphasis is on the distribution of energy rather than just a point value of energy.

Three other suggestions for further research involve the control scheme using surface mounted piezo actuators. First, the overconstrained control case discussed in this report utilized many more actuators than necessary to correct any surface aberration. In this situation, it may be possible to selectively eliminate any given Zernike component of the aberration without affecting the magnitudes of the remaining Zernike terms. This poses an additional question for study using an overconstrained system. The second point focuses on the influence of the actuators used over various surface aberrations. It was shown that most of the actuators affect only low order deformations described by Zernikes under Z10. Perhaps if alternate actuator layouts, actuator sizes and ranges of actuator strain were used, a greater influence over these higher order Zernikes could be achieved. This ties in to the last point for consideration. Underconstrained test results show that, when correcting aberrations with higher order Zernikes over which the actuators have little influence, the algorithm correcting for wavefront error provided a superior improvement in Strehl ratio and scattering levels over the correction for surface error. Further tests conducted similar to these may provide more insight into the effectiveness of this type of control.

In conclusion, the points for improvement include both the elimination of existing errors as well the expansion and embellishment of some concepts only briefly addressed in this research. The implementation of these improvements may result in a far better understanding of the issue of active control of reflector panels than has been presented in this report.

Appendices

A.1 Nearest Cool Stars[45]

The following is a list containing those stars within 6.5 parsecs of the Sun which have surface temperatures at or below ≈ 4000 K. These 73 stars are the most likely candidates around which brown dwarfs and/or planets may be detected. They are listed in order of increasing distance from the Sun.

Star Name	Parallax (arcsecs)	Distance (parsecs)	Star Type	Surface Temperature (K)
Proxima Centauri	0.762	1.3123	M5	2800
Alpha Centauri b	0.745	1.3423	K5	4130
Barnard	0.552	1.8116	M5	2800
Wolf 359	0.429	2.3310	M8	2400
36.2147	0.401	2.4938	M2	3150
L726-8	0.367	2.7248	M5	2800
UV Ceti	0.367	2.7248	M6	2700
Ross 154	0.345	2.8986	M4	2950
Ross 248	0.317	3.1546	M6	2700
L789-6	0.303	3.3003	M7	2550
Ross 128	0.301	3.3223	M5	2800
61 Cyg a	0.294	3.4014	K5	4130
61 Cyg b	0.294	3.4014	K7	3800
Eps Ind	0.291	3.4364	K5	4130
59.1915 a	0.283	3.5336	M4	2950
59.1915 b	0.283	3.5336	M5	2800
4344 a	0.282	3.5461	M1	3370
4344 b	0.282	3.5461	M6	2700
-36.15693	0.279	3.5842	M2	3150
51668	0.268	3.7313	M5	2800
-39.14192	0.26	3.8462	M0	3480
Kapteyn	0.256	3.9063	M0	3480

[45]Allen, C.W. *Astrophysical Quantities*, Athlone Press, London, 1976, pp. 235-240.

Kruger 60	0.253	3.9526	M3	3050

Star Name	Parallax (arcsecs)	Distance (parsecs)	Star Type	Surface Temperature (K)
D0 Cep	0.253	3.9526	M4	2950
Ross 614 a	0.25	4.0000	M7	2550
-12.4523	0.249	4.0161	M5	2800
Wolf 424 a	0.23	4.3478	M6	2700
Wolf 424 b	0.23	4.3478	M7	2550
-37.15492	0.225	4.4444	M4	2950
50.1725	0.219	4.5662	K7	3800
-46.1154	0.216	4.6296	M4	2950
-49.13515	0.214	4.6729	M1	3370
-44.11909	0.213	4.6948	M5	2800
L1159-16	0.212	4.7170	M8	2400
68.946	0.209	4.7847	M4	2950
-15.629	0.207	4.8309	M5	2800
40 Eri c	0.205	4.8780	M4	2950
15.262	0.205	4.8780	M4	2950
20.2465	0.203	4.9261	M4	2950
70 Oph b	0.195	5.1282	K5	4130
AC 79.3888	0.195	5.1282	M4	2950
43.4305	0.194	5.1546	M4	2950
AC+58 25001	0.192	5.2083	M4	2950
44.2051	0.186	5.3763	M2	3200
WX UMa	0.186	5.3763	M8	2400
-26.12036	0.184	5.4348	K5	4130
-20.4125	0.18	5.5556	K5	4130
-20.4123	0.18	5.5556	M2	3150
36.13940 b	0.177	5.6497	M5	2800
1.4774	0.175	5.7143	M2	3150
L347-14	0.175	5.7143	M7	2550
-211377	0.174	5.7471	M1	3370
4.4048	0.173	5.7803	M4	2950

VB10	0.173	5.7803	M5	2800

Star Name	Parallax (arcsecs)	Distance (parsecs)	Star Type	Surface Temperature (K)
Eta Cas 4614 b	0.17	5.8824	M0	3480
-31123	0.17	5.8824	M1	3370
-40.9712	0.169	5.9172	M4	2950
Ross 986	0.169	5.9172	M5	2800
Wolf 294	0.168	5.9524	M4	2950
Ross 47	0.168	5.9524	M6	2700
53.132	0.166	6.0241	M0	3480
53.1321	0.166	6.0241	M0	3480
YZCMi	0.165	6.0606	M4	2950
-45.13677	0.164	6.0976	M0	3480
Wolf 629	0.161	6.2112	M4	2950
Wolf 630 a	0.161	6.2112	M4	2950
Wolf 630 b	0.161	6.2112	M5	2800
Wolf 630 - VB8	0.161	6.2112	M5	2800
-11.3759	0.16	6.2500	M4	2950
45.2505	0.155	6.4516	M3	3050
Fu 46	0.155	6.4516	M3	3050
19.5116 a	0.155	6.4516	M4	2950
19.5116 b	0.155	6.4516	M6	2700

A.2 COMP Model Codes

This appendix contains the input codes used to create the low and higher order optical models of the segmented reflector.

Low Order Model Input Code

```
ChfRayDir= 0.0000000000D+00 0.0000000000D+00-0.1000000000D+01
ChfRayPos= 0.0000000000D+00 0.0000000000D+00 0.1000000000D+02
 IndRef= 0.1000000000D+01
 Wavelen= 0.1000000000D-04
   Flux= 0.1000000000D+01
GridType= 3
Aperture= 0.3900000000D+01
Obscratn= 0.7800000000D+00
nGridpts= 15
  xGrid= 0.1000000000D+01 0.0000000000D+00 0.0000000000D+00
   nElt= 10
   nSeg= 7
  width= 0.1300000000D+01
   gap= 0.0000000000D+00
SegCoord=  0     0     0
           1    -1    -2
           2     1    -1
           1     2     1
          -1     1     2
          -2    -1     1
          -1    -2    -1
   iElt= 1
 EltName= SEG1
 EltType= 5
   fElt= 0.7800000000D+01
   eElt= 0.1000000000D+01
 psiElt= 0.0000000000D+00 0.0000000000D+00 0.1000000000D+01
 VptElt= 0.0000000000D+00 0.0000000000D+00 0.0000000000D+00
 RptElt= 0.0000000000D+00 0.0000000000D+00 0.0000000000D+00
 IndRef= 0.1000000000D+01
   zElt= 0.0000000000E+00
PropType= 1
 nECoord= -6
   iElt= 2
 EltName= SEG2
 EltType= 5
   fElt= 0.7800000000D+01
   eElt= 0.1000000000D+01
 psiElt= 0.0000000000D+00 0.0000000000D+00 0.1000000000D+01
 VptElt= 0.0000000000D+00 0.0000000000D+00 0.0000000000D+00
 RptElt= 0.6500000000D+00-0.1125833000D+01 0.5416600000D-01
 IndRef= 0.1000000000D+01
   zElt= 0.0000000000E+00
PropType= 1
 nECoord= -6
   iElt= 3
```

```
 EltName= SEG3
 EltType=   5
   fElt=  0.7800000000D+01
   eElt=  0.1000000000D+01
  psiElt=  0.0000000000D+00 0.0000000000D+00 0.1000000000D+01
  VptElt=  0.0000000000D+00 0.0000000000D+00 0.0000000000D+00
  RptElt=  0.1300000000D+01 0.0000000000D+00 0.5416600000D-01
  IndRef=  0.1000000000D+01
   zElt=  0.0000000000E+00
PropType=   1
 nECoord=  -6
   iElt=   4
 EltName= SEG4
 EltType=   5
   fElt=  0.7800000000D+01
   eElt=  0.1000000000D+01
  psiElt=  0.0000000000D+00 0.0000000000D+00 0.1000000000D+01
  VptElt=  0.0000000000D+00 0.0000000000D+00 0.0000000000D+00
  RptElt=  0.6500000000D+00 0.1125833000D+01 0.5416600000D-01
  IndRef=  0.1000000000D+01
   zElt=  0.0000000000E+00
PropType=   1
 nECoord=  -6
   iElt=   5
 EltName= SEG5
 EltType=   5
   fElt=  0.7800000000D+01
   eElt=  0.1000000000D+01
  psiElt=  0.0000000000D+00 0.0000000000D+00 0.1000000000D+01
  VptElt=  0.0000000000D+00 0.0000000000D+00 0.0000000000D+00
  RptElt= -0.6500000000D+00 0.1125833000D+01 0.5416600000D-01
  IndRef=  0.1000000000D+01
   zElt=  0.0000000000E+00
PropType=   1
 nECoord=  -6
   iElt=   6
 EltName= SEG6
 EltType=   5
   fElt=  0.7800000000D+01
   eElt=  0.1000000000D+01
  psiElt=  0.0000000000D+00 0.0000000000D+00 0.1000000000D+01
  VptElt=  0.0000000000D+00 0.0000000000D+00 0.0000000000D+00
  RptElt= -0.1300000000D+01 0.0000000000D+00 0.5416600000D-01
  IndRef=  0.1000000000D+01
   zElt=  0.0000000000E+00
PropType=   1
 nECoord=  -6
   iElt=   7
 EltName= SEG7
 EltType=   5
   fElt=  0.7800000000D+01
   eElt=  0.1000000000D+01
  psiElt=  0.0000000000D+00 0.0000000000D+00 0.1000000000D+01
  VptElt=  0.0000000000D+00 0.0000000000D+00 0.0000000000D+00
  RptElt= -0.6500000000D+00-0.1125833000D+01 0.5416600000D-01
  IndRef=  0.1000000000D+01
   zElt=  0.0000000000E+00
PropType=   1
```

```
nECoord=  -6
  iElt=   8
EltName= SEC
EltType=   1
  fElt=  0.1560000000D+01
  eElt=  1.5714285714
 psiElt=  0.0000000000D+00 0.0000000000D+00 0.1000000000D+01
 VptElt=  0.0000000000D+00 0.0000000000D+00 0.6240000000D+01
 RptElt=  0.0000000000D+00 0.0000000000D+00 0.6240000000D+01
 IndRef=  0.1000000000D+01
  zElt=  0.0000000000E+00
PropType=   1
nECoord=   0
  iElt=   9
EltName= REFSURF
EltType=   4
  fElt=  0.6920000000D+01
  eElt=  0.0000000000D+00
 psiElt=  0.0000000000D+00 0.0000000000D+00-0.1000000000D+01
 VptElt=  0.0000000000D+00 0.0000000000D+00 0.6140000000D+01
 RptElt=  0.0000000000D+00 0.0000000000D+00 0.6140000000D+01
 IndRef=  0.1000000000D+01
  zElt=  0.6920000000E+01
PropType=   3
nECoord=   0
  iElt=   10
EltName= FOCPLANE
EltType=   3
  fElt=  0.1000000000D+19
  eElt=  0.0000000000D+00
 psiElt=  0.0000000000D+00 0.0000000000D+00 0.1000000000D+01
 VptElt=  0.0000000000D+00 0.0000000000D+00-0.0780000000D+01
 RptElt=  0.0000000000D+00 0.0000000000D+00-0.0780000000D+01
 IndRef=  0.1000000000D+01
  zElt=  0.0000000000E+00
PropType=   1
nECoord=   0
nOutCord=   5
   Tout=  1.0000D+00 0.0000D+00 0.0000D+00 0.0000D+00 0.0000D+00 0.0000D+00 0.0000D+01
          0.0000D+00 1.0000D+00 0.0000D+00 0.0000D+00 0.0000D+00 0.0000D+00 0.0000D+01
          0.0000D+00 0.0000D+00 0.0000D+00 1.0000D+00 0.0000D+00 0.0000D+00 0.0000D+01
          0.0000D+00 0.0000D+00 0.0000D+00 0.0000D+00 1.0000D+00 0.0000D+00 0.0000D+01
          0.0000D+00 0.0000D+00 0.0000D+00 0.0000D+00 0.0000D+00 0.0000D+00 0.1000D+01
```

Higher Order Model Input Code

```
ChfRayDir= 0.0000000000D+00 0.0000000000D+00-0.1000000000D+01
ChfRayPos= 0.0000000000D+00 0.0000000000D+00 0.1000000000D+02
 zSource= 0.1000000000D+20
  IndRef= 0.1000000000D+01
 Wavelen= 0.1000000000D-04
    Flux= 0.1000000000D+01
GridType=    3
Aperture= 0.3900000000D+01
Obscratn= 0.1300000000D+01
nGridpts=   32
   xGrid= 0.1000000000D+01 0.0000000000D+00 0.0000000000D+00
    nElt=   10
    nSeg=    7
   width= 0.1300000000D+01
     gap= 0.0000000000D+00
SegCoord=      0          0          0
               1         -1         -2
               2          1         -1
               1          2          1
              -1          1          2
              -2         -1          1
              -1         -2         -1
    iElt=    1
 EltName= s1
 EltType=   15
   KrElt= -0.1560000000D+02
   KcElt= -0.1000000000D+01
ZernCoef= 0.0000000000D+00 0.0000000000D+00 0.0000000000D+00 0.0000000000D+00 0.0(
          0.0000000000D+00 0.0000000000D+00 0.0000000000D+00 0.0000000000D+00 0.0(
          0.0000000000D+00 0.0000000000D+00 0.0000000000D+00 0.0000000000D+00 0.0(
          0.0000000000D+00 0.0000000000D+00 0.0000000000D+00 0.0000000000D+00 0.0(
          0.0000000000D+00 0.0000000000D+00 0.0000000000D+00 0.0000000000D+00 0.0(
          0.0000000000D+00 0.0000000000D+00 0.0000000000D+00 0.0000000000D+00 0.0(
    pMon= 0.0000000000D+00-0.0000000000D+00 0.0000000000D+00
    xMon=-0.0000000000D+00-1.0000000000D+00 0.0000000000D+00
    yMon= 0.0000000000D+00 1.0000000000D+00 0.0000000000D+00
    zMon= 0.0000000000D-00 0.0000000000D-00 1.0000000000D+00
    lMon= 0.7505500000D+00
 psiElt= 0.0000000000D+00 0.0000000000D+00 0.1000000000D+01
 VptElt= 0.0000000000D+00 0.0000000000D+00 0.0000000000D+00
 RptElt= 0.0000000000D+00 0.0000000000D+00 0.0000000000D+00
  IndRef= 0.1000000000D+01
    zElt= 0.0000000000E+00
PropType=    1
 nECoord=    0
    iElt=    2
 EltName= s2
 EltType=   15
   KrElt= -0.1560000000D+02
   KcElt= -0.1000000000D+01
ZernCoef= 0.0000000000D+00 0.0000000000D+00 0.0000000000D+00 0.0000000000D+00 0.0(
          0.0000000000D+00 0.0000000000D+00 0.0000000000D+00 0.0000000000D+00 0.0(
          0.0000000000D+00 0.0000000000D+00 0.0000000000D+00 0.0000000000D+00 0.0(
          0.0000000000D+00 0.0000000000D+00 0.0000000000D+00 0.0000000000D+00 0.0(
          0.0000000000D+00 0.0000000000D+00 0.0000000000D+00 0.0000000000D+00 0.0(
          0.0000000000D+00 0.0000000000D+00 0.0000000000D+00 0.0000000000D+00 0.0(
    pMon= 0.6500000000D+00-0.1125833300D+01 0.5416660000D-01
    xMon=-0.8660265528D+00-0.4999980098D+00 0.0000000000D+00
    yMon= 0.4982711058D+00-0.8630354515D+00 0.8304043948D-01
    zMon=-0.4152005447D-01 0.7191522555D-01 0.9965461783D+00
    lMon= 0.7505500000D+00
 psiElt= 0.0000000000D+00 0.0000000000D+00 0.1000000000D+01
 VptElt= 0.0000000000D+00 0.0000000000D+00 0.0000000000D+00
 RptElt= 0.6500000000D+00-0.1125833300D+01 0.5416660000D-01
  IndRef= 0.1000000000D+01
```

```
    zElt=  0.0000000000E+00
PropType=    1
 nECoord=   -6   <-- 6 DoF's
    iElt=    3
 EltName= s3
 EltType=   15
   KrElt= -0.1560000000D+02
   KcElt= -0.1000000000D+01
ZernCoef=  0.0000000000D+00 0.0000000000D+00 0.0000000000D+00 0.0000000000D
           0.0000000000D+00 0.0000000000D+00 0.0000000000D+00 0.0000000000D
           0.0000000000D+00 0.0000000000D+00 0.0000000000D+00 0.0000000000D
           0.0000000000D+00 0.0000000000D+00 0.0000000000D+00 0.0000000000D
           0.0000000000D+00 0.0000000000D+00 0.0000000000D+00 0.0000000000D
           0.0000000000D+00 0.0000000000D+00 0.0000000000D+00 0.0000000000D
    pMon=  0.1300000000D+01 0.0000000000D+00 0.5416660000D-01
    xMon=  0.0000000000D+00-0.1000000000D+01 0.0000000000D+00
    yMon=  0.9965462134D+00 0.0000000000D+00 0.8304001778D-01
    zMon= -0.8304001778D-01 0.0000000000D+00 0.9965462134D+00
    lMon=  0.7505500000D+00
  psiElt=  0.0000000000D+00 0.0000000000D+00 0.1000000000D+01
  VptElt=  0.0000000000D+00 0.0000000000D+00 0.0000000000D+00
  RptElt=  0.1300000000D+01 0.0000000000D+00 0.5416660000D-01   <-- Cen
  IndRef=  0.1000000000D+01                                        f
    zElt=  0.0000000000E+00
PropType=    1
 nECoord=   -6
    iElt=    4
 EltName= s4
 EltType=   15
   KrElt= -0.1560000000D+02
   KcElt= -0.1000000000D+01   <-- Ke = -e^2
/ZernCoef=  0.0000000000D+00 0.0000000000D+00 0.0000000000D+00 0.000000000(
           0.0000000000D+00 0.0000000000D+00 0.0000000000D+00 0.000000000(
           0.0000000000D+00 0.0000000000D+00 0.0000000000D+00 0.000000000(
           0.0000000000D+00 0.0000000000D+00 0.0000000000D+00 0.000000000(
           0.0000000000D+00 0.0000000000D+00 0.0000000000D+00 0.000000000(
           0.0000000000D+00 0.0000000000D+00 0.0000000000D+00 0.000000000
    pMon=  0.6500000000D+00 0.1125833300D+01 0.5416660000D-01
    xMon=  0.8660265528D+00-0.4999980098D+00 0.0000000000D+00
    yMon=  0.4982711058D+00 0.8630354515D+00 0.8304043948D-01
    zMon= -0.4152005447D-01-0.7191522555D-01 0.9965461783D+00
    lMon=  0.7505500000D+00
  psiElt=  0.0000000000D+00 0.0000000000D+00 0.1000000000D+01
  VptElt=  0.0000000000D+00 0.0000000000D+00 0.0000000000D+00
  RptElt=  0.6500000000D+00 0.1125833300D+01 0.5416660000D-01
  IndRef=  0.1000000000D+01
    zElt=  0.0000000000E+00
PropType=    1
 nECoord=   -6
    iElt=    5
 EltName= s5
 EltType=   15
   KrElt= -1.5600000000D+02
   KcElt= -0.1000000000D+01
ZernCoef=  0.0000000000D+00 0.0000000000D+00 0.0000000000D+00 0.000000000
           0.0000000000D+00 0.0000000000D+00 0.0000000000D+00 0.000000000(
           0.0000000000D+00 0.0000000000D+00 0.0000000000D+00 0.000000000(
           0.0000000000D+00 0.0000000000D+00 0.0000000000D+00 0.000000000(
           0.0000000000D+00 0.0000000000D+00 0.0000000000D+00 0.000000000(
           0.0000000000D+00 0.0000000000D+00 0.0000000000D+00 0.000000000(
    pMon= -0.6500000000D+00 0.1125833300D+01 0.5416660000D-01
    xMon=  0.8660265528D+00 0.4999980098D+00 0.0000000000D+00
    yMon= -0.4982711058D+00 0.8630354515D+00 0.8304043948D-01
    zMon=  0.4152005447D-01-0.7191522555D-01 0.9965461783D+00
    lMon=  0.7505500000D+00
  psiElt=  0.0000000000D+00 0.0000000000D+00 0.1000000000D+01
  VptElt=  0.0000000000D+00 0.0000000000D+00 0.0000000000D+00
  RptElt= -0.6500000000D+00 0.1125833300D+01 0.5416660000D-01
  IndRef=  0.1000000000D+01
    zElt=  0.0000000000E+00
PropType=    1
 nECoord=   -6
    iElt=    6
 EltName= s6
 EltType=   15
   KrElt= -0.1560000000D+02
   KcElt= -0.1000000000D+01
ZernCoef=  0.0000000000D+00 0.0000000000D+00 0.0000000000D+00 0.0000000000D+00 0.0(
           0.0000000000D+00 0.0000000000D+00 0.0000000000D+00 0.0000000000D+00 0.0(
           0.0000000000D+00 0.0000000000D+00 0.0000000000D+00 0.0000000000D+00 0.0(
           0.0000000000D+00 0.0000000000D+00 0.0000000000D+00 0.0000000000D+00 0.0(
           0.0000000000D+00 0.0000000000D+00 0.0000000000D+00 0.0000000000D+00 0.0(
           0.0000000000D+00 0.0000000000D+00 0.0000000000D+00 0.0000000000D+00 0.0(
    pMon= -0.1300000000D+01 0.0000000000D+00 0.5416660000D-01
```

```
    xMon=  0.0000000000D+00 0.1000000000D+01 0.0000000000D+00
    yMon= -0.9965462134D+00 0.0000000000D+00 0.8304001778D-01
    zMon=  0.8304001778D-01 0.0000000000D+00 0.9965462134D+00
    lMon=  0.7505500000D+00
  psiElt=  0.0000000000D+00 0.0000000000D+00 0.1000000000D+01
  VptElt=  0.0000000000D+00 0.0000000000D+00 0.0000000000D+00
  RptElt= -0.1300000000D+01 0.0000000000D+00 0.5416660000D-01
  IndRef=  0.1000000000D+01
    zElt=  0.0000000000E+00
PropType=    1
 nECoord=   -6
    iElt=    7
 EltName= s7
 EltType=   15
   KrElt= -0.1560000000D+02
   KcElt= -0.1000000000D+01
ZernCoef=  0.0000000000D+00 0.0000000000D+00 0.0000000000D+00 0.0000000000D+00 0.0(
           0.0000000000D+00 0.0000000000D+00 0.0000000000D+00 0.0000000000D+00 0.0(
           0.0000000000D+00 0.0000000000D+00 0.0000000000D+00 0.0000000000D+00 0.0(
           0.0000000000D+00 0.0000000000D+00 0.0000000000D+00 0.0000000000D+00 0.0(
           0.0000000000D+00 0.0000000000D+00 0.0000000000D+00 0.0000000000D+00 0.0(
           0.0000000000D+00 0.0000000000D+00 0.0000000000D+00 0.0000000000D+00 0.0(
    pMon= -0.6500000000D+02-0.1125833300D+01 0.5416660000D-01
    xMon= -0.8660265528D+00 0.4999980098D+00 0.0000000000D+00
    yMon= -0.4982711058D+00-0.8630354515D+00 0.8304043948D-01
    zMon=  0.4152005447D-01 0.7191522555D-01 0.9965461783D+00
    lMon=  0.7505500000D+00
  psiElt=  0.0000000000D+00 0.0000000000D+00 0.1000000000D+01
  VptElt=  0.0000000000D+00 0.0000000000D+00 0.0000000000D+00
  RptElt= -0.6500000000D+00-0.1125833300D+01 0.5416660000D-01
  IndRef=  0.1000000000D+01
    zElt=  0.0000000000E+00
PropType=    1
 nECoord=   -6

    iElt=    8
 EltName= sec  ← secondary
 EltType=    1
   KrElt=  0.1560000000D+01
   KcElt=  0.1571428571D+01
  psiElt=  0.0000000000D+00 0.0000000000D+00 0.1000000000D+01
  VptElt=  0.0000000000D+00 0.0000000000D+00 0.6240000000D+01
  RptElt=  0.0000000000D+00 0.0000000000D+00 0.6240000000D+01
  IndRef=  0.1000000000D+01
    zElt=  0.0000000000E+00
PropType=    1
 nECoord=    0
    iElt=    9
 EltName= refsurf  ← reference surface

 EltType=    4
   KrElt=  0.6920000000D+01  ← spherical
   KcElt=  0.0000000000D+00
  psiElt=  0.0000000000D+00 0.0000000000D+00-0.1000000000D+01
  VptElt=  0.0000000000D+00 0.0000000000D+00 0.6140000000D+01
  RptElt=  0.0000000000D+00 0.0000000000D+00 0.6140000000D+01
  IndRef=  0.1000000000D+01
    zElt=  0.6920000000E+01  ← scale length (important only ref sfc
PropType=    3  ← far-field
 nECoord=    0
    iElt=   10
 EltName= fplane  ← focal plane
 EltType=    3
   KrElt=  0.1000000000D+19
   KcElt=  0.0000000000D+00
  psiElt=  0.0000000000D+00 0.0000000000D+00 0.1000000000D+01
  VptElt=  0.0000000000D+00 0.0000000000D+00-0.7800000000D+00
  RptElt=  0.0000000000D+00 0.0000000000D+00-0.7800000000D+00
  IndRef=  0.1000000000D+01
    zElt=  0.0000000000E+00
PropType=    1
 nECoord=    0
nOutCord=    5
    Tout=  0.1000000000D+01 0.0000000000D+00 0.0000000000D+00 0.000000000(
           0.0000000000D+00 0.1000000000D+01 0.0000000000D+00 0.000000000(
           0.0000000000D+00 0.0000000000D+00 0.0000000000D+00 0.100000000(
           0.0000000000D+00 0.0000000000D+00 0.0000000000D+00 0.000000000(
           0.0000000000D+00 0.0000000000D+00 0.0000000000D+00 0.000000000(
```

5 output Coord's for Linear A
$(\theta_x, \theta_y, \delta_x, \delta_y, \delta L)$

A.3 Linear vs. Full Ray COMP

Several of the eigenvectors of the S-matrix were used in comparing the linear and full ray trace capabilities of COMP. Figures A3-1 below illustrates typical results. The linear ray trace method follows the full ray trace very closely, varying by 0.5% at most. For small perturbations ($z/\lambda \leq 0.1$), the Strehl ratio behavior is nearly quadratic. For larger errors, the Strehl ratio falls off to a minimum near 0.2, and then climbs again as the deformations refocus the rays at a slightly off-center point. However, strictly defined as the intensity ratio of aberrated/good images at the image plane center, the Strehl ratio could not climb, as the energy is redirected to a point other than the center. This climbing behavior is well modeled by a third order polynomial.

Wavefront error (WFE) was found to be directly proportional to perturbation magnitude for a given perturbation vector. Again, the linear ray trace method follows very closely to the full ray trace, varying less than 1% up to the maximum measured WFE of 35 $\mu m = 3.5\lambda$ (Fig. A3-2). These results indicate that, at least in the case of the optical system under examination, the linear approximations of optical performance are sufficient to characterize the system.

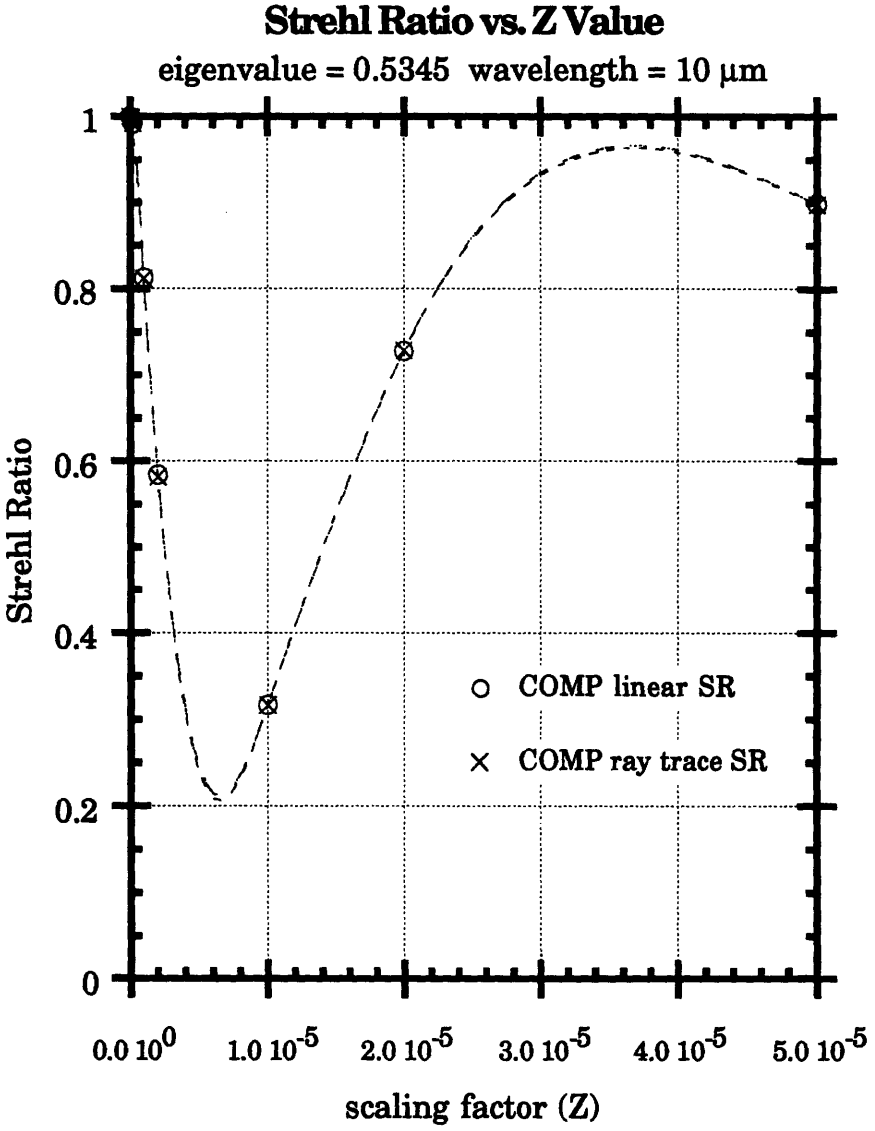

Figure A3-1
Strehl Ratio vs. Error Norm (linear & full ray)

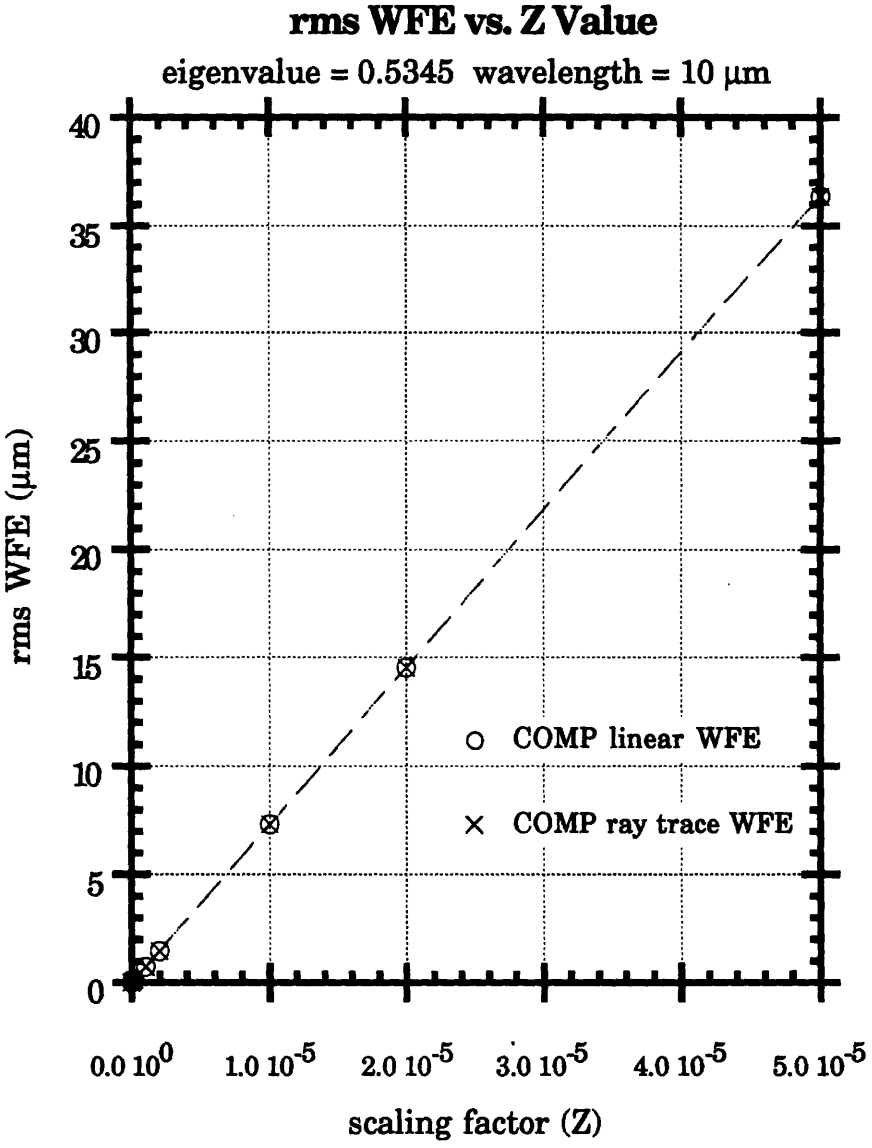

Figure A3-2
rms Wavefront Error vs. Error Norm

A.4 Zernike Polynomials

This appendix contains the polar forms for Zernike polynomials 2 through 36, as defined by Malacara. Z1 is not included as it is the pure piston term not being considered in this analysis. Each polynomial is accompanied with an orthographic projection of the polynomial described over the unit circle.

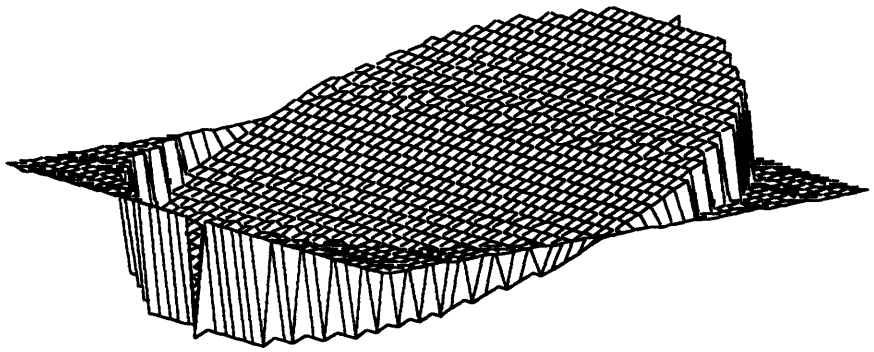

$Z2 = \rho\cos\theta$

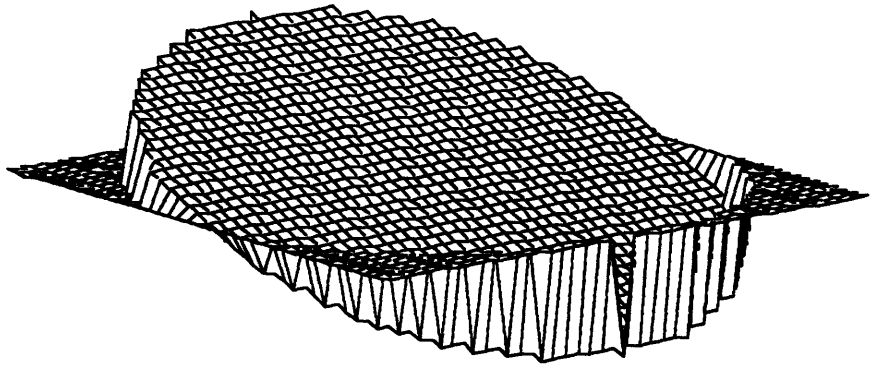

$Z3 = \rho\sin\theta$

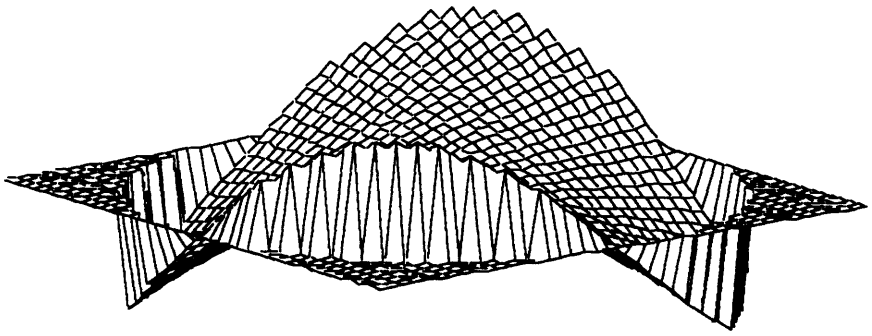

$Z4 = \rho^2 \sin 2\theta$

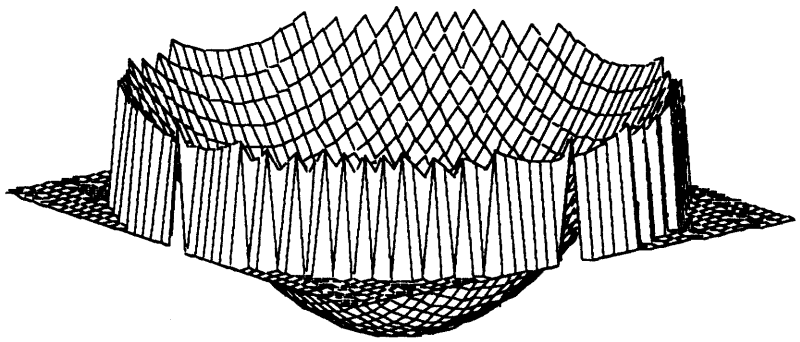

$Z5 = 2\rho^2 - 1$

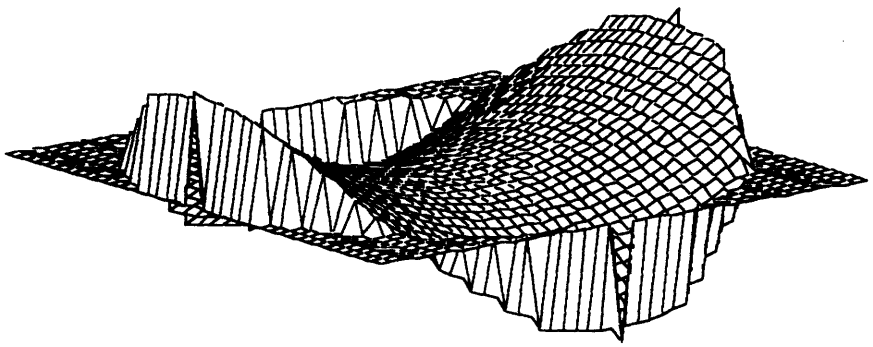

$Z6 = \rho^2 \cos 2\theta$

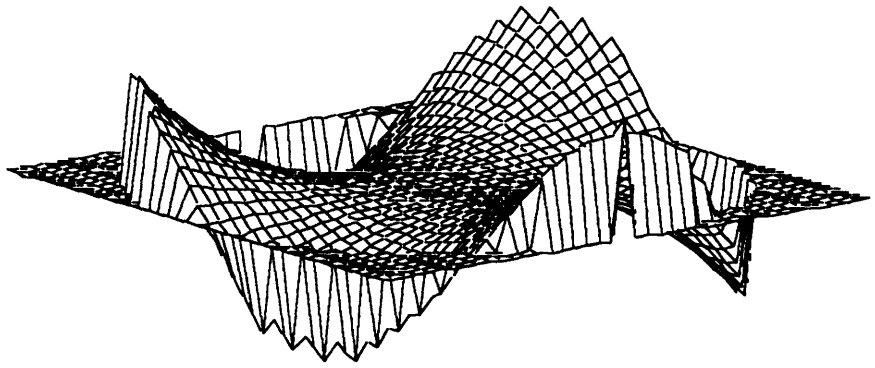

$Z7 = \rho^3 \cos 3\theta$

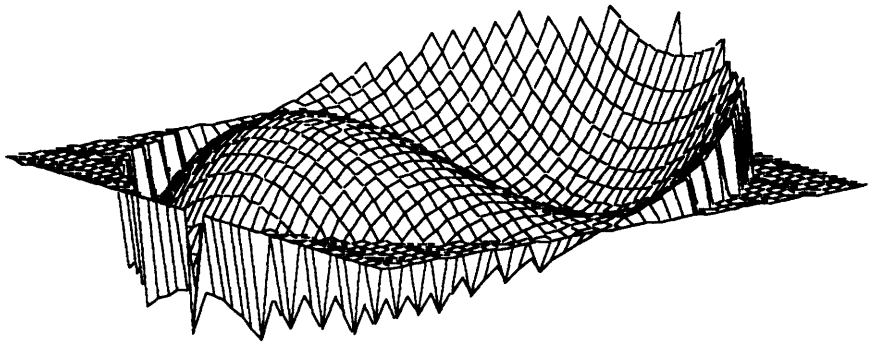

$Z8 = \rho(3\rho^2 - 2)\cos \theta$

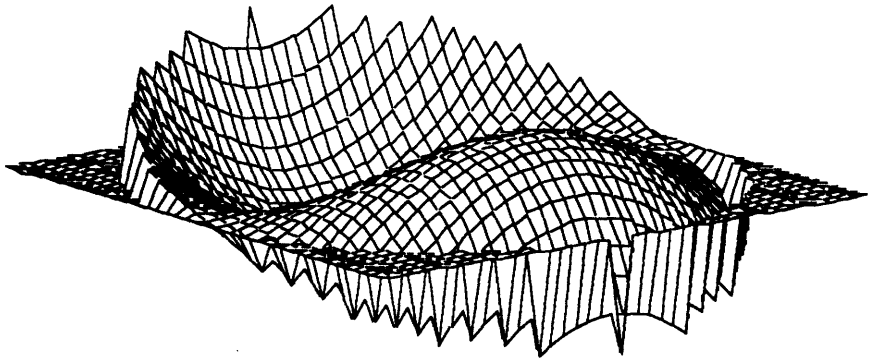

$Z9 = \rho(3\rho^2 - 2)\sin \theta$

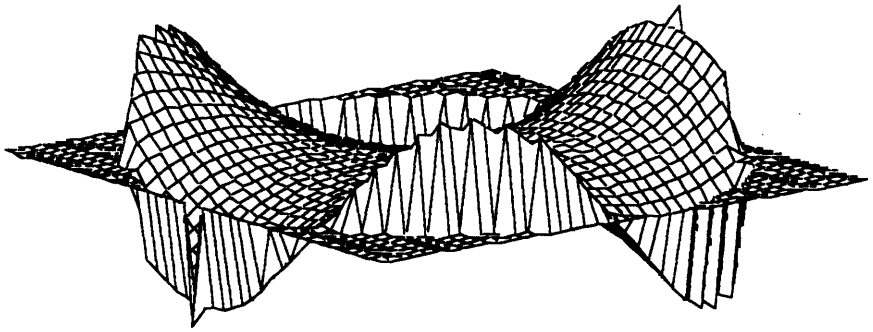

$Z10 = \rho^3 \sin 3\theta$

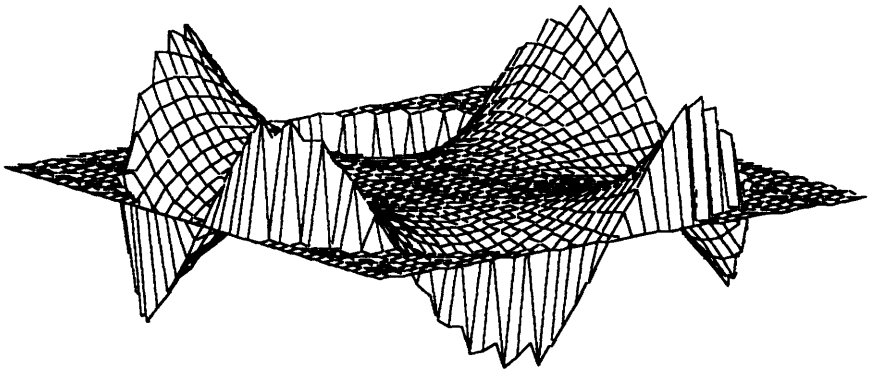

$Z11 = \rho^4 \sin 4\theta$

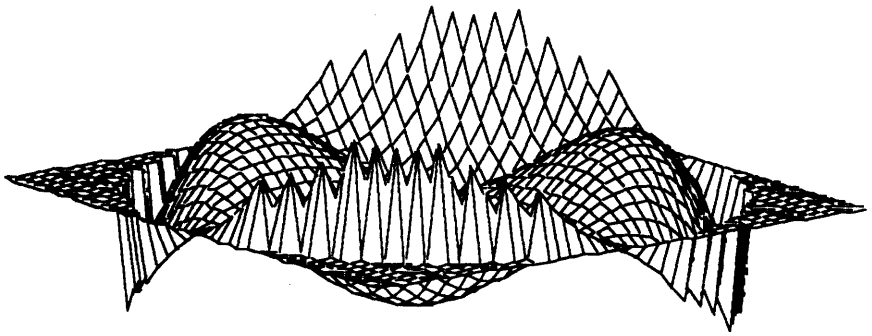

$Z12 = \rho^2(4\rho^2 - 3)\sin 2\theta$

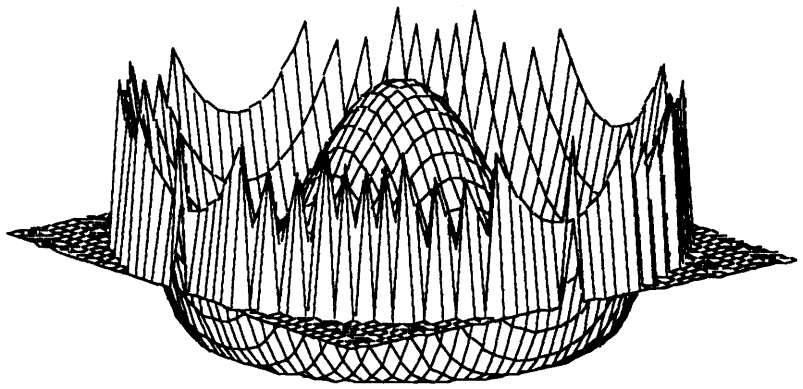

$Z13 = 6\rho^4 - 6\rho^2 + 1$

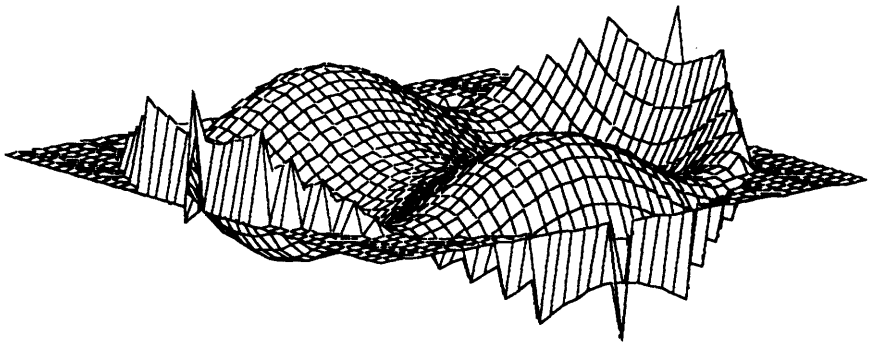

$Z14 = \rho^2(4\rho^2 - 3)\cos 2\theta$

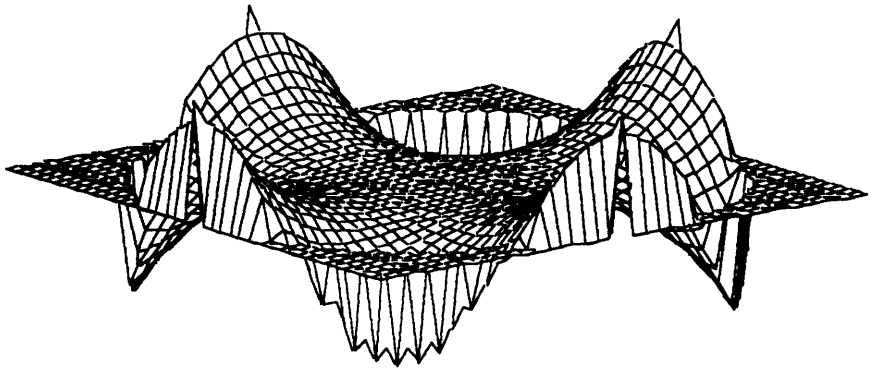

$Z15 = \rho^4 \cos 4\theta$

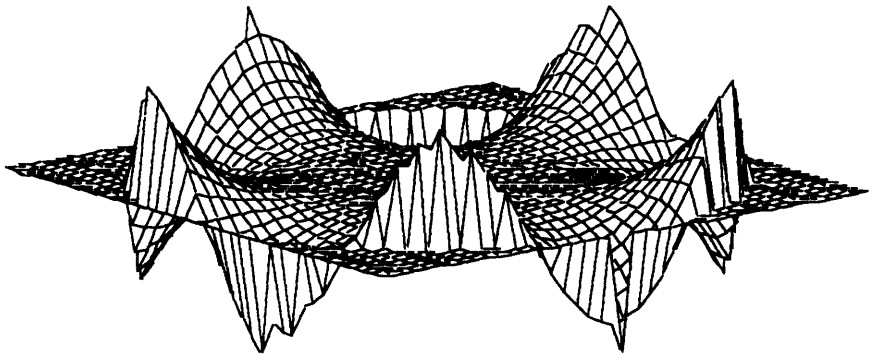

$Z16 = \rho^5 \sin 5\theta$

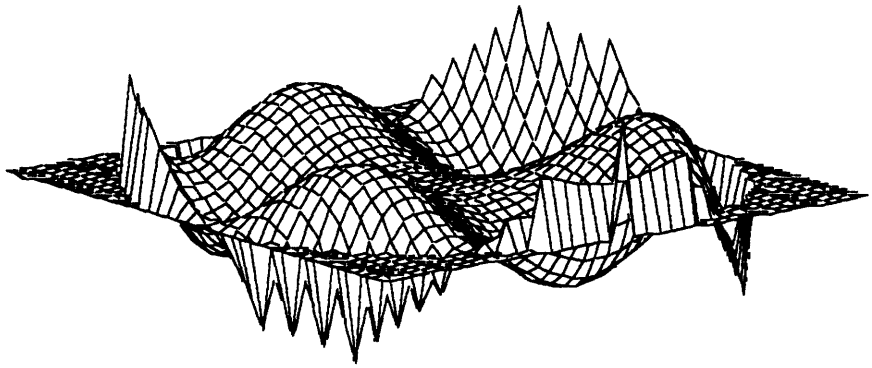

$Z17 = \rho^3(5\rho^2 - 4)\sin 3\theta$

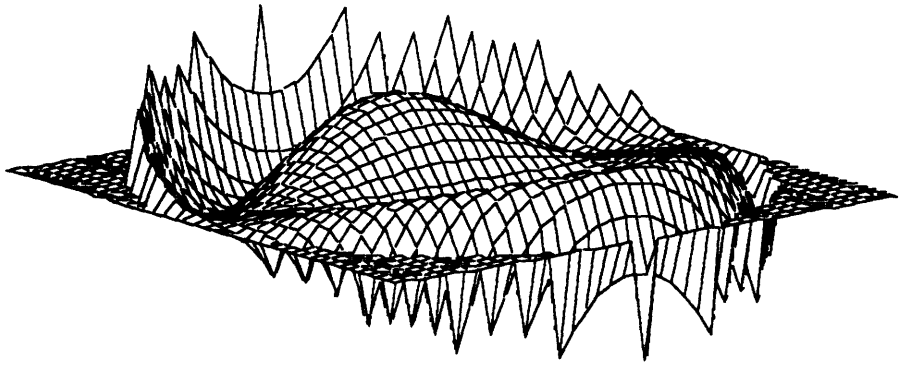

$Z18 = \rho(10\rho^4 - 12\rho^2 + 3)\sin \theta$

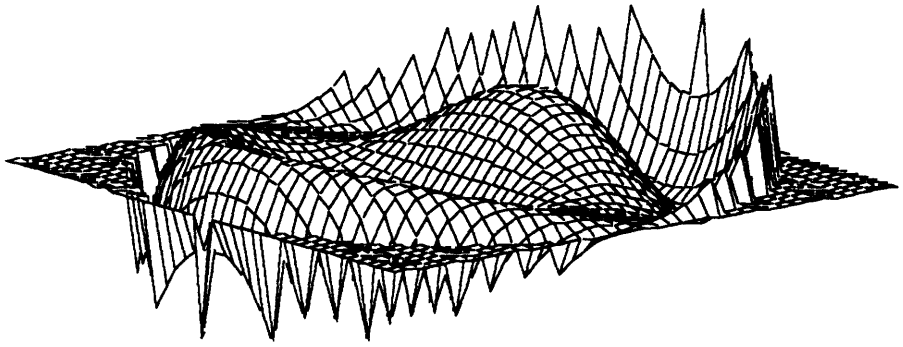

$$Z19 = \rho(10\rho^4 - 12\rho^2 + 3)\cos\theta$$

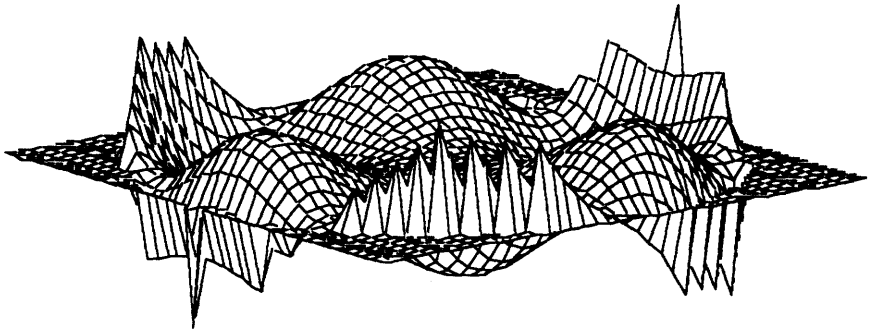

$$Z20 = \rho^3(5\rho^2 - 4)\cos 3\theta$$

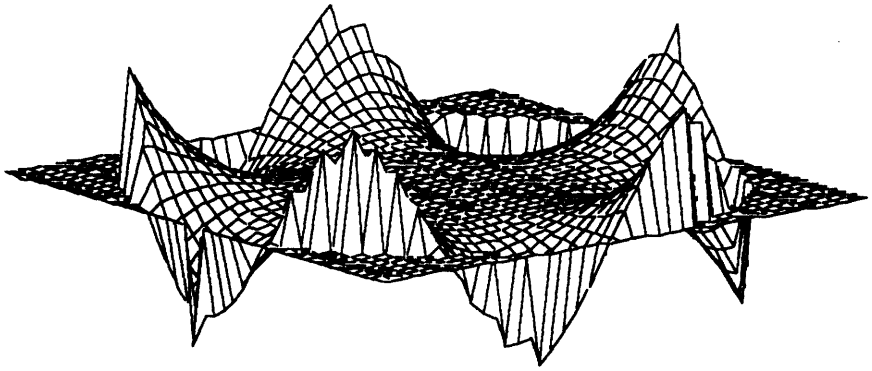

$$Z21 = \rho^5\cos 5\theta$$

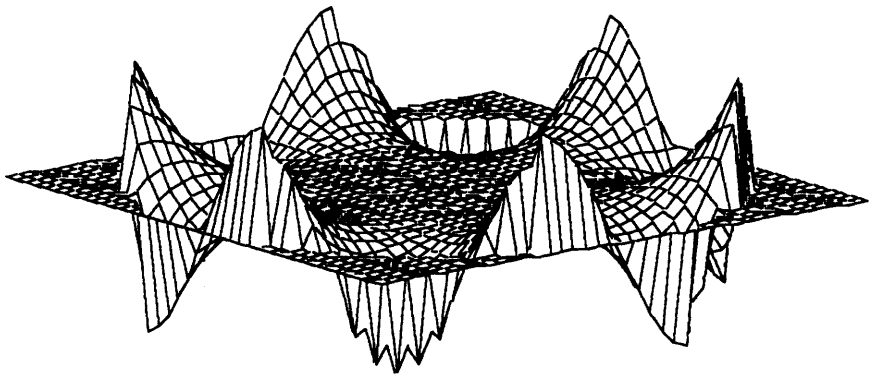

$Z22 = \rho^6 \sin 6\theta$

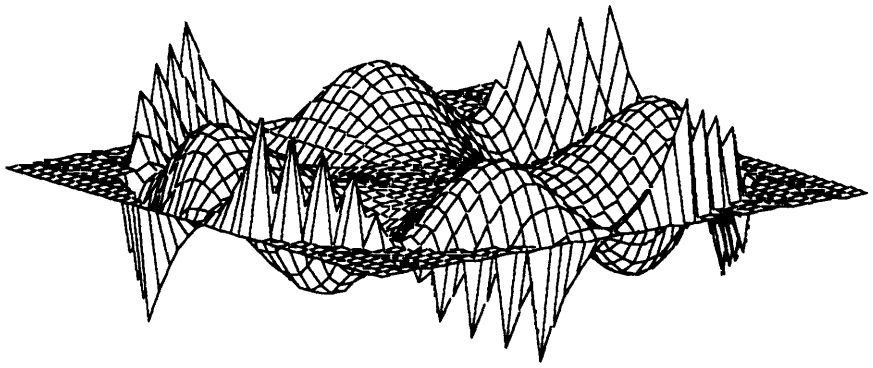

$Z23 = \rho^4(6\rho^2 - 5)\sin 4\theta$

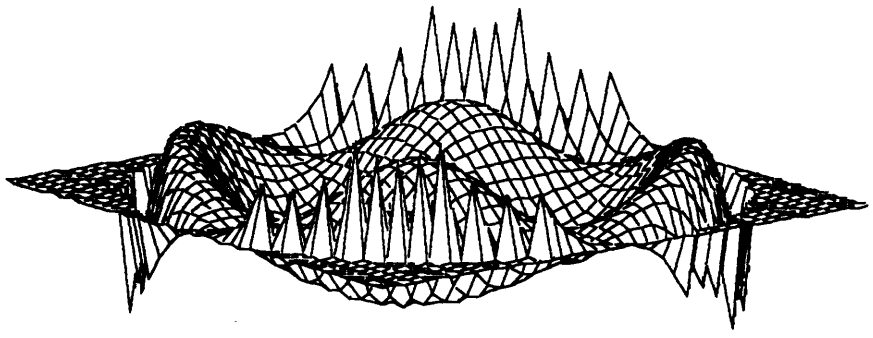

$Z24 = \rho^2(15\rho^4 - 20\rho^2 + 6)\sin 2\theta$

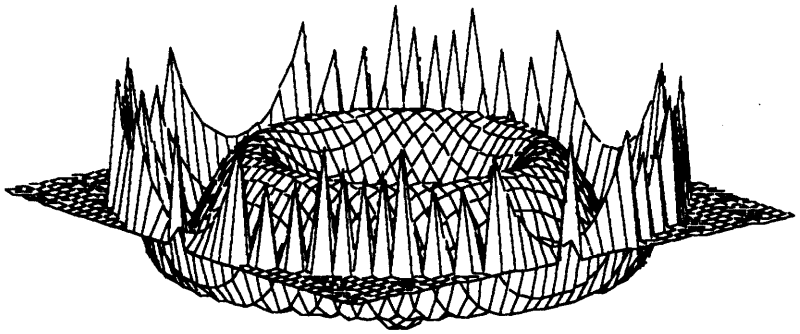

$$Z25 = 20\rho^6 - 30\rho^4 + 12\rho^2 - 1$$

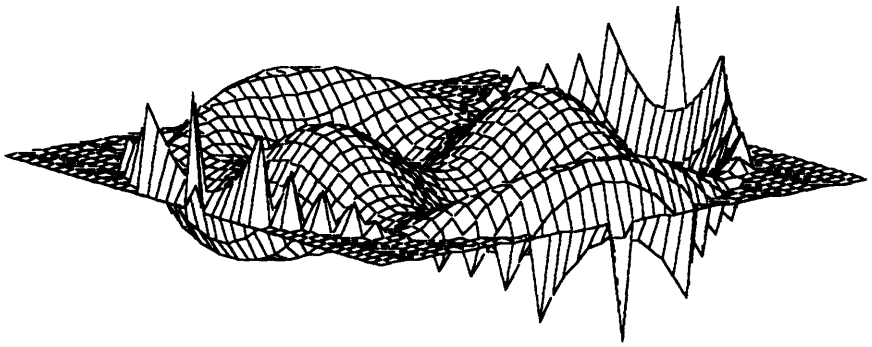

$$Z26 = \rho^2(15\rho^4 - 20\rho^2 + 6)\cos 2\theta$$

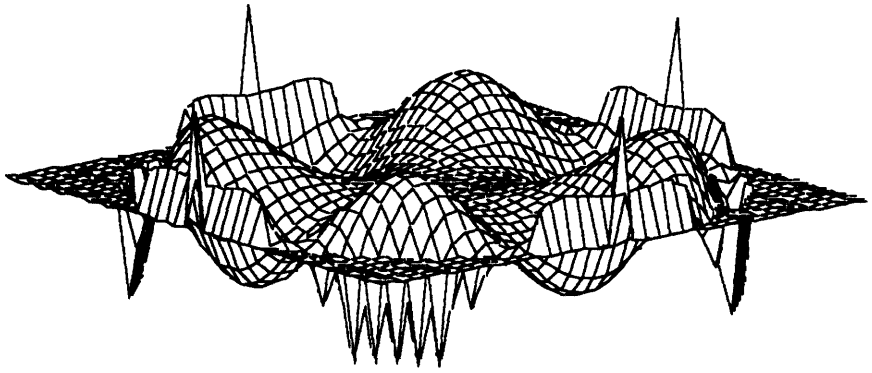

$$Z27 = \rho^4(6\rho^2 - 5)\cos 4\theta$$

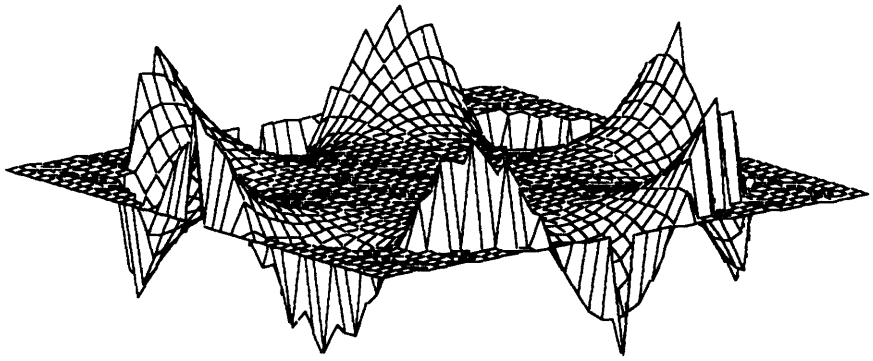

$Z28 = \rho^6 \cos 6\theta$

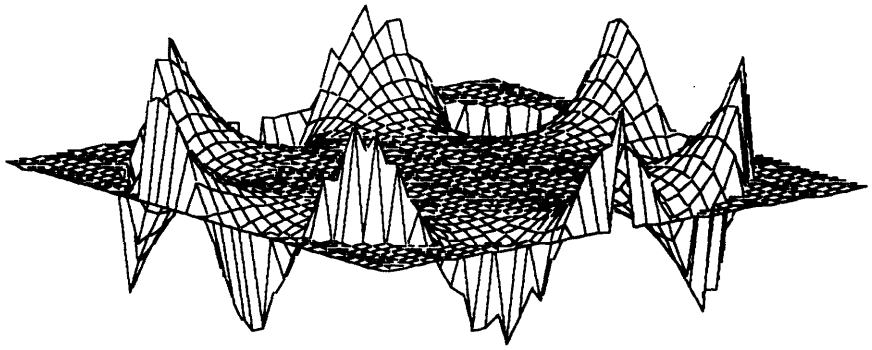

$Z29 = \rho^7 \sin 7\theta$

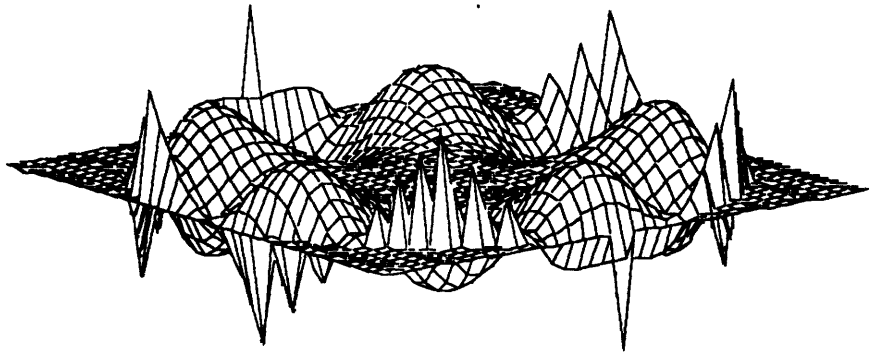

$Z30 = \rho^5(7\rho^2 - 6)\sin 5\theta$

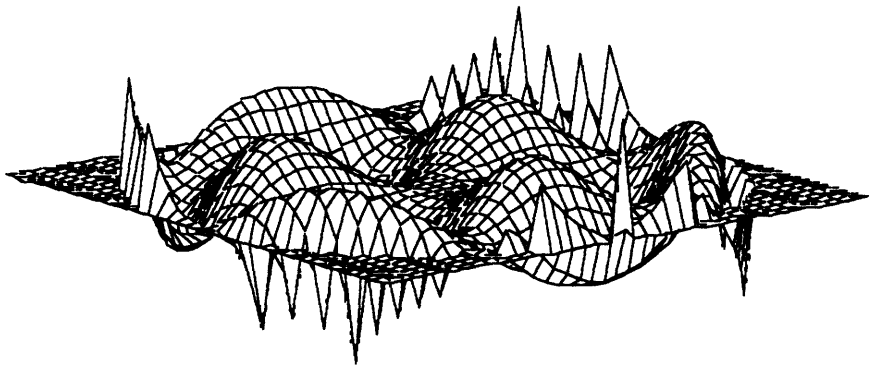

$$Z31 = \rho^3(21\rho^4 - 30\rho^2 + 10)\sin 3\theta$$

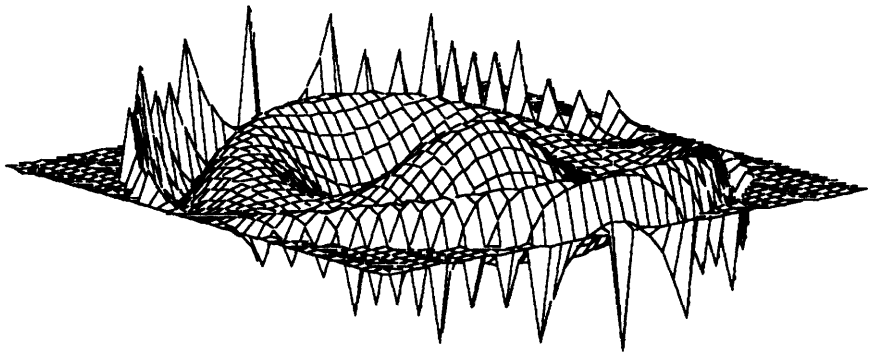

$$Z32 = \rho(35\rho^6 - 60\rho^4 + 30\rho^2 - 4)\sin \theta$$

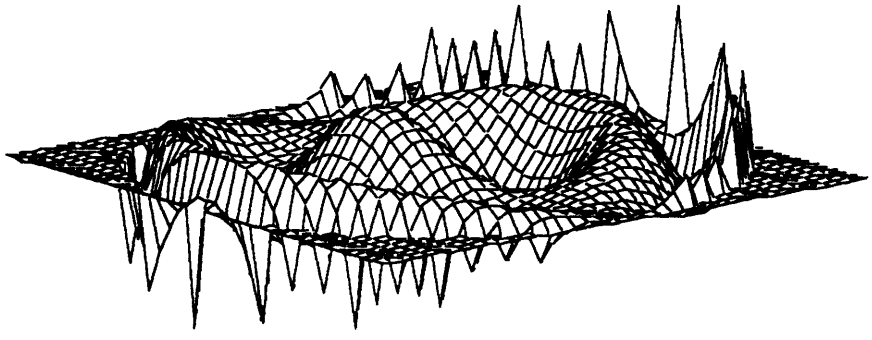

$$Z33 = \rho(35\rho^6 - 60\rho^4 + 30\rho^2 - 4)\cos \theta$$

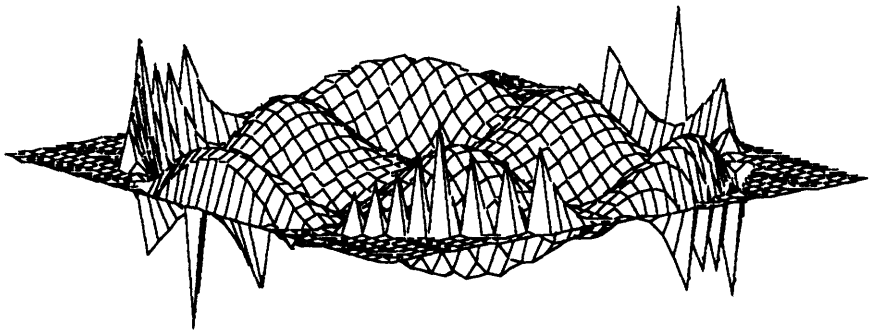

$Z34 = \rho^3(21\rho^4 - 30\rho^2 + 10)\cos 3\theta$

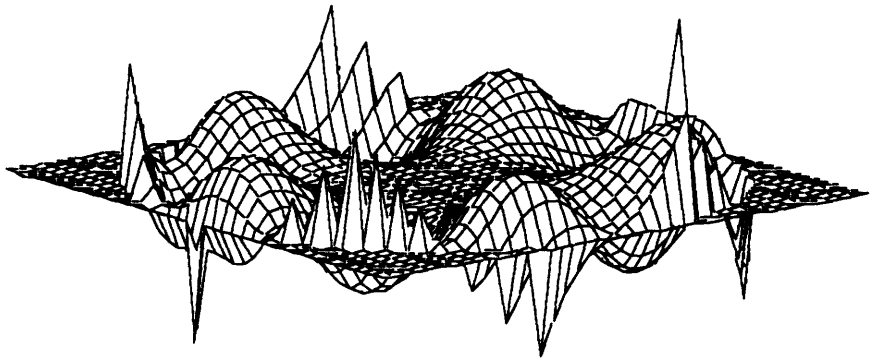

$Z35 = \rho^5(7\rho^2 - 6)\cos 5\theta$

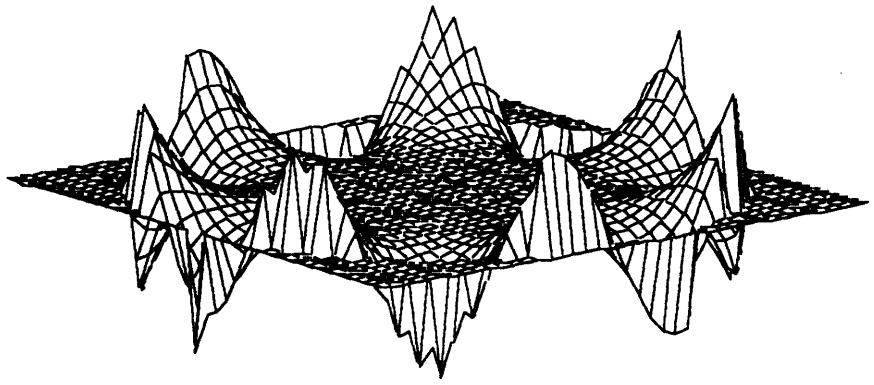

$Z36 = \rho^7 \cos 7\theta$

A.5 Actuator Group Deformations

This appendix contains the Zernike distribution plots and orthographic projections of the deformations produced by each of the 19 symmetric actuator groups described in Table 4-3. Group 2 is not shown, as it appears in the body of the report.

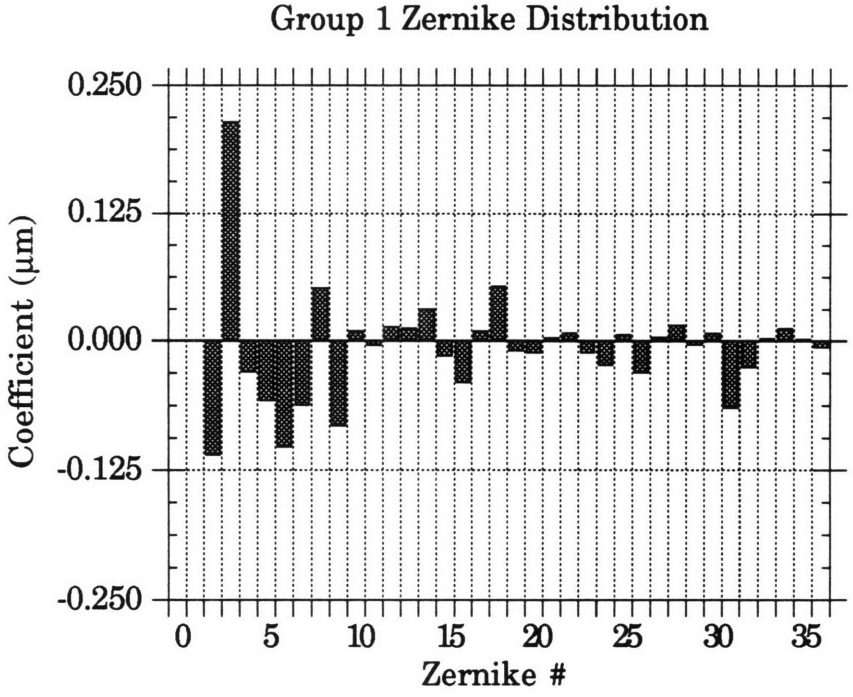

Group 1 Surface Deformation

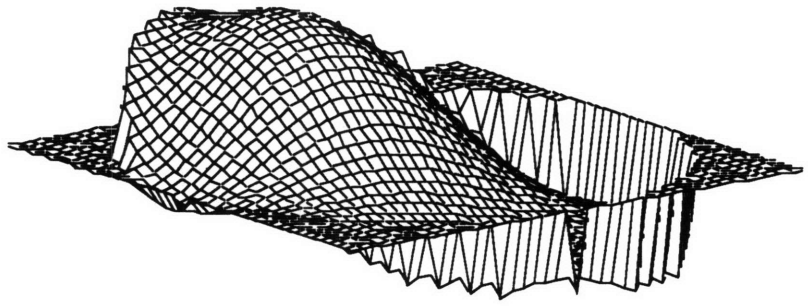

Group 3 Zernike Distribution

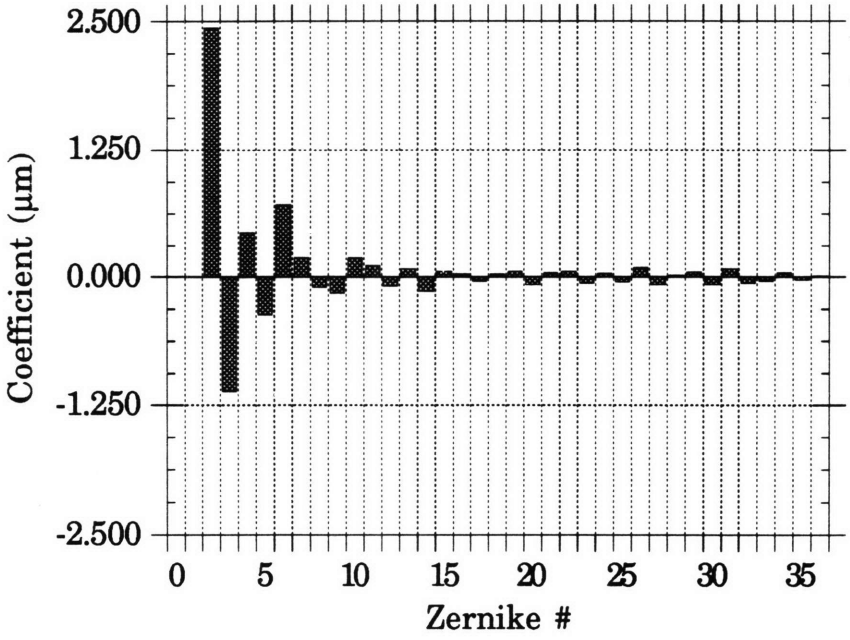

Group 3 Surface Deformation

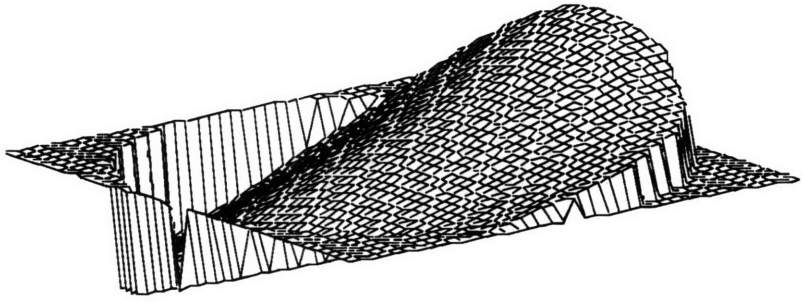

Group 4 Zernike Distribution

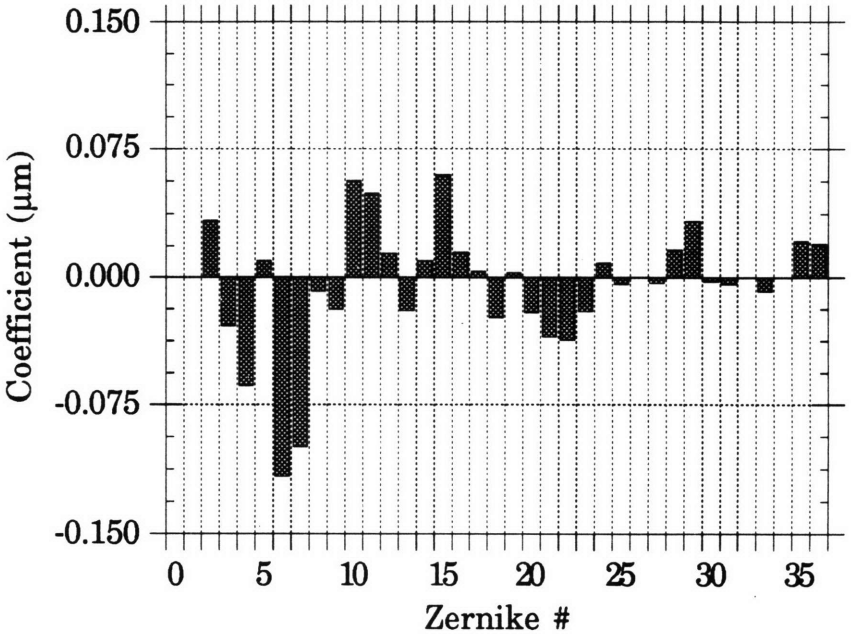

Group 4 Surface Deformation

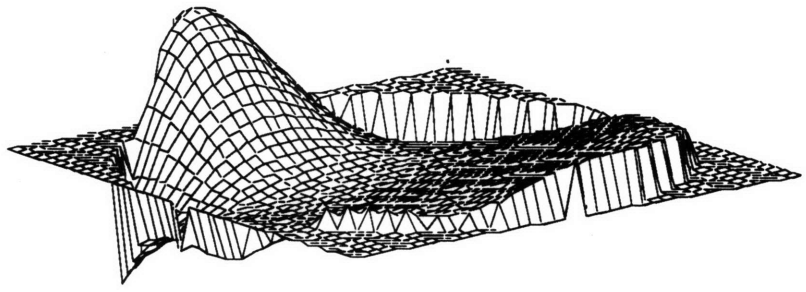

Group 5 Zernike Distribution

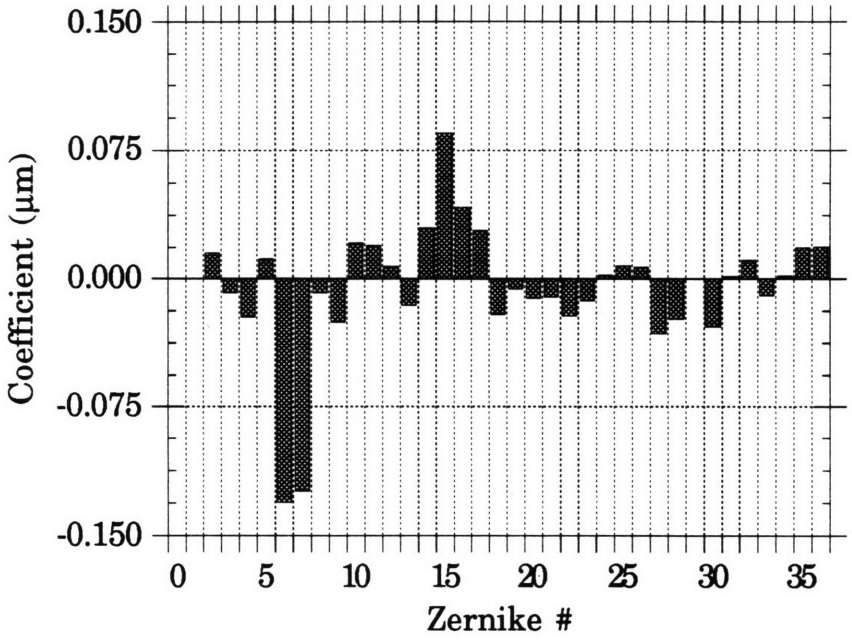

Group 5 Surface Deformation

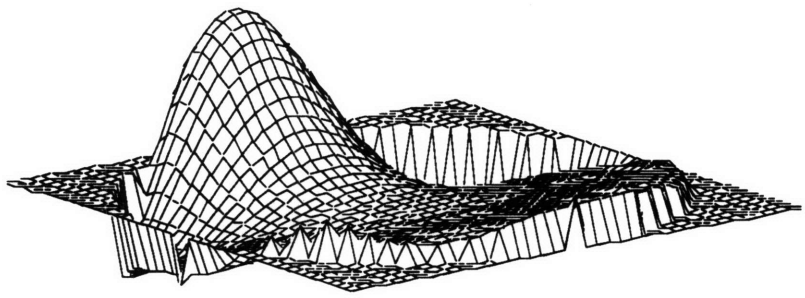

Group 6 Zernike Distribution

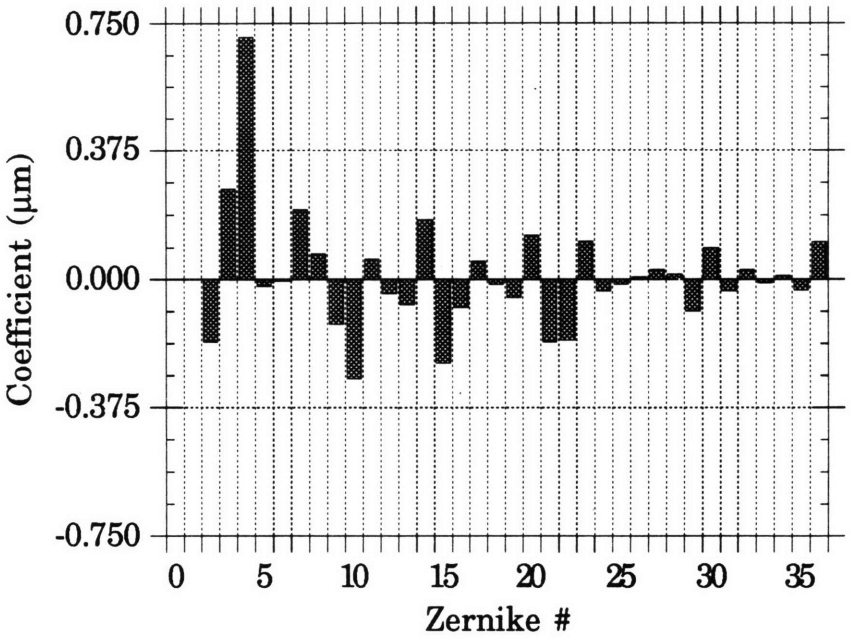

Group 6 Surface Deformation

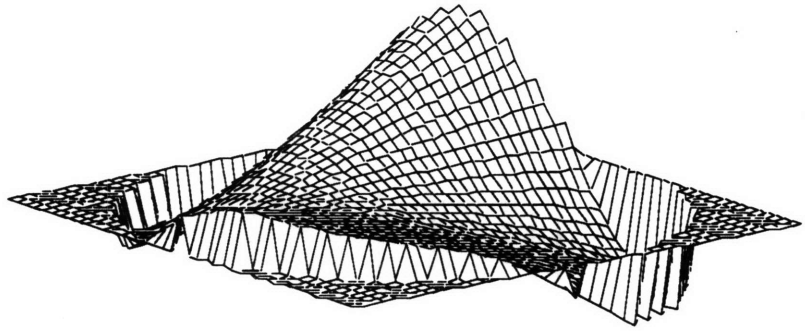

Group 7 Zernike Distribution

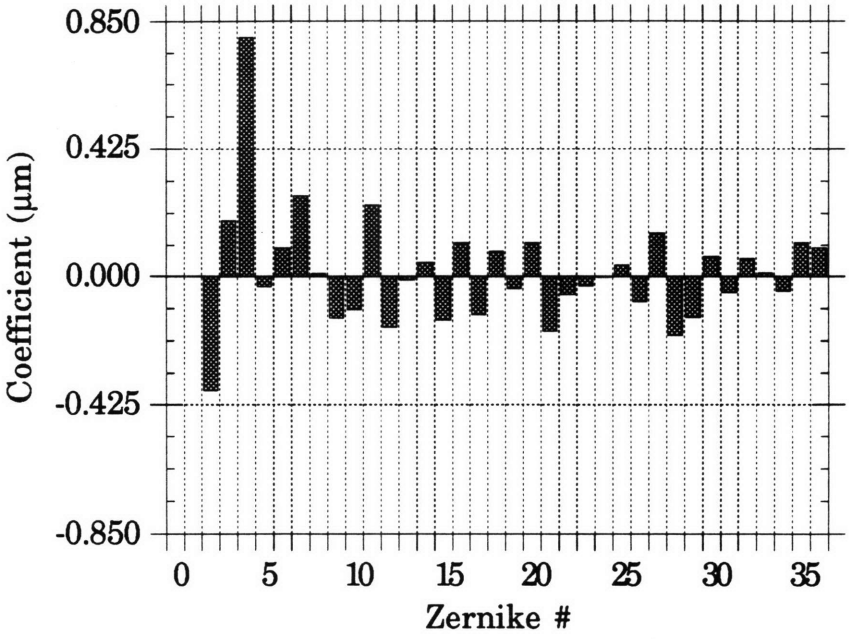

Group 7 Surface Deformation

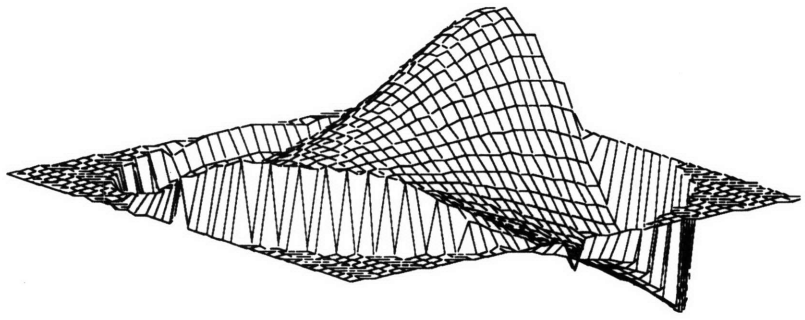

Group 8 Zernike Distribution

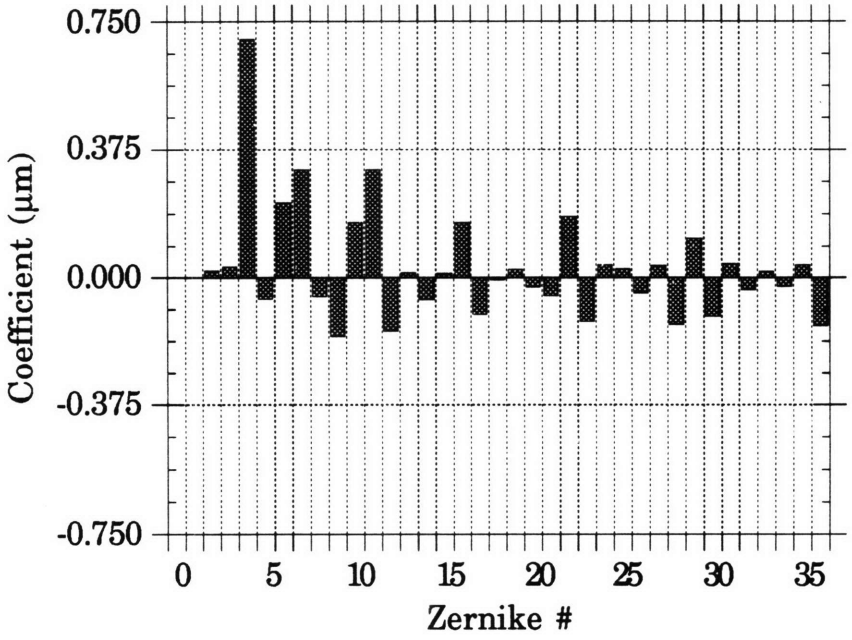

Group 8 Surface Deformation

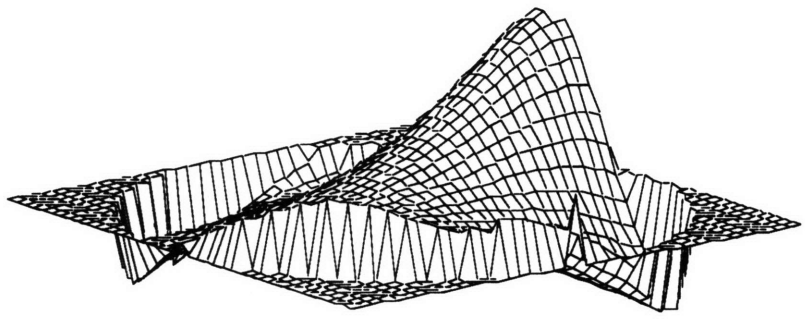

Group 9 Zernike Distribution

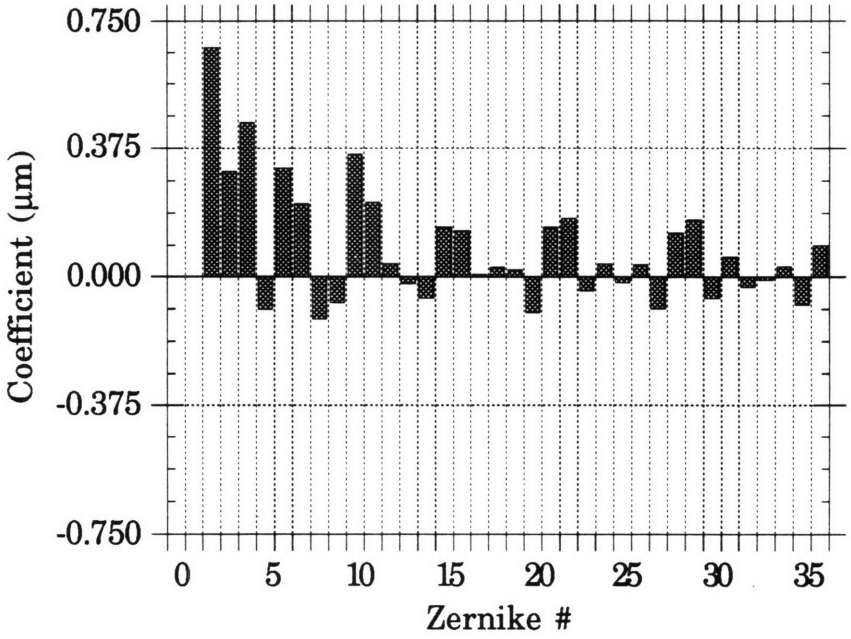

Group 9 Surface Deformation

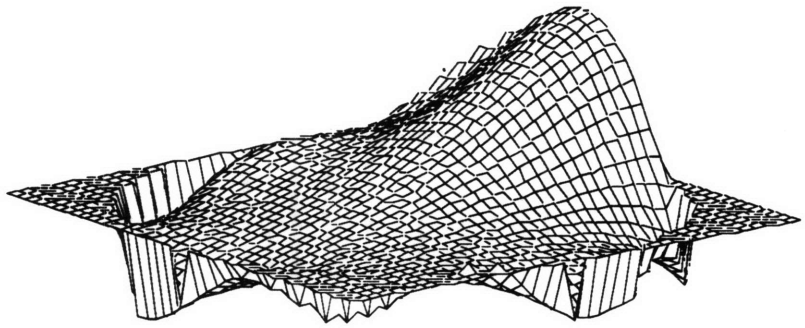

Group 10 Zernike Distribution

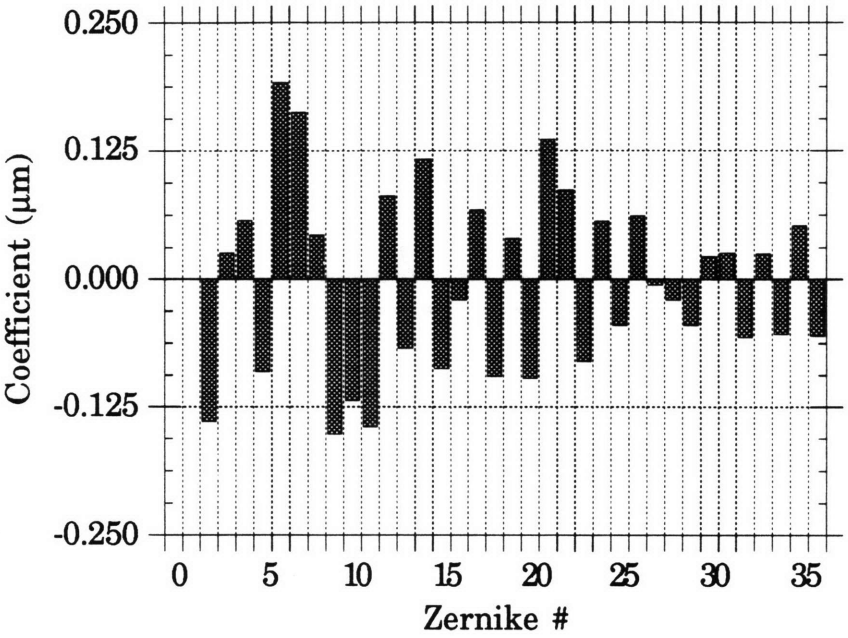

Group 10 Surface Deformation

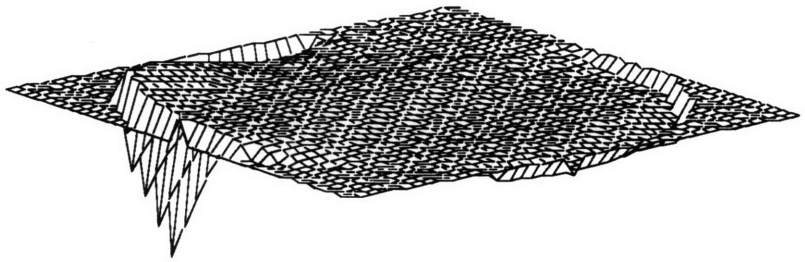

Group 11 Zernike Distribution

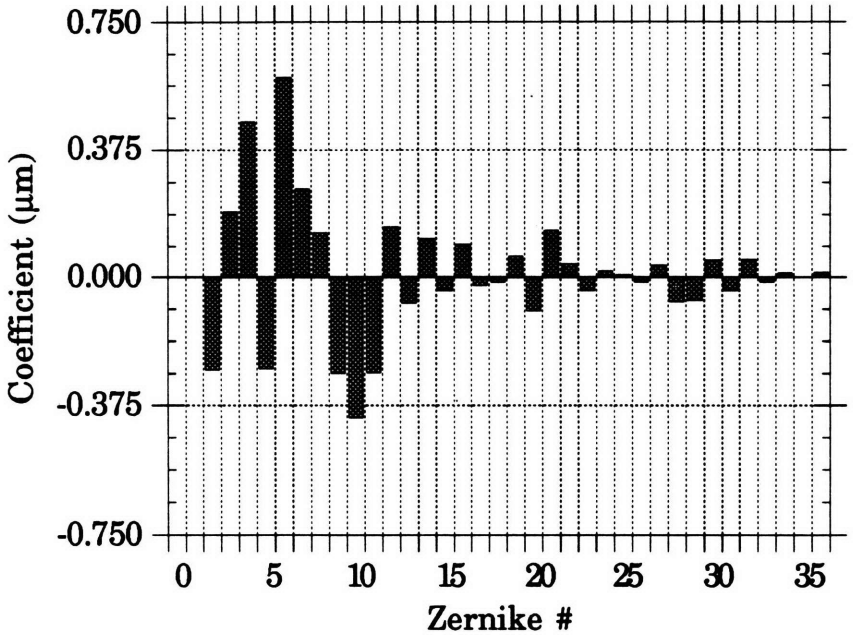

Group 11 Surface Deformation

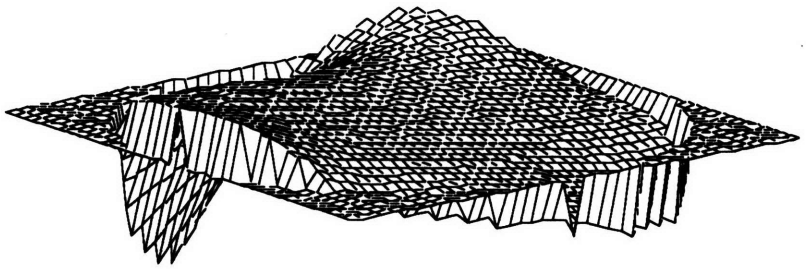

Group 12 Zernike Distribution

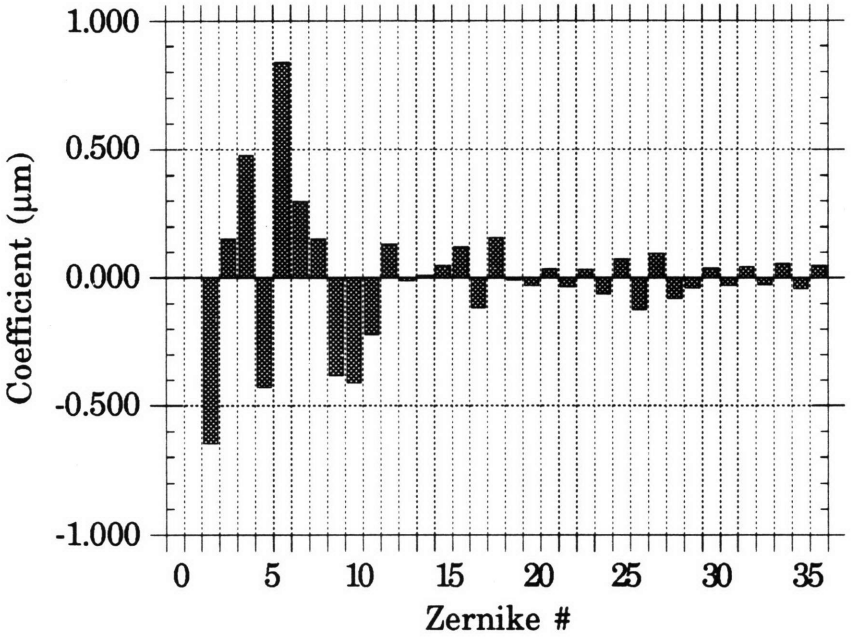

Group 12 Surface Deformation

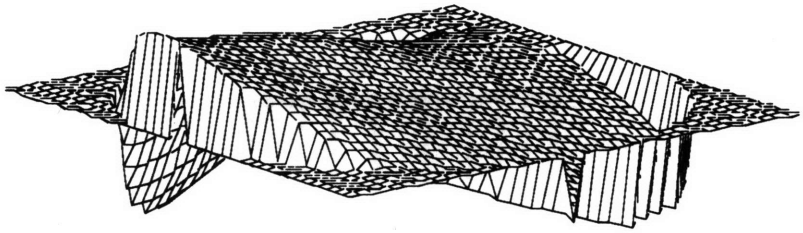

Group 13 Zernike Distribution

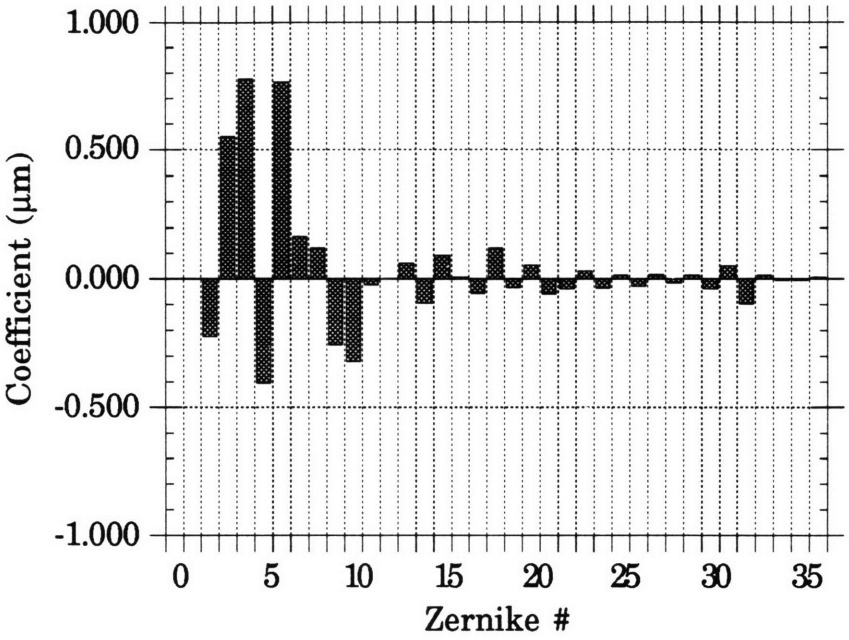

Group 13 Surface Deformation

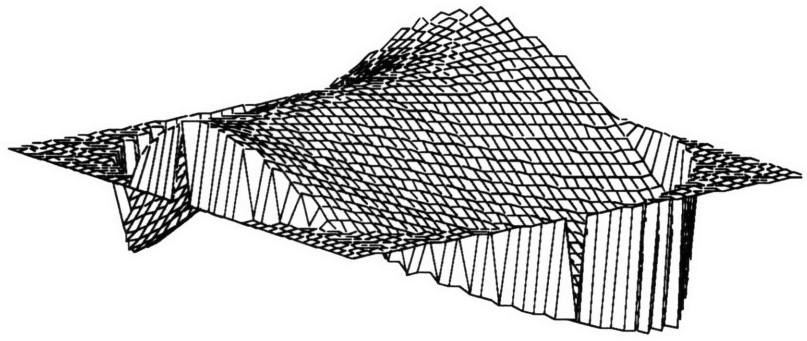

Group 14 Zernike Distribution

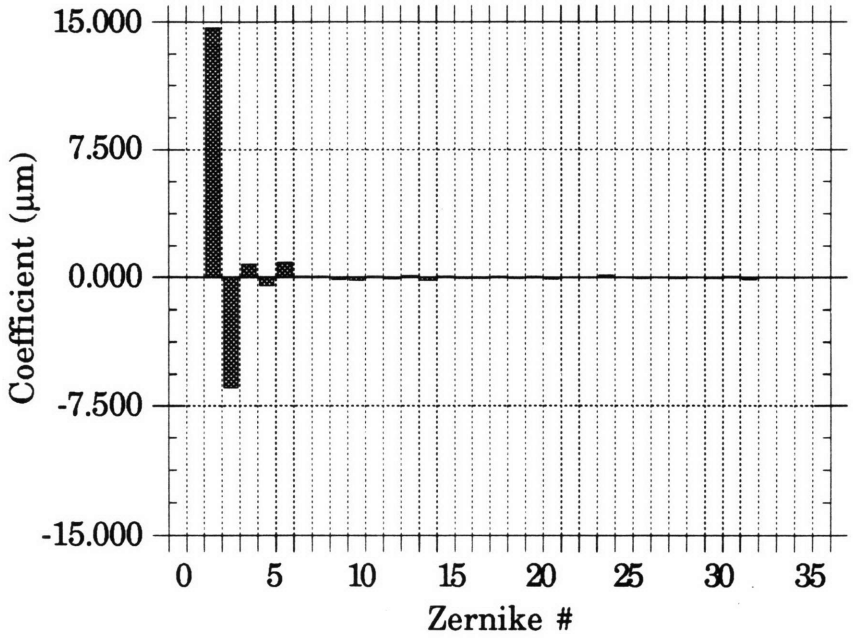

Group 14 Surface Deformation

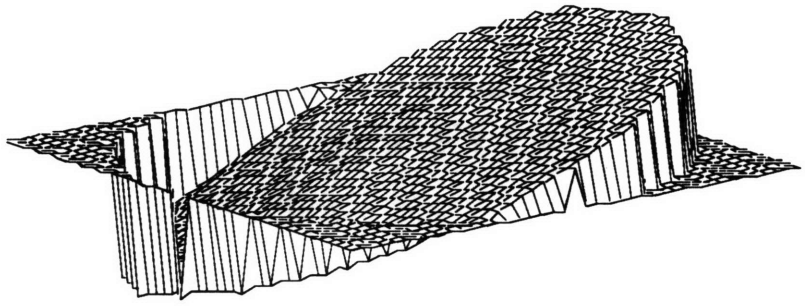

Group 15 Zernike Distribution

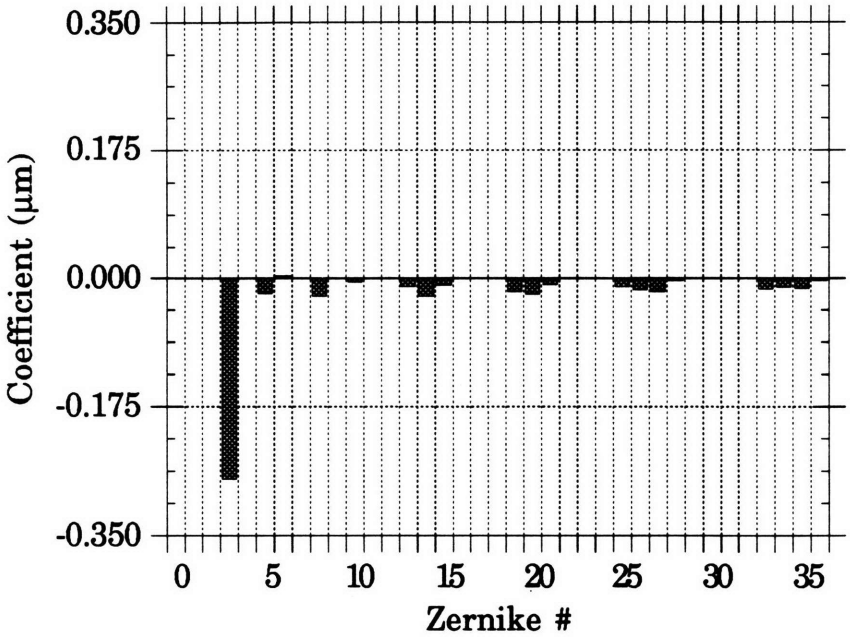

Group 15 Surface Deformation

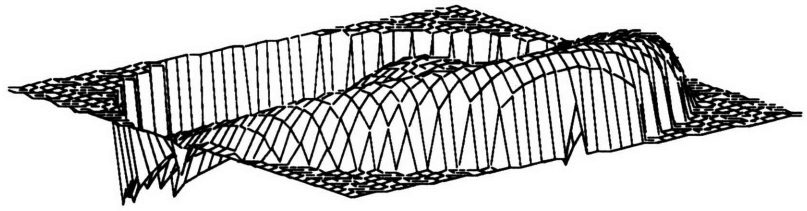

Group 16 Zernike Distribution

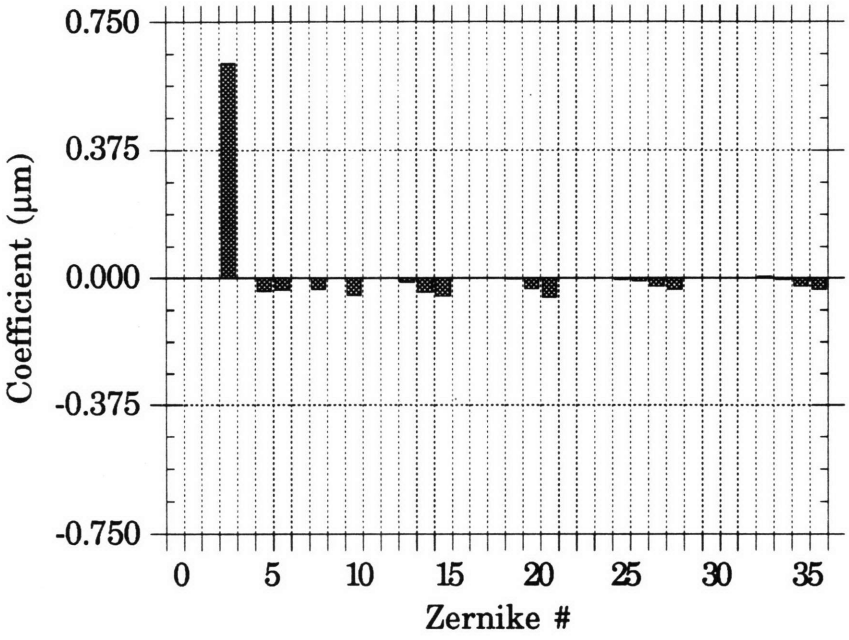

Group 16 Surface Deformation

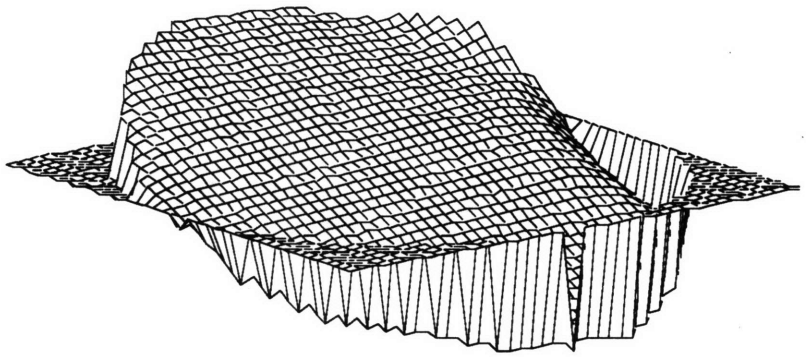

Group 17 Zernike Distribution

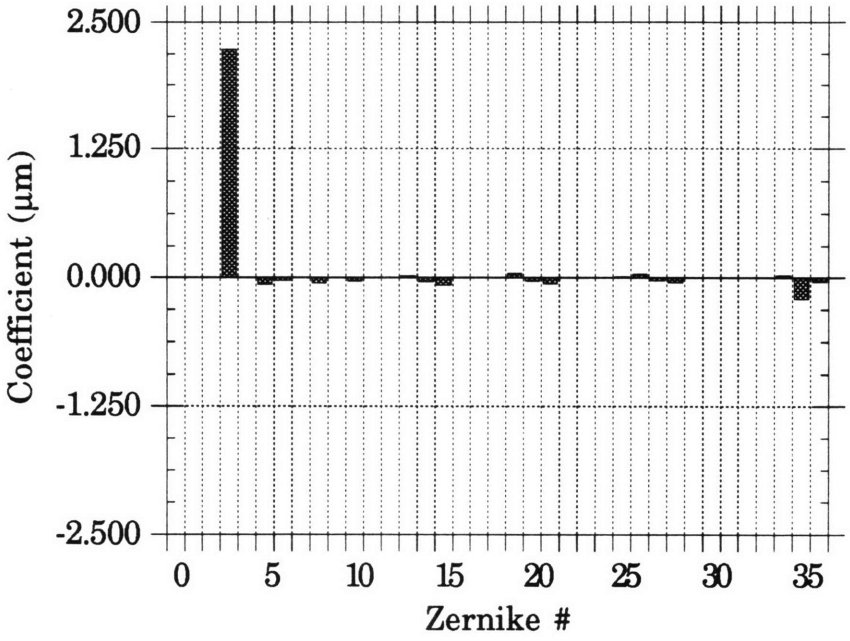

Group 17 Surface Deformation

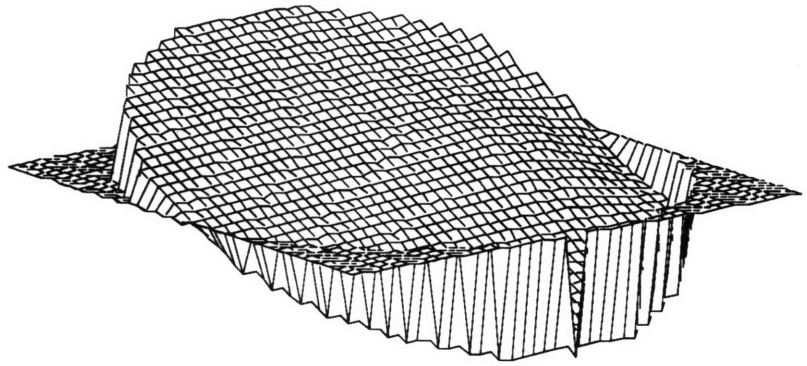

Group 18 Zernike Distribution

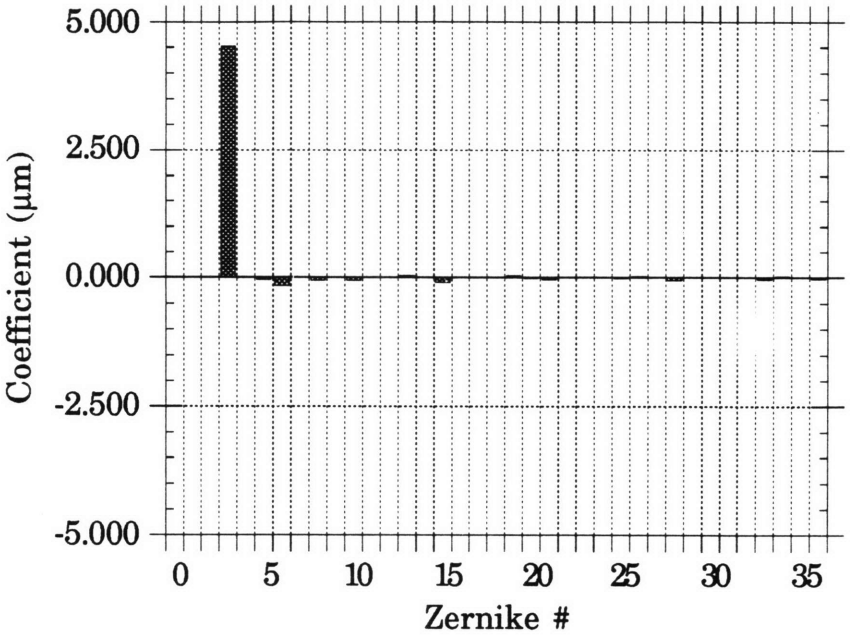

Group 18 Surface Deformation

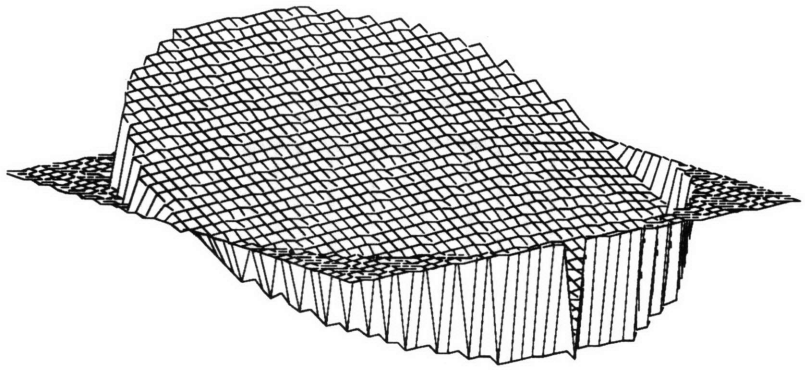

Group 19 Zernike Distribution

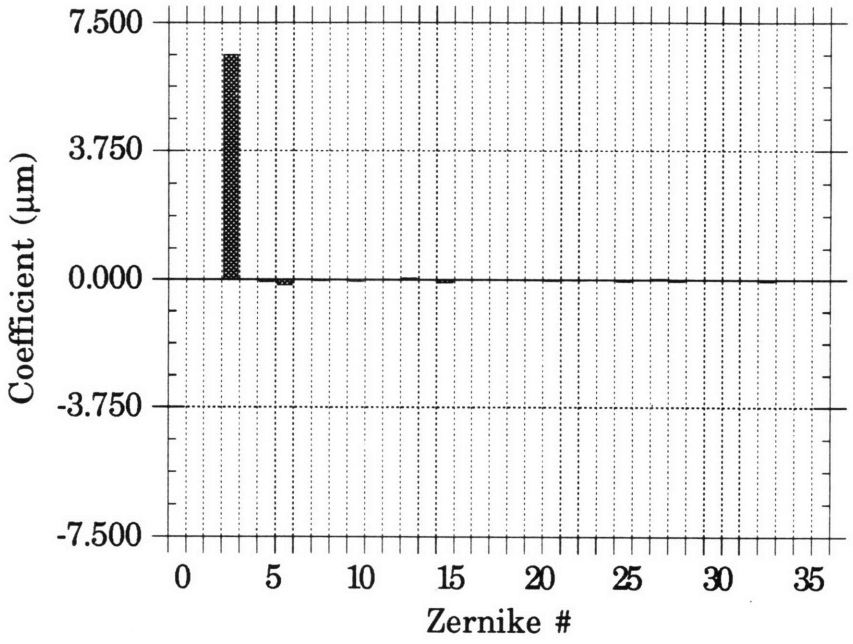

Group 19 Surface Deformation

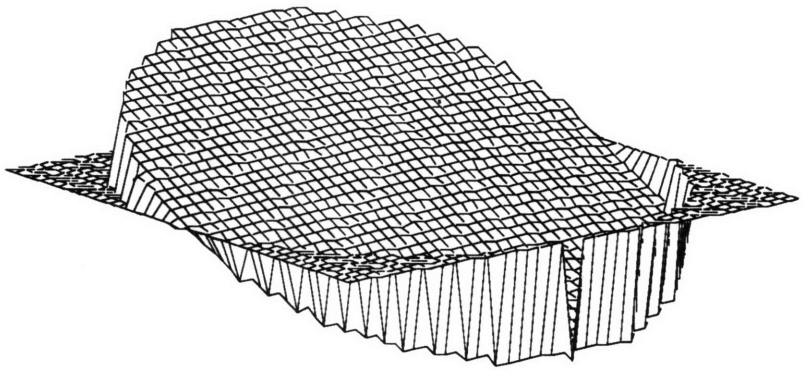

A.6 Dwarf-to-Background Ratios

The data in this appendix describes the peak dwarf-to-scattered background signal ratio for several star/dwarf combinations at various angular separations. The first separation of each combination is the minimum separation required under nominal conditions, as defined by the revised version of Black's Law (Eq. 2.6). At each separation, the peak dwarf-to-background signal ratio is given. The ratio, measured from point spread function plots generated by SAO Image, is the ratio between two points at equal and opposite distances from the center point along the vertical axis. One point is the location of the dwarf, the other is the diffraction signal from the primary star. Ideally, this ratio equals 2.0 at minimum separation, and increases with increasing separation. The actual values vary, however, because nominal PSF image generated by the hexagonal panel reflector system (Fig. 3-1) varies azimuthally for a given distance from the center.

Comparison of Peak Dwarf-to-Scattered Background Signal Ratios for Nominal, Thermally Aberrated and Test Case 11

Object Combination	Separation (asec)	Nominal Ratio	Aberrated Ratio	Test Case 11 Ratio
6000 K star/ 2400 K dwarf	2.04	1.25	8.46	1.19
	3.0	15.9	1.05	9.42
	4.0	35.2	209.0	3.5
	6.0	14.9	7.67	2.11
6000 K star/ 1000 K dwarf	2.83	1.84	1.02	1.18
	4.0	12.9	78.8	1.75
	6.0	5.86	3.33	1.39
	8.0	17.7	11.4	36.5

Object Combination	Separation (asec)	Nominal Ratio	Aberrated Ratio	Test Case 11 Ratio
6000 K star/ 640 K dwarf	3.83	2.96	13.5	1.41
	5.0	8.81	2.31	3.12
	6.0	2.86	1.89	1.15
	8.0	7.32	4.97	14.5
6000 K star/ 450 K dwarf	5.2	5.94	38.7	30.1
	6.0	1.70	1.32	1.06
	8.0	3.32	2.46	5.97
	9.0	32.7	2.84	6.80
3600 K star/ 2400 K dwarf	0.68	2.53	13.3	26.1
	1.0	2.44	6.22	3.02
	2.0	8.73	200.0	6.75
3600 K star/ 1000 K dwarf	0.95	1.50	2.65	1.74
	2.0	3.70	77.6	3.02
	4.0	410.0	2300.0	19.5
3600 K star/ 640 K dwarf	1.28	2.46	1.25	1.26
	2.0	2.02	301.7	1.77
	4.0	157.1	920.0	10.9
3600 K star/ 450 K dwarf	1.74	2.87	1.11	1.67
	3.0	26.1	1.08	15.2
	5.0	99.7	17.7	27.8
3600 K star/ 300 K dwarf	2.89	1.83	1.02	1.76
	4.0	12.4	60.0	1.67
	6.0	5.57	3.19	1.37

References

Allen, C.W. *Astrophysical Quantities*, Athlone Press, London, 1976.

Anderson, David. *Fringe Manual Version 3*. University of Arizona, Tuscon, 1982.

Anderson, E.H., Moore, D., Fanson, J.L., Ealey, M. "Development of an Active Member Using Piezoelectric and Electrostrictive Actuation for Control of Precision Structures", JPL report (section 354), 1990.

Anderson, Eric H. *Piezoceramic Actuation of One and Two Dimensional Structures*, MIT Master's thesis SSL #5-89, 1989.

Anonymous. "View Zernike Coefficients - Surface Analysis", Breault Research, Inc., 1991.

Aubrun, J., Lorell, K., Nast, T., Nelson, J. "Dynamic Analysis of the Actively Controlled Segmented Mirror of the W.M. Keck Ten Meter Telescope", IEEE Control Systems Proceedings Vol. VII #6 (1987).

Bertsekas, Prof. Dimitri. Nonlinear Programming (6.252) lecture notes, section 4.4, MIT (1992).

Black, D. "In Search of Other Planetary Systems", Space Science Reviews #25 (1980).

Borne, M., Wolf, E. *Principles of Optics: Electromagnetic Theory and Propagation, Interference and Diffraction of Light*, Pergamon Press, 1980.

Chamis, C.C., Aiello, R.A., Murthy, P.L.N. "Fiber Composite Sandwich Thermostructural Behavior: Computational Simulation", *Journal of Composites Technology and Research* No. 10, 1988.

Chen, G.S. "Piezoelectric Actuator for Cryogenic Application", JPL Interoffice Memorandum 3542/GSC/018-90, January 18, 1990.

Ealey, Mark. "Deformable Mirrors at Litton/Itek: A Historical Perspective", Litton/Itek Optical Systems, report #1167-04 (1990).

Ealey, M., Wellman, J., "Fundamentals of Deformable Mirror Design and Analysis", Litton/Itek Optical Systems report #1167-05, 1990.

Goodman, J. W. *Introduction to Fourier Optics*, McGraw-Hill, 1968.

Hardy, John W. "Active Optics: A New Technology for the Control of Light", Proceedings of IEEE Vol. 66, No. 6, June 1978.

Hochberg, E.B. "PSR Prototype Panel Optical Figure Testing: Cryointerferometric Tests of JPL 91-03 on 5/16/91", JPL Interoffice Memorandum PSR #91-70 (1991).

Information package, Vernitron Corp. Piezoelectric Division, 1991.

Kuo, C.P. "A Deformable Mirror Concept for Adaptive Optics in Space", Jet Propulsion Laboratory section 354 report (1991).

Kuo, C.P., Wada, B.K. "Composite Deformable Mirror", JPL New Technology Report Case No. NPO-18128, 1990.

Lawrence, G.N. *Applied Optics and Optical Engineering* (preprint), Eds. Shannon and Wyatt, Applied Optics Research. Tuscon, 1990.

Malacara, Daniel. *Optical Shop Testing,* John Wiley & Sons, Inc., New York, 1978.

Mast, Terry S., Nelson, Jerry E. "Figure Control for a Segmented Telescope Mirror", Kitt Peak National Observatory Conference Proceedings Vol. I - *Optical and Infrared Telescopes for the 1990's*, May 1980.

Rapp, D. "Direct and Indirect Detection of Extra-Solar Planets and Brown Dwarfs: A Survey Report Written for Non-Specialists", 1990.

Rapp, Dr. Donald. "Potential for Active Structures Technology to Enable Lightweight Passively Cooled IR Telescopes", JPL Report D-9449 (1992).

Redding, D. "A Wavefront Compensation Approach to Segmented Mirror Figure Control", 14th Annual AAS Guidance and Control Conference, AAS 91-054 (1991).

Redding, D. *Controlled Optics Modelling Package User Manual*, release 1.0, Jet Propulsion Laboratory, October 22, 1991.

Redding, D., Breckenridge, W. "Optical Modelling for Dynamics and Control Analysis", AIAA paper courtesy of C.S. Draper Laboratory, 1990.

Redding, D., Milman, M., Loboda, G. "Linear Analysis of Opto-Mechanical Systems", SPIE Aerospace Sensing Conference, Orlando (1992).

Tsuyuki, G., French, L. "On-Orbit Thermal Performance of a Submillimeter Telescope Primary Reflector Panel", Jet Propulsion Laboratory, 1991.

Uchino, K., Tsuchiya, Y., Nomura, S., Sato, T., Ishikawa, H., Ikeda, O. "Deformable Mirror Using PMN Electrostrictor", *Applied Optics*, Vol. 20 No. 17, September 1981.

Wette, M. "NPSOL-in-Matlab Users' Guide", Jet Propulsion Laboratory technical report (section 343), 17 December 1991.